Energy management system strategy of DC microgrids with integration of renewable energy sources and energy storages
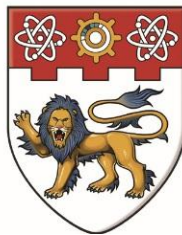
Setyawan, Leonardy

2016

Setyawan, L. (2016). Energy management system strategy of DC microgrids with integration of renewable energy sources and energy storages. Doctoral thesis, Nanyang Technological University, Singapore.
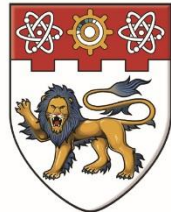
https://hdl.handle.net/10356/68568

https://doi.org/10.32657/10356/68568

ENERGY MANAGEMENT SYSTEM STRATEGY OF DC MICROGRIDS WITH INTEGRATION OF RENEWABLE ENERGY SOURCES AND ENERGY STORAGES

LEONARDY SETYAWAN

SCHOOL OF ELECTRICAL AND ELECTRONIC ENGINEERING

2016

ENERGY MANAGEMENT SYSTEM STRATEGY OF DC MICROGRIDS WITH INTEGRATION OF RENEWABLE ENERGY SOURCES AND ENERGY STORAGES

LEONARDY SETYAWAN

School of Electrical and Electronic Engineering

**A thesis submitted to the Nanyang Technological University
in partial fulfillment of the requirement for the degree of
Doctor of Philosophy**

2016

Acknowledgement

This thesis could not be finished without all the assistance and support from all the related parties. First and most importance of all, I would like to thank my Lord and Savior Jesus Christ because of His continuous grace that never ceases in my life. I also want to thank my wife, Jessie Darma, who always loves me and gives me endless support since I started my PhD study. In this opportunity I also want to thank my parents, Lim Se Thian and Lie Kian Ho, for their loves and encouragement in my life.

I would also like to express my gratitude to Xiao Jianfang for his guidance, assistance and advice towards me throughout all my PhD journey; I also want to acknowledge Zhao Tianyang for his significant help in my projects; I also would like to take this moment to remember my friends, team members and technicians who always available to facilitate my needs and give me ample suggestions while I was doing my research work. My PhD's life has become more colorful and enjoyable with their presence.

Last but not least, I want to give special thanks and appreciations to my supervisor Associate Professor Wang Peng who has always been guiding me during my PhD research and study. I am very proud to have him as my supervisor because he never gives up on me. His advices and suggestions are always very encouraging for me and it has helped me to develop my interpersonal, academic and technical skills.

Table of Contents

Summary

DC microgrids are gaining popularity along with the increasing penetration of RESs, energy storages and DC-inherent loads in current power systems. Some major advantages of DC microgrids are the reduction of power conversion ineffectiveness and the reduction of carbon emission to the environment. EMS strategy is required in order to maintain the system stability and improve system cost-effectiveness. Control of each system unit which is important in realizing EMS in DC microgrids is explained in detail. System stability of DC microgrids is affected by system power balance. Moreover, parameters like system operation cost, battery lifetime, load management, *etc*. should also be considered to deploy a cost-effective DC microgrid. Several EMS strategies for DC microgrids is proposed, elaborated and implemented in this report.

The simplest EMS strategy to be implemented in DC microgrids is distributed EMS. Distributed EMS which does not require communication links in the operation, depends only on local bus voltage as a global indicator of system power balance. Two types of distributed EMS strategies for DC microgrids are proposed including multiple modes and advanced multiple-slack-terminal distributed EMS. In multiple modes distributed EMS, system bus voltage is partitioned to several regions and the prioritization of system units are based on their marginal utilization costs. Each system units including RES and BES can be scheduled as slack terminal (voltage regulation mode) or power terminal (power control mode). The scheduling of system units' operating modes is determined from the result of the comparison between the local bus voltage and the threshold voltages.

In advanced multiple-slack-terminal distributed EMS, droop control based on *V-P* droop relationship is employed to minimize system bus voltage variation during the transitions of bus voltage regions. Active power sharing can be fulfilled autonomously and effectively among the multiple slack terminals. However, there are main drawbacks that are impossible to be eliminated by distributed EMS *i.e.* steady state bus voltage deviations, power sharing error and inability in solving systematic optimization.

Therefore, multi-level based EMS with multiple slack terminals consisted of primary control, secondary and tertiary control is proposed to mitigate the main drawbacks of distributed EMS. Distributed EMS is applied in primary control. Secondary control implements bus voltage restoration in order to eliminate bus voltage deviations. Tertiary control functions as power sharing compensator to eliminate errors in power tracking. Power quality of the system can thus be enhanced. System reliability in case of failure in communication link is ensured because system is still able to operate normally with primary control.

Multi-level EMS is also applied for the operation of DC microgrid transition between islanded and grid-tied mode to reduce bus voltage fluctuation and inrush current. Another application of multi-level EMS is on hybrid AC/DC microgrid. Brief explanation on the operation of hybrid AC/DC microgrid with multi-level EMS is presented. Applying multi-level EMS in hybrid AC/DC microgrid ensures system power balance while enhancing the reliability.

One of effective and economic solutions to reduce energy storages (ESs) cost is by applying hybridization of energy storages (HESS) which utilizing the most of different ESs characteristics. EMS strategies for HESS coordination are proposed in this report including distributed and multi-level EMS of HESS. Distributed EMS realizes system net power decomposition and ESs power dispatch effectively and autonomously. Nevertheless, distributed EMS has the main drawbacks such as degraded power quality and control accuracy. Therefore, multi-level EMS of HESS consisted of primary, secondary and tertiary controls, is proposed. In primary control, multiple-slack-terminal distributed EMS of HESS, in which all ESs are scheduled to operate in voltage regulation mode, is implemented. Secondary control applies bus voltage restoration to eliminate system deviation in bus voltage and power sharing compensation to eliminate error in power sharing. Moreover, tertiary control implements autonomous SoC recovery to limit the SoC variation of the ESs with high ramp rate. The superiority of multi-level EMS of HESS is system operation can be retained with primary control in case of communication failure.

In DC microgrids BES has a very important role to mitigate system power imbalance especially when DC microgrids operate in islanded mode. However, currently the price of BES is relatively high. Because the price of BES is of high cost, selection of BES capacity should thus be optimized to reduce system cost. In the operation, system cost related to depth of discharge range and capacity of BES. A method has been proposed in this report to select depth of discharge range and capacity under the minimum system operation cost. The system operation cost including BES lifetime degradation cost and cost of energy not supplied were taken into consideration. The DoD range and BES capacity are selected under the minimum system operation cost.

Extension work on tertiary control of multi-level EMS is also elaborated. More detail formulations on the marginal costs of system units have been realized. Real-time economic dispatch based on marginal cost comparison has been proposed and implemented for DC microgrid operation. The proposed method is able to do power scheduling prioritization intuitively based on marginal cost. The direct comparison of components' marginal cost simplifies the economic dispatch, thus it is suitable for real-time implementation.

The proposed EMS strategies are verified using MATLAB simulation or a lab-scale DC microgrid. Multi-level EMS strategy for hybrid AC/DC microgrid is verified using MATLAB simulation. Other proposed methods including distributed EMS, multi-level EMS, islanding and reconnection procedures for system transitions between islanded and grid-tied modes, multi-level EMS of HESS, are verified in a lab-scale DC microgrid with integration of rooftop solar PV panels, various energy storages, loads and energy sources.

List of Figures

List of Tables

List of Abbreviations

AC	Alternating Current
ARMA	Auto-Regressive Moving Average
BES	Battery Energy Storage
BIC	Bidirectional Interlinking Converter
BMS	Battery Management System
CC-CV	Constant Current-Constant Voltage
CIC	Customer Interruption Cost
DBS	DC Bus Signaling
DC	Direct Current
DG	Diesel Generator
DoD	Depth of Discharge
EMS	Energy Management System
ES	Energy Storage
EV	Electric Vehicle
HESS	Hybrid Energy Storage System
HEV	Hybrid Electrical Vehicle
HPF	High Pass Filter
HRES	High Ramp Rate Energy Storage
HVDC	High Voltage Direct Current
IC	Incremental Conductance
LPF	Low Pass Filter
LRES	Low Ramp Rate Energy Storage
LVDC	Low Voltage DC
MPP	Maximum Power Point
MPPT	Maximum Power Point Tracking
NRDG	Non-Renewable Distributed Generation
NRES	Non-Renewable Energy Source
P&O	Perturb and Observe
PCM	Power Control Mode

PI	Proportional-Integral
PLC	Programmable Logic Controller
PLL	Phase-locked Loop
PR	Proportional-Resonant
PV	Photovoltaic
PWM	Pulse Width Modulation
RES	Renewable Energy Source
RTU	Remote Terminal Unit
SAS	Solar Array Simulator
SCADA	Supervisory Control and Data Acquisition
SCDFs	Sector Customer Damage Functions
SoC	State of Charge
UC	Ultra-Capacitor
VRM	Voltage Regulation Mode
WT	Wind Turbine

List of Symbols

A	Ideality factor
C	Equivalent capacitance of DC microgrid
C_A	Actual capacity at actual discharging rate
C_{Ai}	Actual capacity of BESi
C_{BESi}	Cost of BESi
C_R	Battery rated amp-hour capacity at rated discharging current
D_A	Actual Depth of discharge
D_{Ai}	Actual Depth of discharge of BESi
d_A	Actual ampere-hour discharge
d_{Ai}	Actual discharge of BESi
d_{BES}	Duty ratio for BES converter
d_{eff}	Effective ampere-hour discharge
d_{NRES}	Duty ratio for NRES converter
dP_{net}^{max}	Maximum system net power change rate
d_{PV}	Duty ratio for PV converter
D_R	Rated depth of discharge
DoD_i	Depth of Discharge of the ith battery energy storage
E_{gap}	Band gap energy
f_{ESi}	Cut-off frequency of ESi
f_{ESi}^{max}	The maximum cut-off frequency of ESi
G_{BES}	Switching signal for BES converter
G_{BIC}	Switching signal for BIC
G_{BVR}	PI gain for bus voltage restoration
G_{NRES}	Switching signal for NRES converter
G_{PSCi}	PI gain for i^{th} slack terminal in power sharing compensation
G_{PV}	Switching signal for PV converter
I_{BES}	Output current of BES
I_d	Inductor current in direct axis
I_d^*	Reference inductor current in direct axis

I_L	Inductor current
I_L^*	Reference inductor current
I_{mp}	PV output current at the maximum power point
I_{ph}	Photocurrent
I_{PV}	Solar PV output current
I_q	Inductor current in quadrature axis
I_q^*	Reference inductor current in quadrature axis
I_{rr}	Reverse saturation current at T_r
I_{sat}	Saturation current
I_{SC}	Short-circuit current of solar PV panel
I_{sso}	Short-circuit current
k	Boltzman constant
k_i	Short-circuit current temperature coefficient
K_{1d}	SoC recovery coefficient of ES1 in distributed EMS
L_R	Rated life cycle of battery energy storage
M	Number of voltage sensitive loads
m_{BESs}	Droop coefficient of BESs
m_{BIC}	Droop coefficient of BIC
m_{eq}	Equivalent droop coefficient
m_i	Droop coefficient of the ith slack terminal
m_{RESs}	Droop coefficient of RESs
MC_{BESi}	Marginal cost of BESi
MC_{NRES}	Marginal cost of NRES
MC_{RES}	Marginal cost of RES
MC_U	Marginal cost of utility grid
n_p	Number of solar cells in parallel
n_s	Number of solar cells in series
P_{BES}	Output power of battery energy storage
P_{BES}^*	Reference output power of battery energy storage
P_{BES}^{max}	Maximum discharging power of battery energy storage

$P_{BES}^{\min}$	Maximum charging power of battery energy storage
P_{BIC}	Output power of bidirectional interlink converter
P_{BIC}^{*}	Reference output power of bidirectional interlink converter
P_C	Charging power of the system capacitor
P_{Con}	Power consumption
P_{ES}	Output power of energy storage
P_G	Output power of diesel generator
P_{Gen}	Power generation
P_i	Output power of the ith slack terminal
P_{L_ac}	AC load power consumption
P_{L_dc}	DC load power consumption
P_{Loads}	Load power consumption
P_{mp}	Maximum output power of solar PV panel
P_{net}	System net power
P_{NRES}	Output power of nonrenewable energy source
$P_{NRES}^{\max}$	Maximum output power of NRES
P_{PV}	Output power of solar PV
P_{RES}	Renewable energy source generation
$P_{RESs}^{\max}$	Maximum output power of RESs
P_{WT}	Output power of wind turbine
q	Electron charge
R_s	Series resistance of a PV cell
R_{sh}	Shunt resistance of a PV cell
RC_i	Replacement cost of BESi
r_{ESi}	Ramp rate of ESi
S	Solar irradiation level
SoC_{nom}	Nominal state of charge
SoC_{max}	Maximum state of charge
SoC_{min}	Minimum state of charge
T_r	Reference temperature

T_s	Surface temperature of the PV
T_{ESi}	Time constant for the LPF of ESi
V	System bus voltage
$\overline{V}$	Average bus voltage
V_{bat}	Battery bank terminal voltage
V_{BES}	Output voltage of BES
V_{BES}^*	Reference BES converter output voltage
V_{H1}	Threshold voltage for bus voltage range region H1
V_i	Output voltage of the ith slack terminal
V_i^*	Reference voltage of the ith slack terminal
V_{L1}	Threshold voltage for bus voltage range region L1
$V_{\max}$	Maximum allowable bus voltage
$V_{\min}$	Minimum allowable bus voltage
V_{mp}	PV terminal voltage at the maximum power point
V_n	Nominal bus voltage
V_{NRES}	Output voltage of NRES
V_{NRES}^*	Reference NRES converter output voltage
V_{OC}	Open-circuit voltage of PV
V_{oi}	Threshold voltage of the ith slack terminal
V_{PV}	Solar PV terminal voltage
V_{PV}^*	Reference PV terminal voltage
V_{PVo}	Output voltage of PV converter
V_{PVo}^*	Reference output voltage for PV converter
V_{Si}	Bus voltage measured at the ith sensitive load
ΔP_i	Output power change of the ith slack terminal
ΔP_{ES1}	Modified output power of ES1
ΔT	Operating period time-step
ΔV	Change of system bus voltage
ΔV_i	Output voltage change of the ith slack terminal
ΔV_{iP}	Power sharing voltage compensator for the ith slack terminal

ΔV_V	Voltage compensator for bus voltage restoration
δV	Change in threshold voltage due to line impedance
δm	Change in droop coefficient due to line impedance

Chapter I

Introduction

1.1   Motivations

Alternating current (AC) power system is widely used all over the globe for over 120 years because its superiority over direct current (DC) power system especially in the capability of stepping up and stepping down system voltage level [1]. Implementing a very high voltage for the transmission can significantly reduce the power loss in the transmission line which was not be able to be performed by DC power system at that time. High voltage AC power system provides long distance transmission that can supply the electricity to consumers whose location usually far from generation station [2].

Although the existing grid has predominance in transmitting electricity for a long distance, some issues are also existed, described as follows [3-5]:

a.   Centralized system

Centralized power systems are capital intensive to be established which results in long gestation periods. Given this situation, unprecedented increase in electricity demand can decrease power quality and reliability. Besides, centralized power plants in the existing grid which is based on the idea of unidirectional power flows, do not guarantee energy security, access, affordability and flexibility at the individual consumer and community level. In transmission side, long distance indicates high installation cost of transmission line from generation side to consumer side which will be burdened to consumers.

b.   Low reliability

Distribution system in the existing grid, where the traditional radial distribution system causes reliability concerns. In addition to that, the aging existing grid both in terms of generating plants and also transmission lines also induces low reliability. A single faulty in transmission line can affect consumers which are provided by the

affected transmission line. The effect even becomes worse if the faulty happens in the generating plant, the affected consumers can be more in numbers. Increasing in digital equipment cannot afford a low reliability power grid since an outage can significantly impact the lifetime of the equipment. Besides that, with an exponential relationship between the cost of the system and the cost of reliability, the cost of improving every percentage point of reliability causes an increasing order of magnitude of costs since system redundancy needs to be introduced. Therefore, the grid providers are very reluctant to improve the system reliability.

c. Inefficiency at managing peak load

The capacity of the grid is planned to withstand maximum anticipated peak demand of its aggregated loads. However, the occurrence of peak demand which is infrequent, leads the existing grid to be inherently inefficient.

Driven by the issues faced by existing grid, microgrids which are distributed systems are gaining their popularity. Microgrids can be designed to answer issues that come from the existing grid. Since microgrids are distributed system, microgrids can guarantee individual consumer special needs *i.e.* sustain local voltages, enhance local reliability, offer increased efficiency, decrease feeder losses, provide voltage sag correction or provide uninterruptible power supply functions, etc. [6]. In addition, integration renewable energy sources (RESs), for example, photovoltaic (PV) and wind turbine, to microgrids is able to reduce carbon emission [4, 5].

Along with the growing application of DC sources, energy storages and loads in today's power systems, DC microgrids are one of the solutions to cope with the power conversion ineffectiveness and the greenhouse effect to the environment [7, 8]. Some factors that boost the improvement of DC microgrids favored with their advantages over AC microgrids include [7, 9, 10]:

a. DC-inherent load

Since the invention in 1960s, semiconductor materials which are natively DC, have dictated electronic and electrical devices, *i.e*. LED lighting, LCD display, computer

2

and communication devices, variable speed drives, *etc*., in such a way that soon most of the load base will be natively DC. Currently, almost 30% of the total consumption loads are consumed by DC-inherent loads, and that percentage is predicted to expand to 80% in 10-15 years [11, 12]. In addition, the tremendous adoption of electric vehicle (EV) which requires DC power charger deliver another extension of DC loads applications [13]. Since AC system is applied in current power distribution network, dedicated AC/DC rectifiers are needed to convert utility AC power to DC power. Energy losses because of the conversion from AC to DC can reach up to 32%. These conversion losses can be reduced from 32% down to 10% by connecting DC loads directly to DC microgrids [8].

b. <u>Distributed renewable generations</u>

Distributed energy resources (DERs) from renewable energy sources (RESs) *i.e*. fuel cell and photovoltaic (PV) which are carbon-free energy resources are also DC-inherent. DC-AC inverters are required to transfer the harvested energy of RESs to the conventional AC distribution system. The inversion processes which result in energy losses can be diminished by incorporating DC microgrids. In addition, since more and more loads served are DC-inherent, integrating DC microgrids can decrease DC-AC-DC conversion losses which consume 15% or more of RESs generated energy [14].

c. <u>Energy storages</u>

RESs generation highly depends on the weather conditions which will cause intermittency. The intermittency of RESs induces significant variations of RESs power generation. The increase of RESs penetration makes the effect becomes more severe [15]. Therefore, sufficient energy storages (ESs) should be installed to mitigate generation variations. By charging during load valley and discharging in case of load peak energy storages are able to smoothen the generation variations of RESs [16-20]. The integration of ESs and DERs can be regarded as a dispatchable generator. Since most of the ESs like battery, ultra-capacitor (UC), flow battery, *etc*. are inherently DC the integration of DC microgrid can reduce energy losses caused by power conversion.

d. Conversion efficiency

AC-DC, DC-AC and DC-AC-DC conversions can be reduced by implementing DC microgrids. Energy losses due to power conversions can be curtailed to 10% − 32% [8, 14].

e. Environment aspect

Unlike the conventional fossil-fueled generators which produce massive carbon emission, RESs integration in DC microgrids can significantly reduce carbon emission which will contribute to cleaner environment. One application that has been realized is zero-net-energy buildings which were designed to demonstrate the possibility of "cleanly" generation of RESs to fulfill the overall building power consumption [14].

f. Control simplicity

Different with conventional AC distribution networks that must consider AC voltage and frequency parameters, DC microgrids only consider system bus voltage parameter to govern the system power balance that makes the control simpler. Since there is no frequency parameter that must be controlled, hence no harmonics exists in the system, reactive power constraints is eliminated and synchronization of diverse generation sources to a single ac grid frequency can also be eliminated [4].

g. Power electronics advancement

Since semiconductor invention, developments of power electronics converter systems for electric power applications has been started since the early 1970s [12]. The advancement of power electronics for electric power applications enables DC system to boost or buck DC voltage easily. With this capability high voltage direct current (HVDC) transmission can be realized. Furthermore, it has been proven that DC power transmission have higher transmission capacity, better stability with transmission loss reduction of up to 30% − 50 % [21].

Energy management system (EMS) strategy is required to control the operation of DC microgrids. A single objective or multi-objectives of EMS strategy are defined

by the user based on their needs. The main motivations of this research are to cope with major problems which are arises in the area of coordination control and EMS strategy considering the economic factor for DC microgrids.

1.2   DC Microgrid

DC microgrid consists of interconnected distributed energy resources (micro turbines, wind turbines, fuel cells, PV, *etc*.), distributed storages (batteries, ultra-capacitors, *etc*.) and loads which primarily generates, distributes, stores, and consumes electricity in DC form at low voltages [8, 14, 22]. DC microgrids can be operated either tied to the traditional centralized grid (grid-tied mode) or functions autonomously dictated by physical and/or economic conditions (islanded mode).
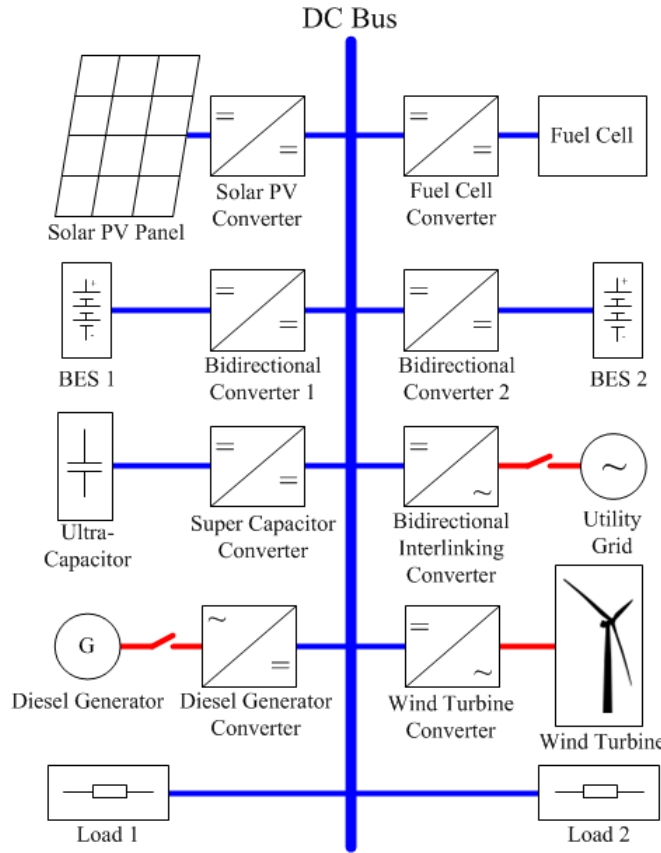
Fig. 1.1 Diagram of a typical DC microgrid.

The diagram of a typical DC microgrid shown in Fig. 1.1 normally comprises renewable energy sources (RESs), conventional generators, energy storages, and loads. PV panels, wind turbine (WT) and battery energy storages (BESs) are linked

5

to the DC microgrid through DC-DC converters, wind turbine converter and bidirectional DC-DC converter, respectively. Non-critical and critical loads are connected either directly or through converters to the DC microgrid [6, 23]. RESs converters usually operate in MPPT mode to maximize output power. BESs are deployed to compensate the RESs generation intermittency and load consumption uncertainty by charging and discharging power. Non-renewable energy source (NRES) *i.e.* diesel generator connected to AC-DC rectifier provides the backup generation to DC microgrids when the total RESs generations and ESs are not sufficient to supply total load consumptions. Power exchange between the utility grid and the DC microgrid in grid-tied state is controlled through a bidirectional interlinking converter (BIC) [24]. Islanded mode is executed when a disturbance such as bus voltage fluctuation, frequency range violation, *etc*. in utility grid occurs.

Applications of DC microgrids include data center [7, 25], commercial and residential buildings [26-28], HVDC [21, 25, 29-32], electric vehicle [33-35], renewable energy sources integration [36], *etc*.

System stability of DC microgrids is affected by system power balance and bus voltage which are interrelated one another. Besides that, to deploy a cost-effective DC microgrid, parameters like system operation cost, battery lifetime, load management, *etc*. should also be taken into consideration. Therefore, EMS strategy should be implemented to integrate all system units such that DC microgrid operation can be optimized.

1.3   DC Microgrid Challenges

Although a lot of advantages are offered by DC microgrids, the implementation of the DC microgrids has several challenges include [8, 14]:

a.   <u>Robust EMS strategy</u>

Robust EMS strategy to coordinate all system units is required in DC microgrids to incorporate various energy sources, storages and loads. Distributed, centralized or hybrid EMS strategy should be investigated.

b. Codes and standards

Codes and standards are required to regulate system power quality requirements of DC microgrids uniformly. For the time being only few codes and standards exist related to DC microgrids application. The 48 VDC is one standard that has been well-established for decades as the voltage in plain old telephone service. Others, such as 380 VDC for data/telecom centers and 24 VDC for LED lighting system has been published by Emerge Alliance which in one of the most active organizations for low voltage DC (LVDC) standardization [7]. Rebus Alliance has also published a draft version of detail specifications on how to create an interconnect topologies that most easily and efficiently integrates RESs into the electrical energy mix for household DC microgrids [37].

c. Safety and protection

Safety and protection issues are being addressed progressively by standards and trade organization such as International Electrotechnical Commission (IEC), Institute of Electrical and Electronics Engineers (IEEE), Power Sources Manufacturers Association (PSMA), Smart Grid Interoperability Panel (SGIP) of the National Institute of Standards and Technology (NIST), and others. Specific protection devices and appliances for DC microgrid application are rare and costly because the needs are still limited so that mass production is still not able to be conducted.

d. Robust ecosystem to support DC microgrids applications

Suppliers, customers and government play important roles in DC microgrids ecosystem. Suppliers' roles are to provide qualified products including DC-compatible protection devices, sources, equipment, meters and others. Concerning the benefits provided by DC microgrids, customers are expected to play their roles for the promotion of DC microgrids. Government has a major stake by providing respective incentives and regulating the market to pioneer DC microgrids developments.

e. <u>Transformational path forward</u>

An unclear direction for shifting from AC-centric power distribution to DC-inclusive distribution schemes is also challenge existed in DC microgrids implementation.

This thesis emphasizes more on solving some problems arisen from the robust EMS strategy of DC microgrids. Several EMS strategies considering the economic factor are proposed to mitigate some problems.

1.4 Objectives

This thesis focuses on the implementation of different type of EMS strategies in DC microgrids with the integration of renewable energy resources and energy storages considering economic factor and system stability. The main objectives of this thesis include:

a Conduct a thorough literature reviews on the existing energy management system strategies for DC microgrids.

b Apply a robust control for individual system unit such as PV, BESs, ultra-capacitor, *etc*. in the DC microgrid.

c Propose distributed energy management system strategies in DC microgrids to ensure system stability.

d Realize multi-level energy management system strategies in DC microgrids not only to ensure system stability but also minimize bus voltage variation that is not able to be mitigated by applying distributed EMS.

e Evaluate different types of energy storages and propose EMS strategy for hybridization of energy storages.

f Propose depth of discharge range and capacity optimization of battery energy storages implemented in DC microgrids.

g Propose a real-time economic dispatch EMS strategy based on system units' marginal cost.

h Conduct experiments in a lab-scale DC microgrid to validate several energy management system strategies that are proposed.

1.5   Major Contributions

The major contributions of this thesis are:

a.   <u>Distributed EMS for DC microgrid operation</u>

Distributed EMS is employed in DC microgrid operation to eliminate the need of communication link and increase system reliability due to communication failure. DC bus voltage plays a very important role as the global indicator to system power balance. Nominal DC bus voltage is the DC bus voltage at system balanced condition. In distributed EMS, DC bus voltage is allowed to vary within the range which is partitioned to several regions. The threshold voltages of each voltage range are compared with the local bus voltage in real-time operation to schedule the operating modes of all system units. A system unit with voltage regulation mode (VRM) has to be scheduled to regulate DC bus voltage. Prioritization of the activation of system units, including RESs, ESs, loads, DGs, *etc*. is prioritized based on their utilization costs. Droop relationships are imposed when system units operate in (VRM) to prevent uncontrollable circulating current, perform active power sharing and ensure smooth transition between different bus voltage regions.

b.   <u>Multi-level EMS for DC microgrid operation</u>

Although higher reliability due to the elimination of communication link has been presented, because of the line impedance and imposed droop relationship in actual implementation, deviation in bus voltage and error in power tracking exist as the main drawbacks of distributed EMS of DC microgrid. To mitigate the main drawbacks of distributed EMS and enhance system control accuracy hence multi-level EMS strategy is proposed. It is divided into three levels of control *i.e*. primary, secondary and tertiary control. The primary control is the implementations of DC bus signaling (DBS) and droop control same as distributed EMS. In secondary control, bus voltage restoration and power sharing compensation are performed to eliminate the bus voltage deviations and the power tracking errors, respectively, so that system power quality can be ensured. Lastly, tertiary control generates power references to all system units based on minimization of system operation costs. A

novel economic dispatch method is introduced in the tertiary control. Besides, the seamless transition between islanded and grid connected mode in multiple-slack-terminal multi-level EMS is elaborated. In case the DC microgrid is connected to utility grid, seamless transition method from islanded mode to grid-tied mode or vice versa, is explained comprehensively. Multi-level EMS for hybrid AC/DC microgrids is also described.

c. Hybridization of energy storages system

Hybridization of energy storages with different characteristics is an effective and economic solution to compensate system power imbalance consisted of high and low frequency elements. Distributed EMS for hybrid energy storage system (HESS) is proposed to retain system power balance. In distributed EMS, high ramp rate energy storage (HRES) is scheduled in voltage regulation mode (VRM) with droop control and low ramp rate energy storages (LRESs) in power control mode (PCM). The power references LRESs are generated according to local bus voltage variations with reverse droop control. High frequency power variation is compensated by HRES, whereas the low frequency element by LRESs. State of charge (SoC) recovery has also been proposed to avoid ESs from over-charged/discharged damage. However, degraded power quality and control accuracy are always the prime disadvantages of distributed EMS.

d. Optimal DoD range and capacity setting of battery energy storage

Battery energy storage is installed for mitigation of microgrids power imbalance induced by the intermittency of renewable sources and load changes. Optimal sizing of battery energy storage is crucial for economic operation of a microgrid due to high capital cost. Therefore, optimization method is proposed to determine both depth of discharge range and capacity under the minimum system operation cost. Time varying resource and load conditions are considered in the optimization. System operation cost function consisted of the cost of BES lifetime degradation and energy not supplied are quantified and incorporated. The proposed method is verified using MATLAB simulation.

Therefore, multi-level EMS based HESS is proposed. The mode operations of all ESs are assigned in VRM with droop control. In primary control, system net power decomposition is performed by applying low pass filter (LPF) at the feedback voltage of LRESs. Bus voltage restoration and power sharing compensation are realized in secondary control. Furthermore, tertiary control incorporates autonomous SoC recovery to restore SoC of HRES to the nominal value.

e.   Marginal cost based real-time economic dispatch

A function for a particular or multiple objectives such as minimum operating cost is usually established in DC microgrids to dispatch power from system units for a given operating period. The solution is not accurate because the solution time is usually in scale of minutes. Therefore, a real-time power dispatch method for operation of microgrids with renewable sources under the minimum system cost is proposed. The real-time system units' marginal costs are quantified and compared to schedule the operation of system units. Both the real-time depth of discharge and discharge rate have been considered in battery energy storage cost model to update the remaining life related marginal cost. To reduce the decision time for real-time operation, the utilization prioritization of system units based on their marginal costs is proposed for power dispatch. The proposed method is implemented and verified in a lab-scale DC microgrid with multi-level energy management system based control.

1.6   Organization

This thesis is organized as follows:

Chapter I introduces motivations behind this thesis writing which include the explanation of the development and benefits of DC microgrids. DC microgrid challenges that hinder DC microgrids development are elaborated. Thesis objectives are pointed out. Major contributions of this thesis are also summarized in this chapter.

Distributed EMS based DC microgrid is presented in Chapter II. Several distributed EMS strategies for DC microgrid are presented including multiple modes distributed EMS and online droop coefficient tuning control. Comprehensive experimental verifications are conducted in the lab-scale DC microgrid.

Chapter III proposes multi-level EMS based DC microgrid which consists of three levels. Each level of control is explained in detail. Seamless transition between islanded mode and grid-tied mode is evaluated. Multi-level EMS for hybrid AC/DC microgrids is also introduced.

In Chapter IV, hybridization of energy storages is investigated. Different types of energy storages based on their characteristics are introduced. Distributed and multi-level EMS for HESS are proposed. Experimental case studies in a lab-scale DC microgrid are conducted to validate the proposed EMS strategies.

Optimal depth-of-discharge range and capacity settings for battery energy storage are evaluated in Chapter V. Models of system units of DC microrids are described. System operation costs of microgrids are modelled. Detailed procedures to determine optimal depth-of-discharge range and capacity are also developed.

Chapter VI proposes real-time economic dispatch of DC microgrids. Marginal costs of all system units are described. Real-time power dispatch with prioritization is performed based on marginal cost of system units. Experimental verifications of teal-time economic dispatch are performed in a lab-scale DC microgrid.

The PhD work's conclusions are described in Chapter VII. In this chapter some future works are also expounded.

Chapter II

Distributed EMS Based DC Microgrids

2.1 Control of Each System Unit in DC Microgrids

Control of each system unit power electronic converter in DC microgrids is required to determine its operating mode configurations and power output. Elaboration of DC microgrids system units including PV, BES and NRES, are presented as follow.

2.2.1 Solar PV System Unit

A solar PV cell is modeled as a current source connected in parallel with a diode and with the addition of the shunt and series resistors [38, 39]. The equivalent circuit of a PV cell is shown in Fig. 2.1. A solar PV array consists of many PV cells connected in series and parallel.
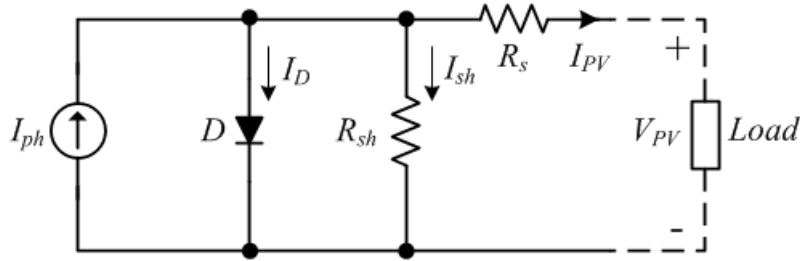
Fig. 2.1 Solar PV cell equivalent circuit.

The output current of solar PV array can be formulated as:

$$I_{PV} = n_p I_{ph} - n_p I_{sat} \times \left[\exp\left(\frac{q}{AkT_s}\left(\frac{V_{PV}}{n_s} + I_{PV}R_s \right) \right) - 1 \right] \tag{2-1}$$

$$I_{ph} = \left(I_{sso} + k_i\left(T_s - T_r \right) \right) \times \frac{S}{1000} \tag{2-2}$$

$$I_{sat} = I_{rr}\left(\frac{T_s}{T_r} \right)^3 \exp\left(\left(\frac{qE_{gap}}{kA} \right) \times \left(\frac{1}{T_r} - \frac{1}{T_s} \right) \right) \tag{2-3}$$

where:

I_{PV} Solar PV output current

V_{PV} Solar PV terminal voltage

I_{ph} Photocurrent

I_{sat} Saturation current

q Electron charge

A Ideality factor

k Boltzman constant

R_s Series resistance of a PV cell

R_{sh} Shunt resistance of a PV cell

I_{sso} Short-circuit current

k_i Short-circuit current temperature coefficient

T_r Reference temperature

T_s Surface temperature of the PV

I_{rr} Reverse saturation current at T_r

E_{gap} Band gap energy

n_p Number of solar cells in parallel

n_s Number of solar cells in series

S Solar irradiation level
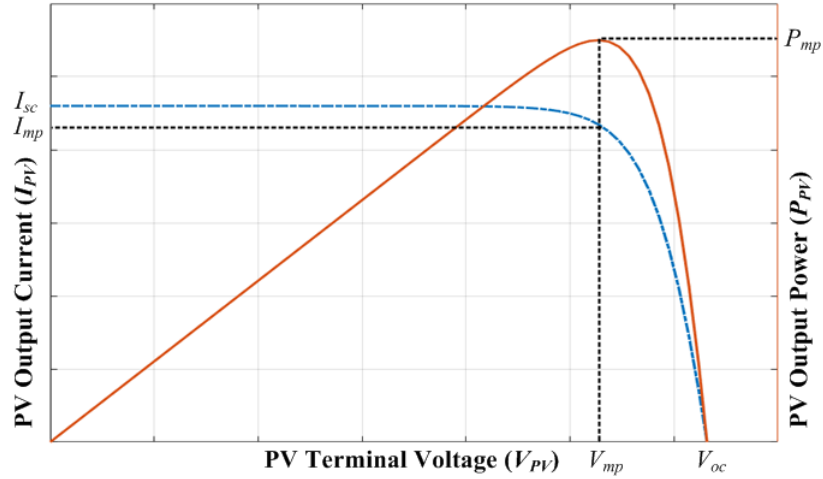
Fig. 2.2 I-V curve of solar PV.

The I-V curve of solar PV panel using PV model formulated in (2-1) – (2-3) is shown in Fig. 2.2 [40]. The short circuit current, I_{SC}, is the maximum current from a solar PV panel and occurs when the PV terminal voltage, V_{PV}, is zero. Whereas the open circuit voltage, V_{OC}, is the maximum voltage from a solar PV panel and occurs when the output current, I_{PV}, is zero. From Fig. 2.2, it can be observed that I_{PV} decreases with the increase of V_{PV}. The straight curve represents the output

power of solar PV panel which is the product of the multiplication of V_{PV} and I_{PV}. The output power increases with the increase of V_{PV} until it reaches the maximum output power (P_{mp}) [41]. After the output power has reached P_{mp}, the output power decreases with the increase of VPV. A maximum power point (MPP) exists at P_{mp} with associate PV terminal voltage of V_{mp} and output current of I_{mp}.

A boost DC-DC converter as can be seen in Fig. 2.3 is implemented for integration of solar PV panel to the DC microgrid. A controller for PV converter displayed in Fig. 2.4 manages the operation mode of PV converter. There are two modes operation of PV converter *i.e.* VRM and MPPT mode.
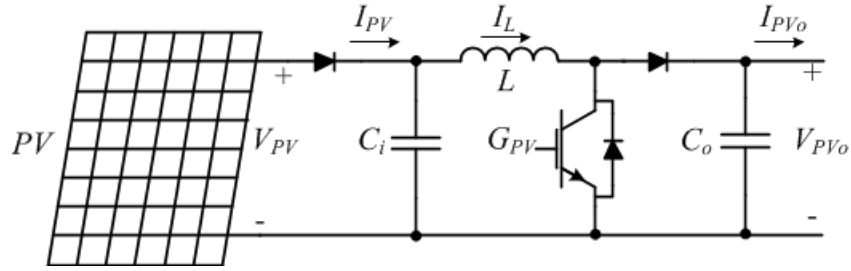
Fig. 2.3 PV converter schematic layout.
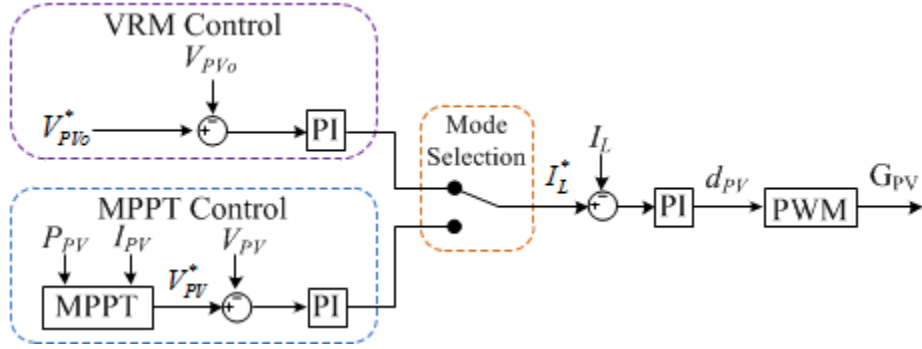
Fig. 2.4 PV converter control diagram.

<u>VRM</u>

In VRM, double-loop proportional-integral (PI) control is implemented to track the reference output voltage V_{PVo}^*. The result of the outer and inner current loop is the duty ratio for PV converter d_{PV}. Pulse width modulation (PWM) generator then produces the switching signal (G_{PV}) for the power electronic switch according to the resulted d_{PV}. The relationship between V_{PVo} and V_{PV} is:

$$V_{PVo} = \frac{1}{1 - d_{PV}} V_{PV} \tag{2-4}$$

MPPT mode

To track the maximum power of solar PV panel, various algorithms including perturb & observe (P&O), incremental conductance (IC), *etc*. have been proposed and implemented [42, 43]. The P&O algorithm is often used because of its simplicity and ease of implementation. In P&O, V_{PV} is perturbed with a small step in certain direction to obtain the corresponding PV output power. The newly obtained output power is observed and compared with the previous output power to determine whether the perturbation direction is correctly towards the MPP. The perturbation direction for the next step remains the same if the newly obtained power is higher than the previous value. Otherwise, the direction of perturbation should be inversed. Detailed procedure of P&O is described in Table 2.1.

Table 2.1 P&O procedure.

Perturbation Direction	Change of Output Power	Next Perturbation Direction
Positive	Positive	Positive
Positive	Negative	Negative
Negative	Positive	Negative
Negative	Negative	Positive

In MPPT mode, MPPT function block produces the reference terminal voltage V_{PV}^*. Double-loop PI control is also implemented to track the reference terminal voltage. The inductor current tracking in MPPT mode is the same as that in VRM. The operating mode of PV converter is selected according to the comparison of actual bus voltage with the predefined threshold value.

Table 2.2 Experimental setups of PV converter.

Component parameters	Unit	Value
Output capacitance	μF	2200
Input capacitance	μF	30
Inductance	mH	3
Switching frequency	kHz	100
Power rating	kW	15
Output voltage rating	V	450
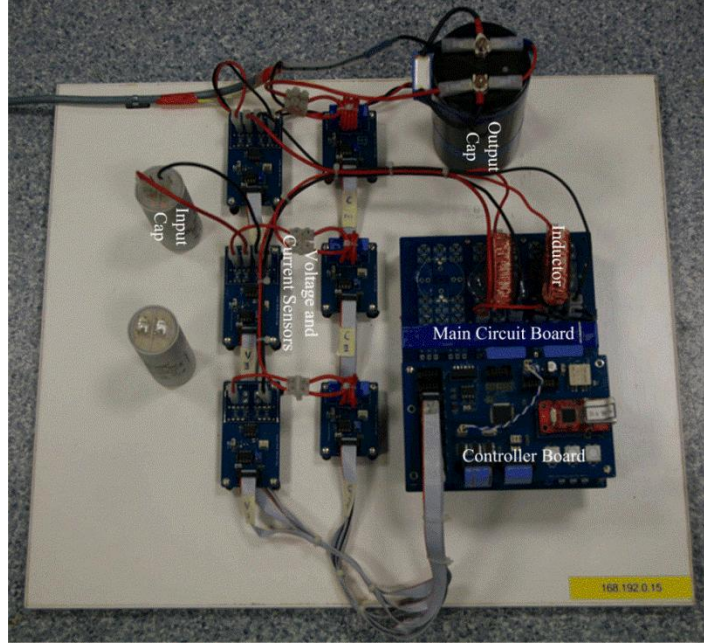
Fig. 2.5 PV converter.

Table 2.2 presents the specifications of PV converter experimental setups. The hardware setup for the multi-channel PV converter is as shown in Fig. 2.5. The multi-channel PV converter, which integrates 3 channels of PV input to operate in parallel, can be divided into two main parts including power board and controller board. The power board includes input capacitor, output capacitor, inductors, modular voltage sensors, modular current sensors and main circuit board where diodes and MOSFETs together with their drivers are installed. Modular voltage and current sensors are installed to measure the input/output voltage and current, respectively. The controller board is built based on Microcontroller C8051f930DK which enables the converter to operate with switching frequency of up to 100 KHz.

2.2.2 BES System Unit

Battery bank together with the bidirectional DC-DC converter is termed as BES system unit. BES system unit is implemented to mitigate power imbalance in DC microgrids. The BES converter schematic layout and control diagram are presented in Fig. 2.6 and Fig. 2.7. There are two modes operation of BES converter, namely VRM and PCM.

17
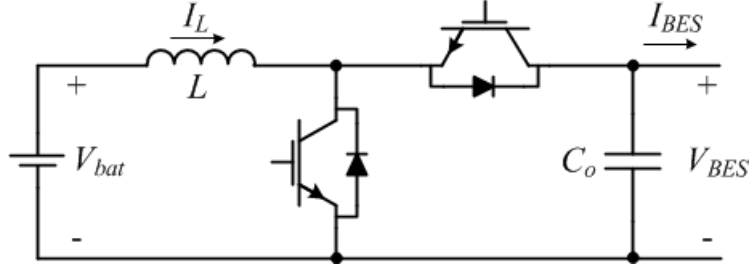
Fig. 2.6 Schematic layout of BES converter.
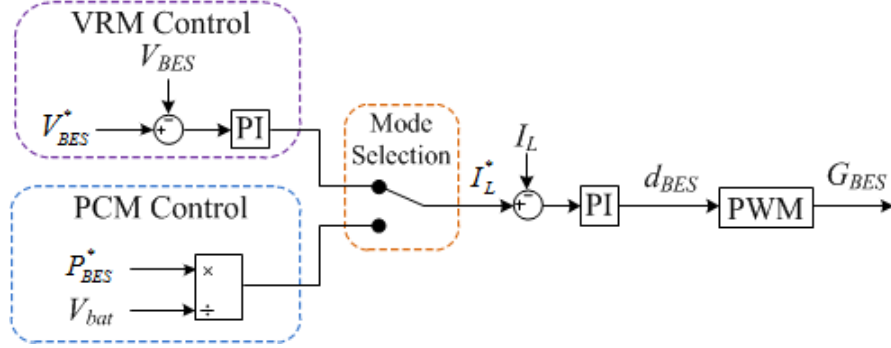
Fig. 2.7 Control diagram of BES converter.

VRM

The VRM operation of BES converter which is the same as PV converter implements the double-loop PI control.

PCM

In PCM, a PI control is implemented in the inner current loop to track I_L^* which is obtained from the division of reference BES output power P_{BES}^* by battery bank terminal voltage V_{bat}.

The BES bidirectional converter operates as boost converter and buck converter in discharging and charging stage, respectively. The upper and lower switches operate in the complementary manner.

Table 2.3 Experimental setups of BES converter.

Component parameters	Unit	Value
Switching frequency	kHz	10
Inductance	mH	10
Output capacitance	μF	2200
Power rating	kW	5
Output voltage rating	V	450

18
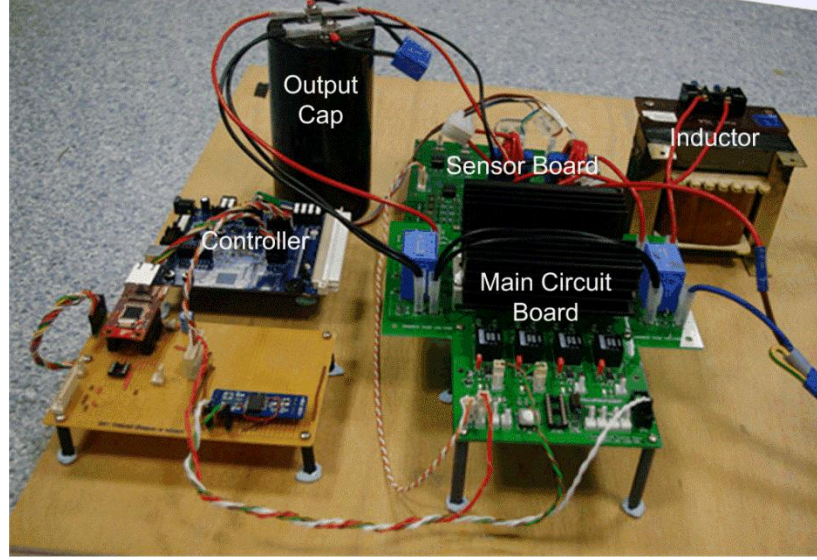
Fig. 2.8 BES converter.

Table 2.3 represents the specifications of BES converter experimental setups. The hardware setup for BES converter is as shown in Fig. 2.8. Same as PV converter, the BES converter can be divided into two main parts such as power board and controller board. The power board includes output capacitor, inductor, sensors board and main circuit board where IGBT module is installed. The C8051f120 development kit is used as the controller board to accelerate converter construction.

2.2.3   NRES System Unit

The AC-DC rectifier is required for the integration of NRES in DC microgrids since the output of fossil fuel based NRES are usually of AC. The NRES converter schematic layout and control diagram are displayed in Fig. 2.9 and Fig. 2.10, respectively.
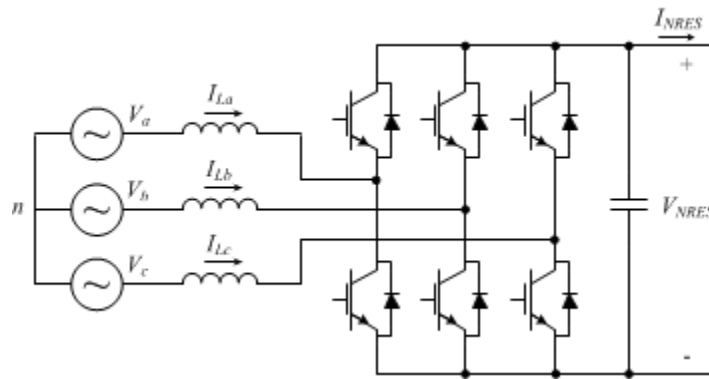
Fig. 2.9 Schematic layout of NRES converter.

19
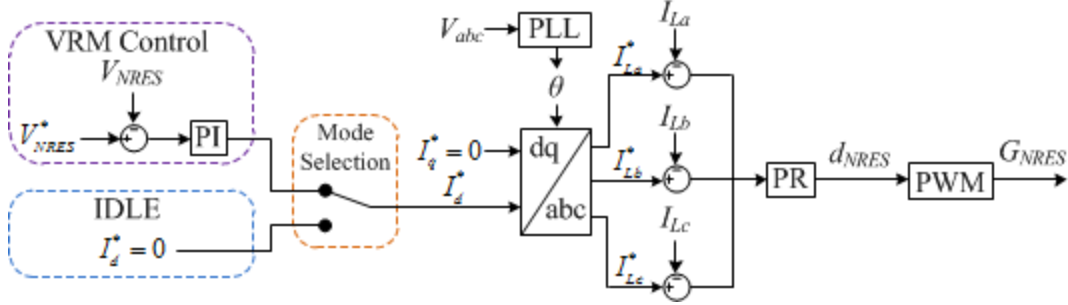
Fig. 2.10 Control diagram of NRES converter.

There are two modes operation of NRES converter *i.e*. VRM and IDLE mode. The output voltage of NRES V_{NRES} in VRM is compared with the reference value V_{NRES}^*. A PI control is implemented to produce the reference direct component of the inductor current I_d^*. Whereas in IDLE mode, I_d^* is set to be zero. Since reactive power is not exist in DC microgrids, the reference quadrature component of inductor current I_q^* is always set to be zero. Phase-locked loop (PLL) generates phase angle θ. Reference of three-phase inductor currents are obtained with dq/abc transformation. A proportional-resonant (PR) control is implemented to generate the duty ratio for NRES converter d_{NRES}. The switching signals G_{NRES} is produced by the PWM generator accordingly.

2.2 Distributed EMS

In general, EMS in DC microgrids can be classified as centralized EMS and distributed EMS. The former type of EMS is elaborated in this chapter. The later type is often realized for DC microgrid system-wide control [44-47]. In centralized EMS, one central controller has a full control of every event that occurs in the system. The central controller through the communication link gathers all system operating information including bus voltage, RESs generation, NRESs generation, load consumption, system power flow, BESs stored energy, *etc*. and assigns operating references to all system units after all data have been processed [48]. The global optimization can be realized with centralized EMS.

However, since some main drawbacks existed in centralized EMS [26, 34, 49, 50], distributed EMS is favored more to be implemented. The main benefits of

20

distributed EMS compared to centralized EMS are:

- Lower installation cost since no communication link is required.
- Higher reliability related to system malfunctions that are caused by communication link failure.
- Higher speed of response as the communication only takes place at local controller.

The global indicator for system power balance in distributed EMS of DC microgrid is bus voltage and the technique is termed as DC bus signaling (DBS). Several distributed EMS strategies which occupies DBS have been proposed [24, 41, 51-53]. The simplified equivalent circuit of the DC microgrid bus is displayed in Fig. 2.11. The capacitance represents the cumulated capacitance of output capacitors attached with all power electronic converters. The P_{Gen} and P_{Con} in Fig. 2.11 refer to system power generation and consumption, respectively, whereas P_C refers to the charging power of the system capacitor.
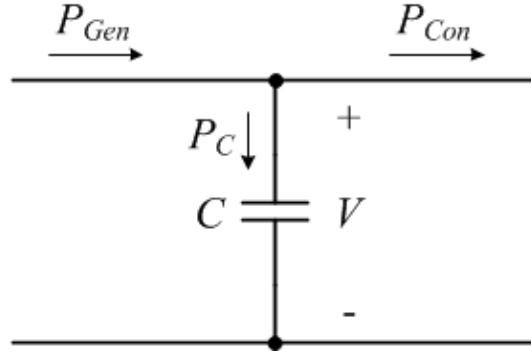
Fig. 2.11 Simplified equivalent circuit of the DC microgrid bus.

$$P_C = P_{Gen} - P_{Con} \tag{2-5}$$

For the bus voltage

$$V\frac{dV}{dt} = \frac{1}{C}\left(P_{Gen} - P_{Con}\right) \tag{2-6}$$

where C and V are the equivalent system capacitance and system bus voltage, respectively.

The interrelationship between system bus voltage and system power balance is as indicated in (2-6). Bus voltage reduction occurs when generated power is lower than consumption. On the contrary, bus voltage increment occurs when system power generation is higher than consumption. With this relationship, system bus voltage, which is available locally for all power electronic converters connected to the DC bus, can be used as global indicator of system power balance.
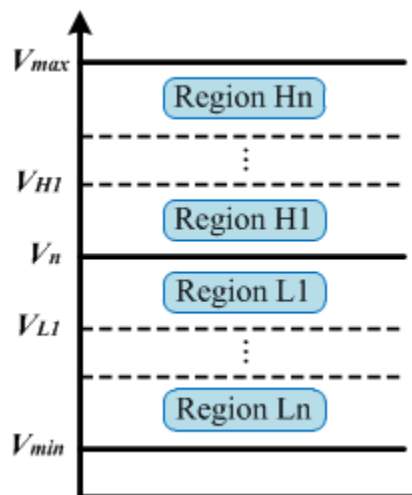
Fig. 2.12 Bus voltage range partition.

Therefore, the EMS strategy of a DC microgrid can be performed based on DC bus voltage variation. The system bus voltage range can be partitioned into several regions in order to schedule the mode operation of different system units in distributed EMS. The nominal bus voltage and allowable bus voltage range is selected according to industrial standards and government regulations [37, 54]. Fig. 2.12 shows several regions in the allowable bus voltage range that are partitioned by several threshold voltages. As can be seen in Fig. 2.12, the V_{min}, V_{L1}, V_n, V_{H1} and V_{max} are the minimum allowable bus voltage, threshold voltage for region L1, nominal bus voltage, threshold voltage for region H1 and maximum allowable bus voltage, respectively [55].

Two types of distributed EMS namely multiple modes distributed EMS and advanced multiple-slack-terminal distributed EMS are explained in this thesis.

2.3   Multiple Modes Distributed EMS

Prioritization of system units power dispatch for distributed EMS is needed for an islanded DC microgrid with the integration of renewable energy source (RES), battery energy storage (BES) and non-renewable energy source (NRES) [56]. The marginal utilization cost based prioritization is adopted [57]. The order of system units' marginal utilization cost from the lowest to the highest is RES, BES and NRES [55]. RES has the lowest marginal utilization cost because the renewable source is free, hence RES is normally controlled to be in MPPT mode. One type of NRES is diesel generator whose marginal cost is proportional to the fuel cost. The marginal utilization cost of BES is indicated with the power losses induced during charging and discharging stage.
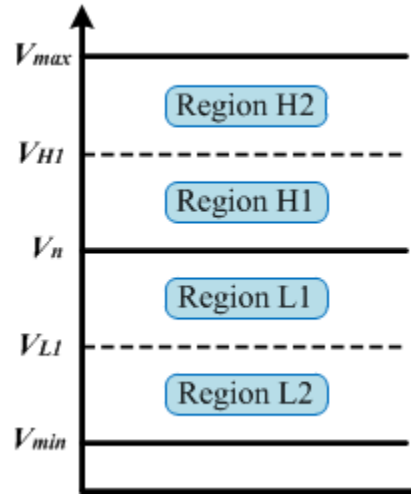
Fig. 2.13 Bus voltage range partition in multi modes distributed EMS

In general, system units can be functioned as a power terminal or a slack terminal [53]. Power terminal operates in power control mode (PCM) to track power reference in spite of the bus voltage variation whereas slack terminal operates in voltage regulation mode (VRM) to track voltage reference and maintain system power balance autonomously. Since power terminal system units are unable to maintain system power balance, at least one slack terminal must be activated throughout the operation [53, 58]. Multi modes distributed EMS divides system bus voltage range into 4 regions, *i.e.* region H2, H1, L1 and L2, with threshold bus

voltages of $V_{\min}$, V_{L1}, V_n, V_{H1} and $V_{\max}$ as can be seen in Fig. 2.13. The relationship among the threshold bus voltages is:

$$V_{\min} < V_{L1} < V_n < V_{H1} < V_{\max} \qquad (2\text{-}7)$$

Different voltage regions determine different operating modes of system units [41]. Detailed operating mode configurations of system units are shown in Table 2.4.

Table 2.4 Operating mode configurations of system units.

Region	System Unit		
	RES	BES	NRES
H2	VRM	PCM charging	IDLE
H1	MPPT	VRM charging	IDLE
L1	MPPT	VRM discharging	IDLE
L2	MPPT	PCM discharging	VRM

Region H2 with high system bus voltage indicates system power surplus. In this region since the BES charging/discharging power is power-capacity constrained, BES is controlled to operate in PCM with the maximum charging power as the power reference to avoid over-current charge which deteriorates BES lifetime operation [59]. At the same time RES is controlled to operate in VRM to prevent over-voltage damage and NRES in IDLE mode.

In region H1 and L1, RES and NRES are controlled in MPPT and IDLE modes, respectively. BES operates in VRM charging or discharging. BES operates in charging stage in region H1 when RES power generation P_{RES} is higher than load consumption P_{Load}. On the other hand when system RES generation is lower than load consumption BES operates in discharging stage.

System power deficiency is indicated in region L2 as the bus voltage is low. In this region when BES reaches the maximum discharging power, BES is controlled to operate in PCM to prevent over-current discharge. The operating mode of MPPT remains the same whereas NRES mode operation is changed from IDLE mode to VRM to retain system power balance.
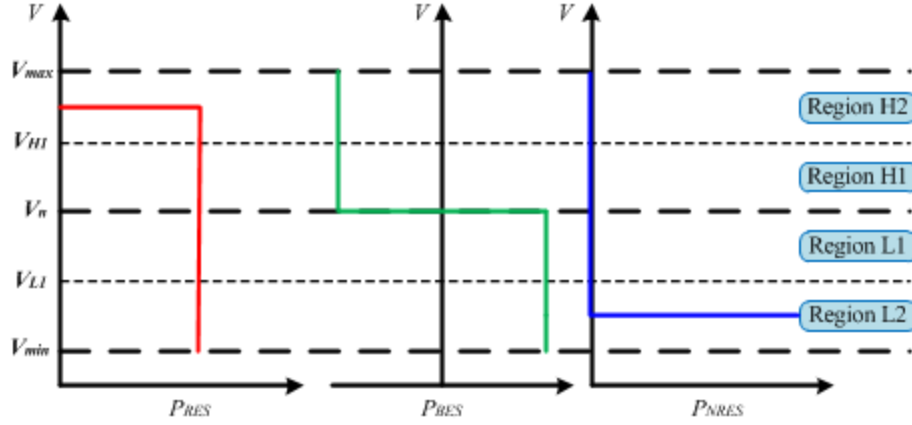
Fig. 2.14 Voltage/output relationship of system units.

The voltage-output power (*V-P*) relationship of RES, BES and NRES can be presented as in Fig. 2.14. In region H2, RES operates in VRM. RES changes to operate in MPPT mode in other regions. BES operates in PCM and its output power is remained constant at the maximum charging and discharging power in region H2 and L2, respectively. BES changes to operate in VRM with reference voltage of V_n in regions H1 and L1. NRES is scheduled to be in IDLE mode for regions L1, H1 and H2. In region L2, NRES as the backup energy source will be activated to operate in VRM.
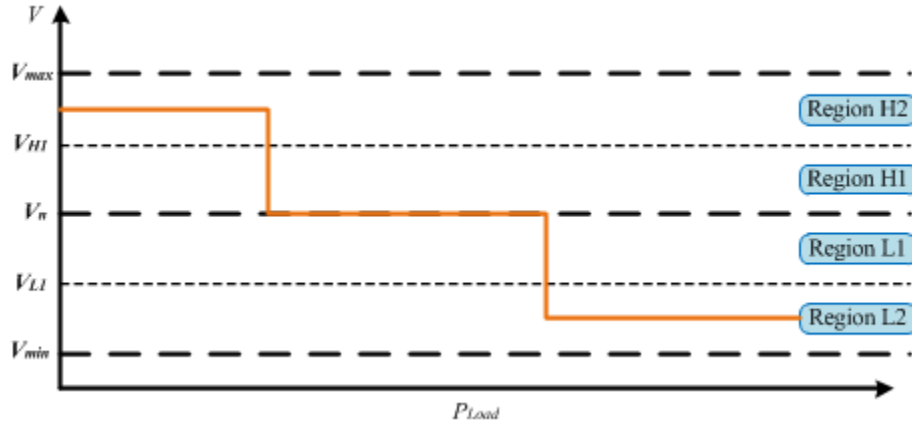
Fig. 2.15 System bus voltage-load power relationship curve.

The system power balance can represented as:

$$P_{Load} = P_{RES} + P_{BES} + P_{NRES} \tag{2-8}$$

where P_{RES}, P_{BES}, P_{NRES} and P_{Load} are the output power of RES, BES, NRES and load consumption, respectively. BES output power P_{BES} in discharging stage is

25

positive whereas in charging stage is negative. In this configuration the DC microgrid losses are neglected since the size of DC microgrid is not big, hence the system units are located relatively close one another.

With the superposition of system units' *V-P* relationship curves as can be seen in Fig. 2.14, the relationship between system bus voltage and load consumption (*V-P_{Load}*) thus can be obtained as it is displayed in Fig. 2.15. The operating region and system bus voltage can be concluded in different loading conditions intuitively using that figure.

2.4   Advanced Multiple-Slack-Terminal Distributed EMS

2.4.1   Droop Control

With the implementation of multiple modes distributed EMS as described in the previous sub-chapter, system units operating mode configuration can be realized effectively by comparison of the threshold voltages with the real-time local bus voltage. However, the discretized reference bus voltages in different bus voltage regions are existed. The mode operation change of system units and bus voltage discontinuity can cause significant bus voltage fluctuations during region transitions. In case there are multiple slack terminals which are in VRM operation in the multiple modes distributed EMS, the power sharing among them is random.

Therefore, to mitigate bus voltage discontinuity, voltage-output power (*V-P*) power droop control is employed for active power sharing among slack terminals in DC microgrid [60-66]. The concept of *V-P* droop control in DC microgrid is adopted from frequency regulation control in conventional AC utility grid [61, 67-69]. The *V-P* droop relationship can be described as:

$$V_i = V_{oi} - m_i P_i \tag{2-9}$$

where V_i is the output voltage; V_{oi} is the threshold voltage; m_i is the droop coefficient; and P_i is the output power of the ith slack terminal [70]. The nominal bus voltage V_n is usually implemented to be threshold voltage. The V_i decreases with the increase of output power and the reverse also applies. The The maximum

26

allowable voltage variation ΔV_{max} and the power capacity P_i^{max} determine the droop coefficient of slack terminals.

$$m_i = \frac{\Delta V_{max}}{P_i^{max}} \tag{2-10}$$

The relationship between the change in output voltage ΔV_i and the change in output power ΔP_i is:

$$\Delta V_i = -m_i \Delta P_i \tag{2-11}$$

With output voltages for slack terminals connected in parallel are assumed to be the same, the output voltage change denoted as system bus voltage change ΔV is:

$$\Delta V = -m_1 \Delta P_1 = -m_2 \Delta P_2 = -m_i \Delta P_i \tag{2-12}$$

In steady state the output power change becomes:

$$\Delta P_i = -\frac{\Delta V}{m_i} \tag{2-13}$$

Therefore, the output power change of the combined slack terminals ΔP can be represented as:

$$\Delta P = \sum \Delta P_i = -\sum \frac{\Delta V}{m_i} = -\Delta V \sum \frac{1}{m_i} \tag{2-14}$$

From (2-14) the combined slack terminals droop coefficient m_{eq} is:

$$m_{eq} = -\frac{\Delta V}{\Delta P} = -\frac{1}{\sum \frac{1}{m_i}} \tag{2-15}$$

So, the system bus voltage and combined output power of slack terminals P relationship can be expressed as:

$$V = V_n - m_{eq} P \tag{2-16}$$

The V-P characteristic curves of two battery energy storages $i.e.$ BES1 and BES2 are as shown in Fig. 2.16 with both operate in VRM at voltage regions H1 and L1.

The respective droop coefficients can be obtained according to (2-10). The droop coefficients of BESs in charging and discharging stage are the same since the voltage range in region L1 and H1 are the same and the magnitudes of charging and discharging power capacities are also the same.

$$m_1 = \frac{V_{H1} - V_{L1}}{P_{BES1}^{max} - P_{BES1}^{min}} \tag{2-17}$$

$$m_2 = \frac{V_{H1} - V_{L1}}{P_{BES2}^{max} - P_{BES2}^{min}} \tag{2-18}$$

where P_{BES1}^{max}, P_{BES1}^{min}, P_{BES2}^{max} and P_{BES2}^{min} are the BES1 maximum power capacity at discharging stage, the BES1 maximum power capacity at charging stage, the BES2 maximum power capacity discharging, and the BES2 maximum power capacity at charging stage, respectively.
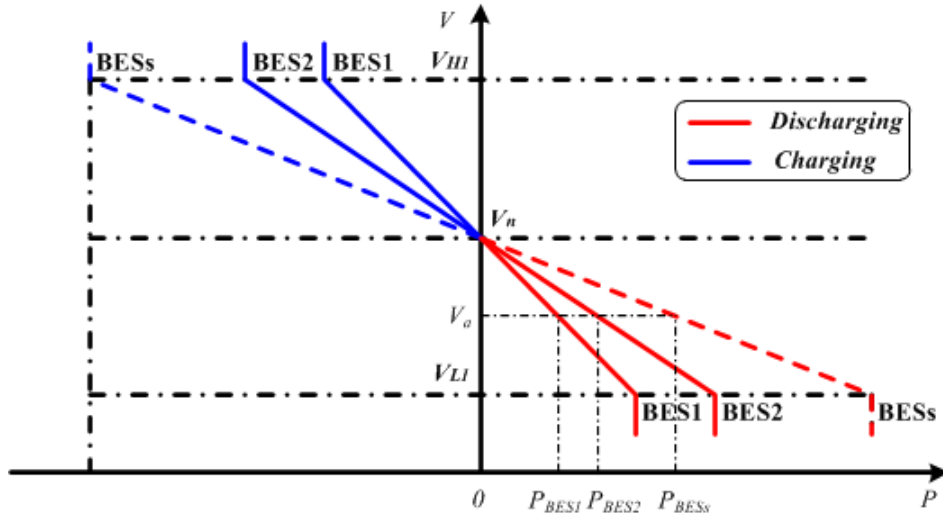
Fig. 2.16 BESs *V-P* characteristic curves.

Using *V-P* characteristic curves, the respective output powers of BES1 and BES2 can be obtained intuitively according to the given system bus voltage. The combined output power of BESs can thus be generated from the superposition of output powers of BES1 and BES2 which is presented as the dash curves in Fig. 2.16. With the combined output power of P_{BESs}, system bus voltage will be regulated at V_a with corresponding BES1 and BES2 output powers of P_{BES1} and P_{BES2}, respectively.

Droop control enables active power sharing among slack terminals. Unlike the discretized bus voltage in multiple modes distributed EMS explained in the previous sub-chapter, system bus voltage in droop control can be scheduled to be continuous so that voltage variation can be reduced significantly during the voltage region transitions.

V-P relationship of system units for each region

The *V-P* characteristic curves with droop control of DC microgirds consisted of RESs, BESs and NRES are displayed in Fig. 2.17. BESs operate in PCM at voltage regions H2/L2 and in VRM at voltage regions H1/L1. The BESs output power and bus voltage relationships in different voltage regions are described as follows:

$$
P_{BESs} = \begin{cases}
P_{BESs}^{\min} & (V_{H1} < V \leq V_{\max}) \\
\dfrac{V - V_n}{V_{H1} - V_n} P_{BESs}^{\min} & (V_n < V \leq V_{H1}) \\
\dfrac{V_n - V}{V_n - V_{L1}} P_{BESs}^{\max} & (V_{L1} \leq V \leq V_n) \\
P_{BESs}^{\max} & (V_{\min} \leq V < V_{L1})
\end{cases}
\tag{2-19}
$$

where V_{max} and V_{min} are the upper and lower limit of allowable bus voltages, respectively; $P_{BESs}^{\max}$ is the BESs maximum power capacity in discharging stage; and $P_{BESs}^{\min}$ is the BESs maximum power capacity in charging stage. The *V-P* characteristic of BESs can be displayed in Fig. 2.17(b).
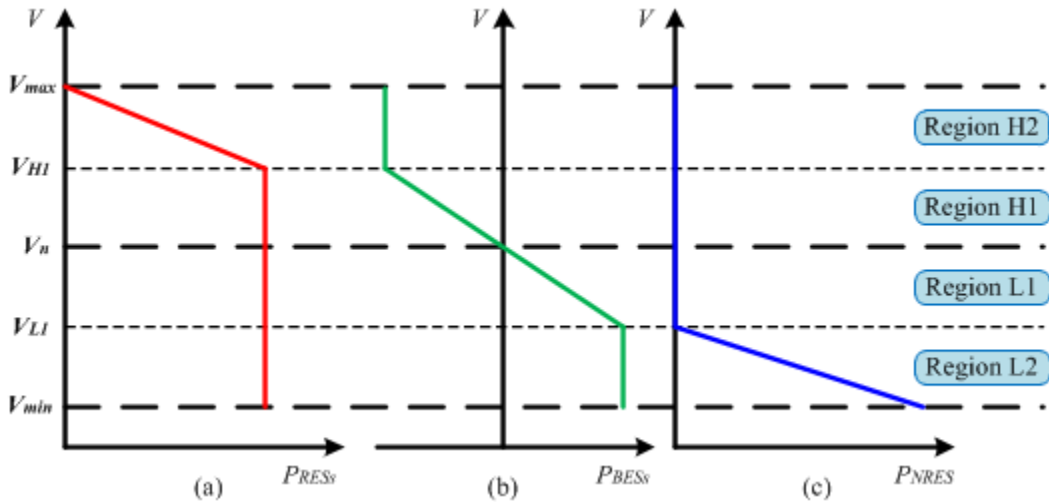
Fig. 2.17 *V-P* characteristics of (a) RESs, (b) BESs and (c) NRES.

Likewise, the RESs and NRES output power and bus voltage relationships for each region are:

$$P_{RESs} = \begin{cases} \dfrac{V_{\max} - V}{V_{\max} - V_{H1}} P_{RESs}^{\max} & (V_{H1} < V \leq V_{\max}) \\ P_{RESs}^{\max} & (V_{\min} \leq V \leq V_{H1}) \end{cases}$$ (2-20)

$$P_{NRES} = \begin{cases} 0 & (V_{L1} \leq V \leq V_{\max}) \\ \dfrac{V_{L1} - V}{V_{L1} - V_{\min}} P_{NRES}^{\max} & (V_{\min} \leq V < V_{L1}) \end{cases}$$ (2-21)

where $P_{RESs}^{\max}$ is the RESs rated power capacity; $P_{NRES}^{\max}$ is the NRES rated power capacity. The *V-P* characteristic of RESs is displayed in Fig. 2.17(a) whereas for NRES is displayed in Fig. 2.17(c).

In steady state, bus voltage variation is eliminated when system power is balanced. The system power balance is:

$$P_{Load} = P_{RESs} + P_{BESs} + P_{NRES}$$ (2-22)

where P_{Load}, P_{RESs}, P_{BESs} and P_{NRES} are the system load consumption, output power of RESs, BESs, and NREs respectively. The aggregation of (2-19) − (2-21) illustrates load consumption and bus voltage relationship:

$$P_{Load} = \begin{cases} P_{BESs}^{\min} + \dfrac{V_{\max} - V}{V_{\max} - V_{H1}} P_{RESs}^{\max} & (V_{H1} < V \leq V_{\max}) \\ \dfrac{V - V_n}{V_{H1} - V_n} P_{BESs}^{\min} + P_{RESs}^{\max} & (V_n < V \leq V_{H1}) \\ \dfrac{V_n - V}{V_n - V_{L1}} P_{BESs}^{\max} + P_{RESs}^{\max} & (V_{L1} \leq V \leq V_n) \\ P_{BESs}^{\max} + P_{RESs}^{\max} + \dfrac{V_{L1} - V}{V_{L1} - V_{\min}} P_{NRES}^{\max} & (V_{\min} \leq V < V_{L1}) \end{cases}$$ (2-23)

System *V-P* characteristic can thus be displayed in Fig. 2.18. The maximum bus voltage when load consumption is equal to zero is:

$$V = V_{\max} + \frac{P_{BESs}^{\min}}{P_{RESs}^{\max}} (V_{\max} + V_{H1})$$ (2-24)

30
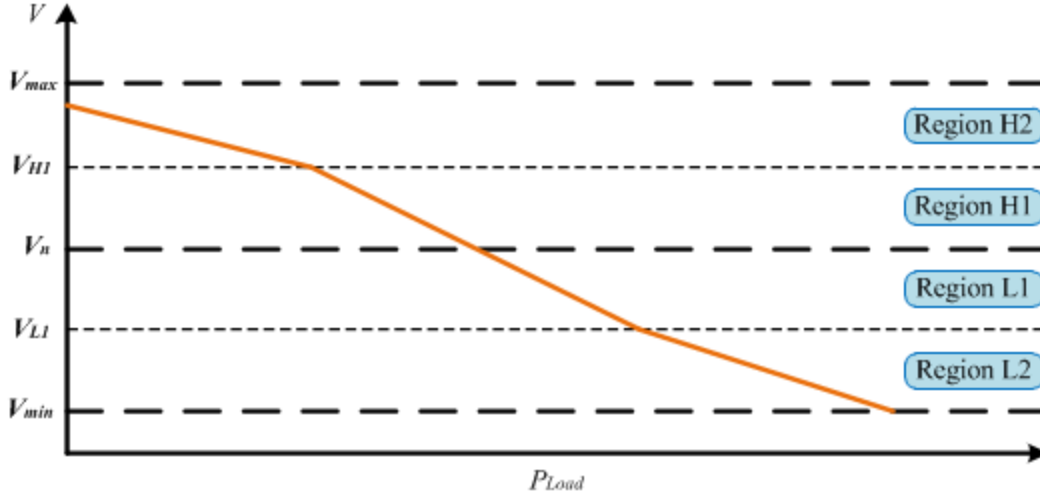
Fig. 2.18 System V-P characteristic curve.

Fig. 2.18 shows that system bus voltage increases when the load consumption decreases.

2.4.2 Partition of Bus Voltage Regions Based on Power Capacity

The *V-P* characteristic curves of islanded DC microgrid system units RESs, BESs and NRES, are displayed in Fig. 2.17. System bus voltage band is partitioned into four regions and the threshold bus voltages are usually fixed from certain percentage of bus voltage variation of the nominal value [41, 51, 53, 71, 72]. The mode operations of system units are similar as in the multiple modes distributed EMS as described in Table 2.4.
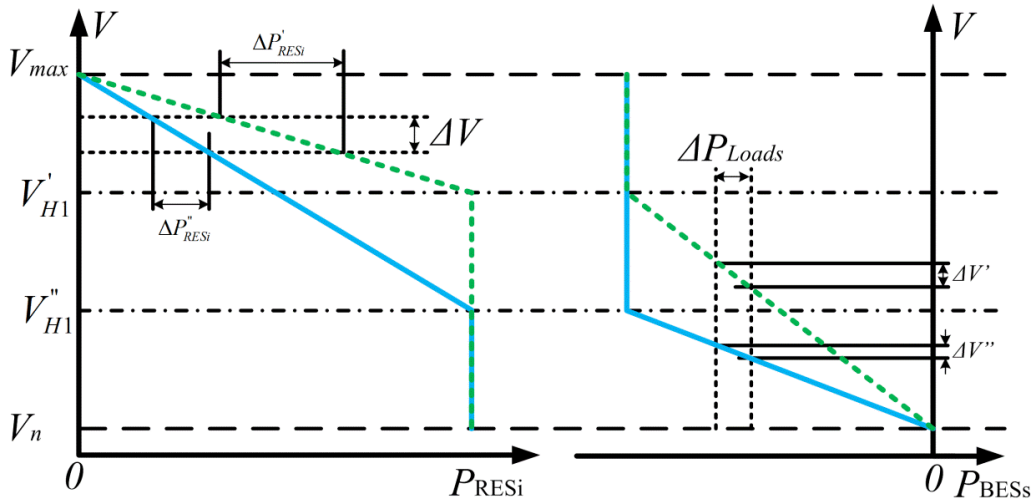
Fig. 2.19 Effect of different threshold voltage values selection.

31

Fig. 2.19 illustrates the effect of different V_{H1} settings. The V-P characteristic of the ith RES and BESs with different threshold voltages settings $i.e.$ V'_{H1} and V''_{H1}, are as can be seen in the figure. The dashed and solid curves represent V-P characteristic with V'_{H1} and V''_{H1}, respectively.

Capacity-based proportional power sharing is able to be realized precisely assuming that system bus voltage is uniform along system bus. However, the local voltages of all system units are not the same in actual implementation because of transmission line impedance and measurement errors. Therefore, power sharing error is induced. The power sharing error of RESi in region H2 due to bus voltage difference of ΔV as in Fig. 2.19 is:

$$\Delta P_{RESi} = \frac{\Delta V}{-m_{RESi}} = -\frac{\Delta V \times P_{RESi}^{max}}{V_{max} - V_{H1}} \tag{2-25}$$

where ΔP_{RESi} and P_{RESi}^{max} are the power sharing error and the maximum power of RESi, respectively. The power sharing error is inversely proportional to the width of region H2 voltage band. The narrower band of the voltage region, the larger power sharing error will be resulted. As can be seen in Fig. 2.19 magnitude of $\Delta P'_{RESi}$ is much larger compared with $\Delta P''_{RESi}$.

The droop gradient of BESs V-P characteristic at region H1 is the same as that of system V-P_{Loads} curve. Therefore, system bus voltage change because of load power variation ΔP_{Loads} can be represented as follows:

$$\Delta V = -\Delta P m_{BESs} = \Delta P_{Loads} \frac{V_{H1} - V_n}{P_{BES}^{min}} \tag{2-26}$$

The larger band of the voltage region, the larger bus voltage change will be resulted. As can be seen in the Fig. 2.19 $\Delta V'$ is wider compared to $\Delta V''$. To conclude, the narrow voltage region band results in significant power sharing error. However, the large voltage region band results in significant system voltage variation.

Therefore, partition of bus voltage regions based on power capacity is proposed to avoid both exaggerate bus voltage variation because of load change and slack

terminal power sharing error because of transmission line impedance. The selection of threshold voltages V_{H1} and V_{L1} are made to equalize the droop coefficients in different regions. The equivalent droop coefficient of system V-P_{Loads} curve m_{eq} for each bus voltage region is:

$$m_{eq} = \begin{cases} \dfrac{V_{max} - V_{H1}}{P_{RESs}^{max}} & (V_{H1} < V \leq V_{max}) \\[3mm] \dfrac{V_n - V_{H1}}{P_{BES}^{min}} & (V_n < V \leq V_{H1}) \\[3mm] \dfrac{V_n - V_{L1}}{P_{BESs}^{max}} & (V_{L1} \leq V \leq V_n) \\[3mm] \dfrac{V_{L1} - V_{min}}{P_{NRES}^{max}} & (V_{min} \leq V < V_{L1}) \end{cases} \quad (2\text{-}27)$$

The V_{H1} is obtained from the equalization of region H1 and H2 droop coefficients:

$$V_{H1} = V_n + \frac{(V_n - V_{max})P_{BESs}^{min}}{P_{RESs}^{max} - P_{BESs}^{min}} \quad (2\text{-}28)$$

Accordingly, V_{L1} is obtained from the equalization of region L1 and L2 droop coefficients:

$$V_{L1} = V_n - \frac{(V_n - V_{min})P_{BESs}^{max}}{(P_{BESs}^{max} + P_{NRES}^{max})} \quad (2\text{-}29)$$

2.4.3 Online Droop Coefficient Tuning

Discontinuity in bus voltage

The threshold voltages V_{H1} and V_{L1} are generated to partition the voltage regions according to the rated power capacities of system units. However, the real-time power capacity of RESs differs depending on weather conditions. As RESs operate in VRM in region H2, the real-time V-P droop relationship is:

$$V(t) = V_{max} - \frac{V_{max} - V_{H1}}{P_{RESs}^{max}} P_{RESs}(t) \quad (2\text{-}30)$$
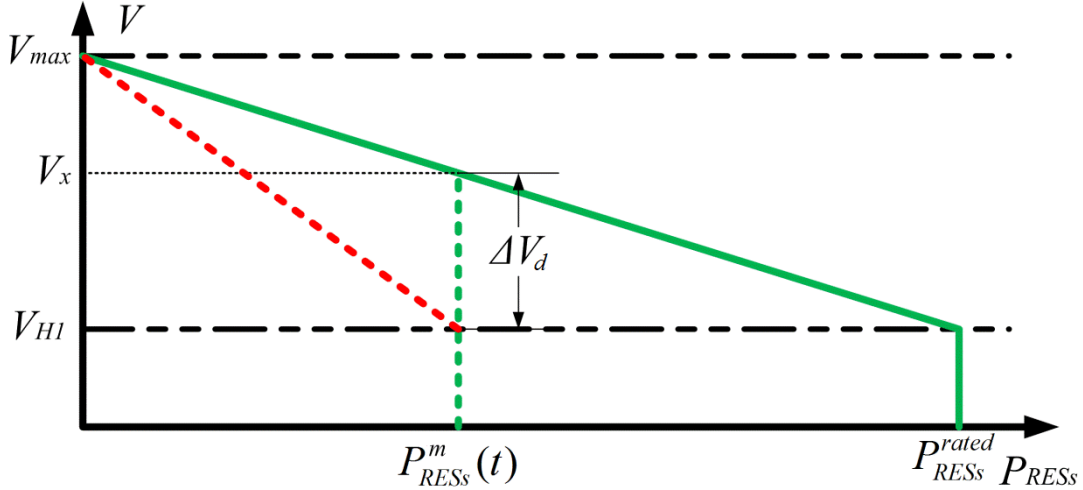
Fig. 2.20 Discontinuity in bus voltage because of RESs power capacity variation.

With the assumption that the real-time RESs power capacity $P_{RESs}^{m}(t)$ is lower than the rated value $P_{RESs}^{\max}$, RESs reaches the maximum output power $P_{RESs}^{m}(t)$ at bus voltage V_x as illustrated in Fig. 2.20.

$$V_x = V_{\max} - \frac{V_{\max} - V_{H1}}{P_{RESs}^{\max}} P_{RESs}^{\mathrm{m}}(t) \qquad (2\text{-}31)$$

With the existence bus voltage discontinuity, system bus voltage is not be able to be controlled actively resulted in system bus voltage jumps from V_x to V_{H1} during the voltage region transition from H2 to H1. The voltage gap ΔV_d between V_x and V_{H1} is:

$$\Delta V_d = V_x - V_{H1} = \frac{(V_{\max} - V_{H1})(P_{RESs}^{\max} - P_{RESs}^{\mathrm{m}}(t))}{P_{RESs}^{\max}} \qquad (2\text{-}32)$$

To mitigate the bus voltage discontinuity, real-time RESs power capacity based droop coefficient tuning is thus proposed. The updated droop coefficient of RESs becomes:

$$m_{RESs}(t) = \frac{V_{\max} - V_{H1}}{P_{RESs}^{m}(t)} \qquad (2\text{-}33)$$

With (2-33), the *V-P* characteristic curve of RESs in region H2 is represented by the red-dashed curve in Fig. 2.20. Implementation the proposed droop coefficient

34

tuning method ensures the continuity of system bus voltage during region transition.

Likewise, BESs power capacities in both charging and discharging stage also change according to the real-time state of charge (SoC). The droop coefficients of BESs in region H1 and L1 should thus be updated accordingly as the RESs as represented in (2-33). The droop coefficient of NRES remains unchanged since its power capacity is considered constant.

Solar PV power capacity estimation

The real-time power capacities of system units are necessary for droop coefficient tuning. Estimation of the real-time power capacities is conducted because of the difficulty to obtain the real value of the real-time power capacities. The instantaneous output power can be assigned as the real-time power capacity only when PV converter functions in MPPT mode. However, when PV converter is in VRM which is in region H2, its power capacity is difficult to determine. A novel method to estimate $P_{PVi}^{\mathrm{m}}(t)$ is proposed based on P_{PV}-V_{PV} characteristic curve as displayed in Fig. 2.21.
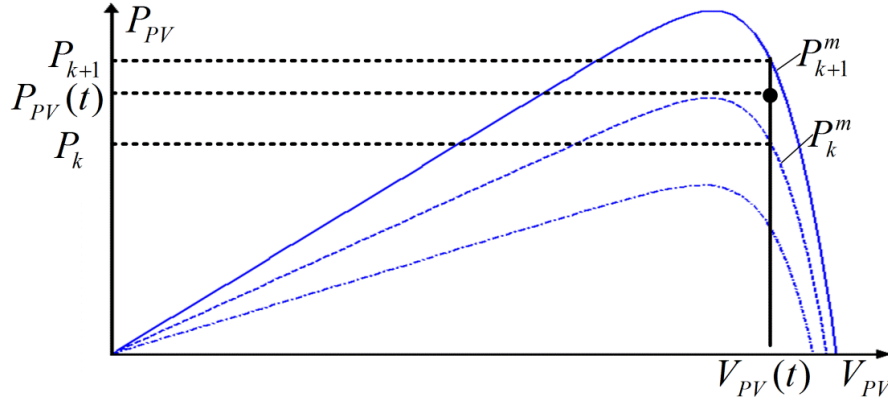
Fig. 2.21 Estimation of real-time PV power capacity in region H2.

Different solar irradiation conditions which result in different P_{PV}-V_{PV} characteristic curves of solar PV are displayed in Fig. 2.21. The instant terminal voltage and output power are $V_{PV}(t)$ and $P_{PV}(t)$, respectively. With curves k and $k+1$

represent PV output characteristics in solar irradiation levels of k and $k+1$, the power capacities are $P_k^{\max}$ and $P_{k+1}^{\max}$, respectively with the terminal voltage is $V_{PV}(t)$.

$$P_k \leq P_{PV}(t) \leq P_{k+1} \tag{2-34}$$

The estimation of solar PV real-time power capacity $P_{PVi}^m(t)$ is performed using linear interpolation, as described as follows:

$$P_{PVi}^m(t) = P_{k+1}^m - \frac{P_{k+1} - P_{PV}(t)}{P_{k+1} - P_k}(P_{k+1}^m - P_k^m) \tag{2-35}$$

The more accurate estimation will be resulted if the more P_{PV}-V_{PV} characteristic curves with different solar irradiation levels are incorporated. The droop coefficients in region H2 are updated according to the estimated solar PV power capacities.

The modified PV converter control diagram is displayed in Fig. 2.22. The operation in MPPT mode is the same as explained in the multiple mode distributed EMS.
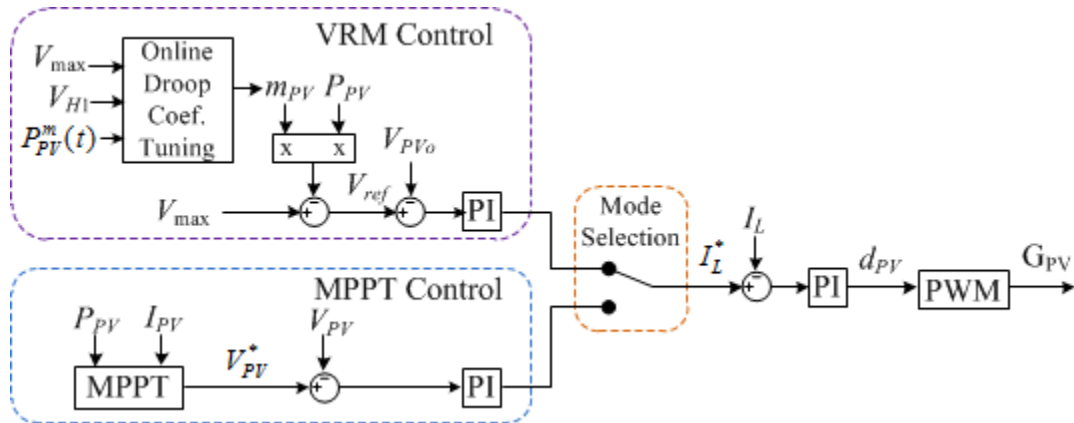
Fig. 2.22 PV converter control diagram with online droop coefficient tuning.

In VRM, $P_{PVi}^m(t)$ is obtained to produce the droop coefficient m_{PV}. The V_{ref} is thus obtained according to (2-9). Double-loop PI control is implemented to track the V_{ref} and produce the respective duty ratio to the converter.

Estimation of BES power capacity

Likewise, estimation of real-time power capacity of BES which depends on its

36

stored energy normally indicated with SoC is also required for online droop coefficient tuning [73]. Because of the simplicity, terminal voltage together with coulomb counting methods are often used to estimate the SoC of battery [74].

Constant current–constant voltage (CC-CV) charging scheme displayed in Fig. 2.23 is usually performed for BES charging [75-77]. The battery is charged with constant current in the first stage until the terminal voltage has reached a threshold value (SoC is 70-80%). In this stage, battery terminal voltage increases with the increase of SoC. Battery constant voltage charging which is the second stage is activated when the terminal voltage has reached a threshold value. In this stage, the charging current reduces with the increase of SoC. When the predefined cutoff current has reached, battery is considered fully charged. Therefore BES power capacity and SoC relationship could be obtained as illustrated by the dashed curve in Fig. 2.23.
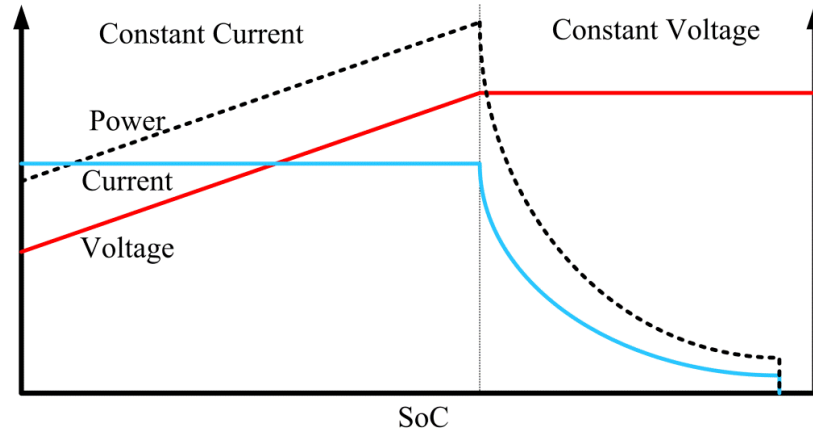
Fig. 2.23 BES two-stage charging process.

The modified BES converter control diagram is displayed in Fig. 2.24. When BES converter operates in PCM in regions L2 and H2, the reference output power is set to be $P_{BES}^m(t)$. After that the same procedure as in multiple modes distributed EMS applied to produce the duty ratio for the respective converter. As BES is in VRM at regions L1 and H1, the droop coefficient is updated according to the estimation of real-time power capacity implementing online droop coefficient tuning. Double-loop PI control is implemented to track the V_{ref} and produce the duty ratio for the respective converter.

37
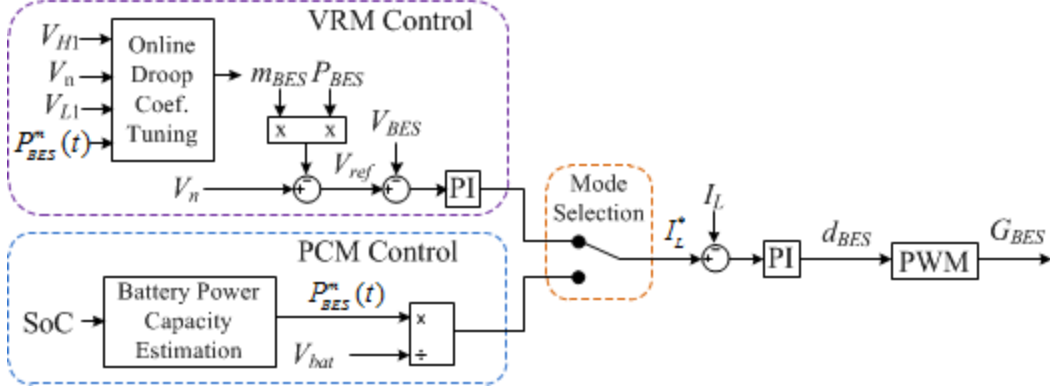
Fig. 2.24 BES converter control diagram with online droop coefficient tuning

The droop coefficients of the slack terminals in different voltage regions are updated according to the real-time power capacities by implementing online droop coefficient tuning method. The system load consumption and voltage bus relationship is described as follows:

$$P_{Loads} = \begin{cases} \dfrac{V_{\max} - V}{V_{\max} - V_{H1}} P_{RESs}^m(t) - P_{BESs}^m(t) & (V_{\max} \geq V > V_{H1}) \\[2ex] P_{RESs}^m(t) - \dfrac{V - V_n}{V_{H1} - V_n} P_{BESs}^m(t) & (V_n < V \leq V_{H1}) \\[2ex] \dfrac{V_n - V}{V_n - V_{L1}} P_{BESs}^m(t) + P_{RESs}^m(t) & (V_{L1} \leq V \leq V_n) \\[2ex] P_{BESs}^m(t) + P_{RESs}^m(t) + \dfrac{(V_{L1} - V)}{V_{L1} - V_{\min}} P_{NRES}^{\max} & (V_{\min} \leq V < V_{L1}) \end{cases} \tag{2-36}$$

2.5 Experimental Verifications

2.5.1 Multiple Modes Distributed EMS

A lab-scale DC microgrid in Water and Energy Research Laboratory (WERL), School of Electrical and Electronic Engineering, Nanyang Technological University, Singapore, as displayed in Fig. 2.25 has been developed to validate the effectiveness of the proposed multiple modes distributed EMS operation. System bus consists of 8 circuit panels which are configured in a ring network. Each circuit panel serves as a remote terminal unit (RTU) in which AC and DC plugs are installed for integration of various system units.

For the experimental verification purpose, two Agilent E4360A Modular Solar Array Simulators (SAS) with 2.4 kW combined power capacity are installed as the renewable energy source. SAS is capable of emulating the output of PV panel with the desired I-V characteristic. The I-V characteristic can be based on the given open-circuit voltage V_{oc}, short-circuit current I_{sc}, maximum power voltage V_{mp} and current I_{mp}. The variation output of PV panel can also be emulated by switching between different I-V curves. PV converter as described in Fig. 2.5 is employed to integrate the PV panel into the DC microgrid.
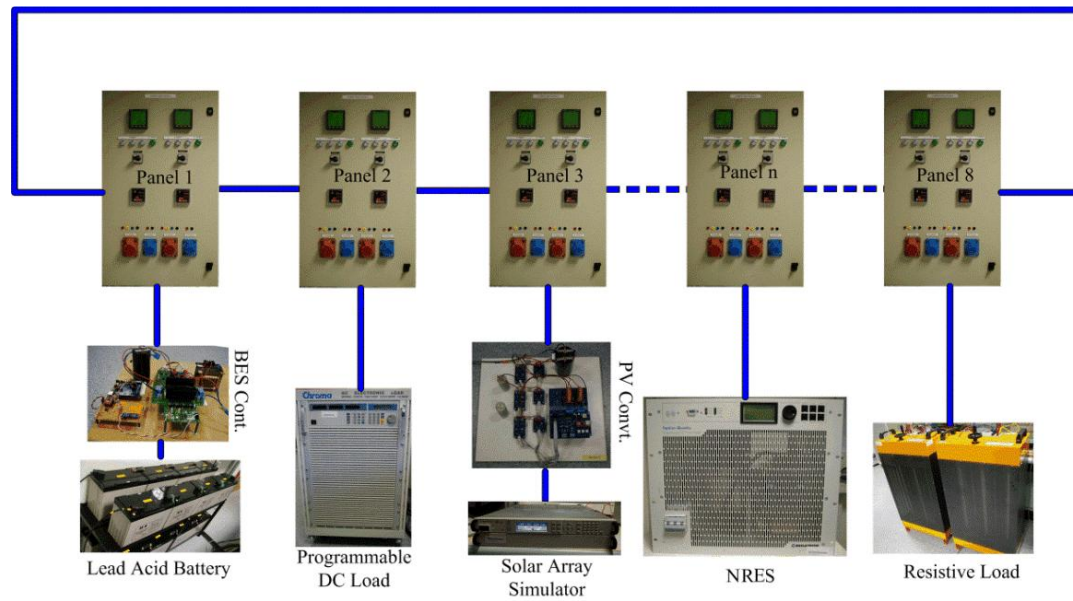
Fig. 2.25 The lab-scale DC microgrid schematic diagram.

Lead-acid battery bank, comprised of 16 battery cells connected in series, is implemented as BES. The nominal terminal voltage and capacity of each battery cell are 12 V and 200 Ah, respectively. Therefore, the nominal terminal voltage of the battery bank is 192 V. Battery management system (BMS) with functionalities including state of charge (SoC) estimation, cell SoC equalization, *etc.* is installed to optimize the utilization of BES. BES converter presented as in Fig. 2.8 is employed to control the output of BES. In this case, the power capacities of BES both at charging and discharging stages are limited by the maximum inductor current of 10 A. Therefore, to guarantee the safety of the operation, the BES maximum power capacity is set to be 1.6 kW.

39

To simulate different loading profiles, Chroma programmable load and resistive load bank are employed. The Chroma programmable load has several mode configurations including constant resistance, constant current and constant power modes to mimic different kinds of loads.

Chroma DC power supply is employed to emulate NRES in this case. NRES operates in IDLE mode in normal state and can be activated to operate in VRM autonomously when system power deficiency is detected.

The nominal bus voltage of 380 VDC has been implemented for application of data center is specified in microgrid specifications draft V. 0.14 published by REbus Alliance in 2011 [7, 37]. Therefore, the nominal bus voltage for DC microgrid operation throughout the thesis is selected to be 380 V. With the allowable bus voltage range is about ±5% of the nominal bus voltage, the respective reference output voltage of RES, BES and NRES in VRM are 400 V, 380 V and 360 V. To verify multiple modes distributed EMS, two experimental case studies have been conducted as follows:

Case 1

In Case 1 system transition between voltage regions H1 and L1 is verified. The setting of resistive load bank is to be 144.4 Ω and programmable load is configured with constant power consumption of 1 kW. The experimental results including V_{BES}, I_{BES}, V_{bat}, I_L and P_{BES}, are acquired with LeCroy oscilloscope as shown in Fig. 2.26. V_{BES}, I_{BES}, V_{bat}, I_L and P_{BES} refer to BES output voltage, BES output current, battery bank terminal voltage, inductor current and output power of BES, respectively.

At the first time, with only the resistive load bank that was turned on, bus voltage was retained by BES at 380 V. Resistive load bank consumed 1 kW of power according this nominal bus and the output power of PV converter was 1.6 kW. Because there is a power surplus in the DC microgrid, BES scheduled in charging stage with power magnitude of 0.6 kW. System bus voltage was at region H1 and regulated at the nominal value steadily. The wide band of inductor current was due to the switching process of the BES converter.
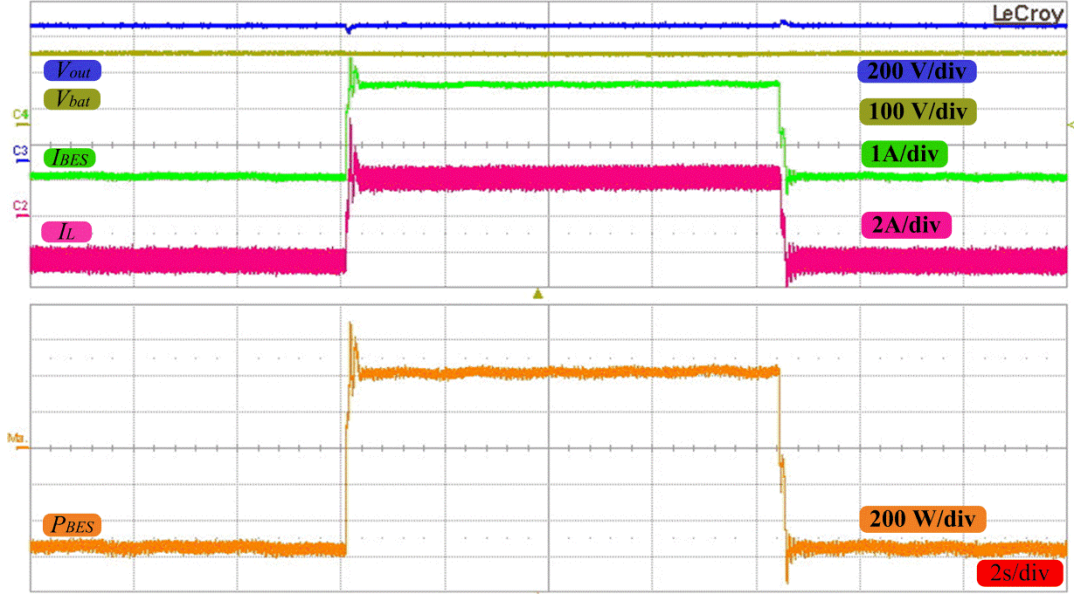
Fig. 2.26 Experimental results of system transition between voltage regions H1 and L1.

The programmable load was turned on at 6 s, hence BES output power raised by 1 kW instantly to maintain system power balance. RES still operated in MPPT mode. Fluctuations of BES output current appeared because of BES response lag. During the transition, system bus voltage sag was observed for duration of 0.17 s due to instant system power deficiency. At steady state, BES discharged power of 0.4 kW to stabilize system power balance. System bus voltage at this condition was at region L1 and remained at the nominal value.

At 14.2s the programmable load was back to be switched off. Therefore, BES returned back to charging stage instantly to keep system power balance. During the transition, bus voltage surge can be observed because of excess power in the system. Bus voltage was back to region H1 and maintained at the nominal value in steady state.

Case 2

Experimental Case 2 observed mode operation changes of system units at different bus voltage regions. The experimental results including V_{BES}, I_{BES}, V_{bat}, I_L and P_{BES}, are shown in Fig. 2.27. RES output power capacity was increased to be 2.2 kW. Resistance of resistive load bank and power rating of programmable load were set to be 240 Ω and 0.3 kW, respectively.

41

Both the programmable load and resistive load bank are connected to system bus in the beginning, resulted in 0.9 kW of load consumption. Since the load consumption is lower than PV generation and the difference is lower than the charging capacity, BES operated in VRM at nominal value with 1.3 kW of charging power.
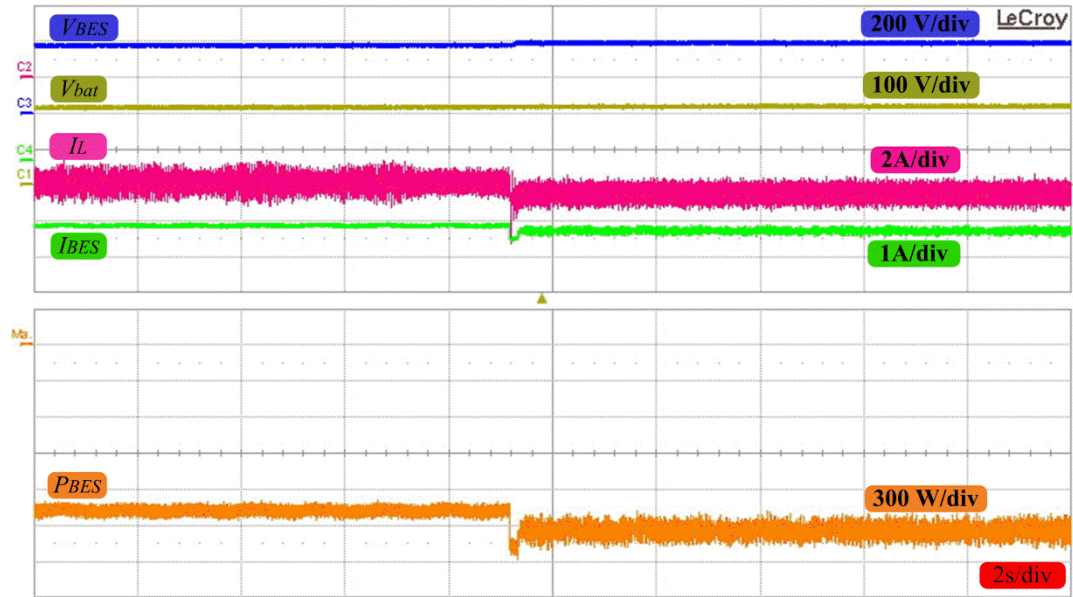
Fig. 2.27 Experimental results of operating mode change.

At 9.6s, the programmable load was switched off. To regulate system bus voltage, BES charging power was thus increased immediately. As the charging power has reached the maximum power capacity value of 1.6 kW, BES changed to PCM with the maximum charging power (1.6 kW) as the power reference. The threshold power of mode change was set 10% higher than the maximum charging power to prevent undesired operating mode change of BES due to power fluctuations. This explains the reason for BES output power surge during the transition.

At the time BES changed to PCM, BES and RES operated as power terminals. In this case, power surplus induces system bus voltage increase. When system bus voltage reached the threshold value for PV converter operating mode change which is 400 V, PV changes to VRM with reference voltage of 400 V. System was stabilized with bus voltage of 400 V with PV converter operated in VRM and BES operated in PCM.

Experimental cases have exhibited the effectiveness of the multiple modes

42

distributed EMS. Operating mode configuration of system unit can be realized effectively and autonomously.

2.5.2 Advanced Multiple-Slack-Terminal Distributed EMS

To validate the effectiveness of the proposed EMS strategy, the same lab-scale DC microgrid as displayed in Fig. 2.25 is used for experimental verifications. The experimental specifications are presented in Table 2.5.

Table 2.5 Experimental specifications.

Parameter	Unit	Setting
System Bus Equivalent Capacitance	μF	4000
Nominal Bus Voltage	V	380
Allowable Voltage Variation	V	±20
PVs Rated Power Capacity	kW	2
BES Rated Power Capacity	kW	1
BES Energy Capacity	kWh	10
NRES Rated Power Capacity	kW	2

Case 1

The comparison of operations between implementation of the conventional and the proposed power capacity based bus voltage partition is demonstrated in Case 1. In the conventional partition, the threshold voltage V_{H1} and V_{L1} are set to be 390 V and 370 V, respectively, so that the widths of all voltage regions can be equalized. The droop coefficients at H2, H1, L1 and L2 can thus be obtained to be 5 V/kW, 10 V/kW, 10 V/kW and 5 V/kW according to (2-10). Fig. 2.28 displayed the experimental results including system bus voltage, PV output power, BES output power and load consumption.

In the beginning, the system loads were activated with total power consumption of 2.5 kW. PV converter generated power of 2 kW. Therefore, BES converter regulated bus voltage by discharging power in the amount of 0.5 kW. System bus voltage V was regulated at 375 V and system operated in L1.

Later on, the system loads were reduced to 1.5 kW At 2 min. Consequently, BES converter rebalanced system power by changing to charging stage with the amount power of 0.5 kW. During the load change, an insignificant voltage swell was

43

observed due to the response delay of BES converter. After 1 kW load reduction, system bus voltage was stabilized at 385 V with voltage increment 10 V compared to the previous stage.
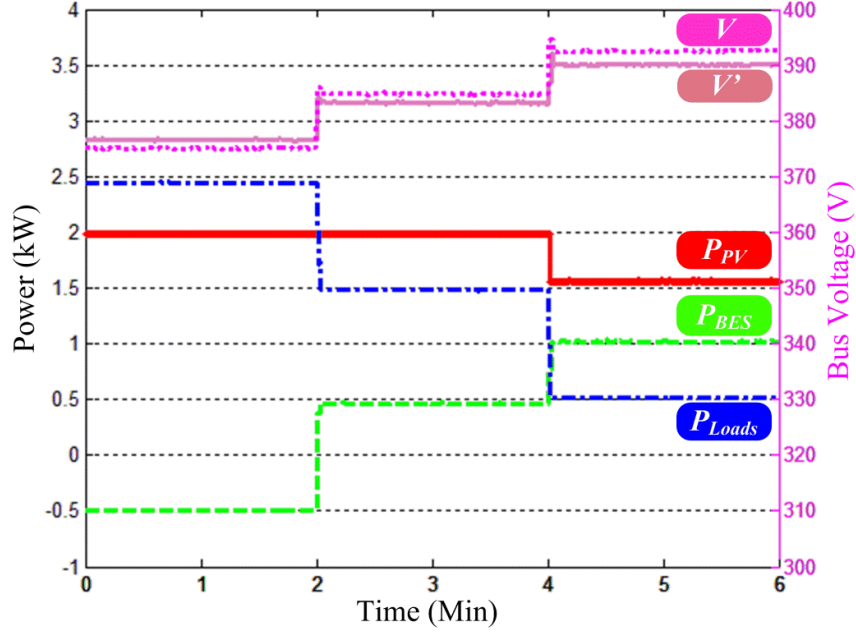
Fig. 2.28 Case 1 experimental results.

At 4 min and system load were further decreased to 0.5 kW. BES charging power increased instantly till reaching the maximum charging power capacity. Therefore BES converter changed from VRM to PCM operation with charging power reference of 1 kW to avoid over-current charge. At this moment, system bus voltage was not regulated actively and thus has exceeded the threshold value V_{H1} due to system power excess. Therefore, PV converter mode operation changed to VRM. The output power of PV was reduced to be 1.5 kW to rebalance system power. The longer duration of transition can be observed than that at 2 min due to the response time need for battery and PV converter to change operating mode. System was finally stabilized at 392.5 V and the voltage increment was 7.5 V.

In contrast, with power-capacity-based bus voltage region partition implementation, the threshold voltages of V_{H1} and V_{L1} became 386.7 V and 373.3 V, respectively, according to equations (2-28) and (2-29). The updated threshold voltages resulted in uniform droop coefficients to be 6.67 V/kW for all regions. The experiment with

44

the same generation and loading profiles as previous case was conducted. The updated system bus voltage implementing power capacity based partition is represented with curve *V'*.

The configuration of system units mode operations and output power in different loading conditions were stayed the same as that with the conventional partition method. Initially, system bus voltage was regulated by the BES converter in discharging stage at 376.7 V. At 2 min, system load consumption was reduced to 1.5 kW, BES changed to charging stage and stabilized at 383.3 V. The bus voltage increment with 1 kW load reduction was 6.7 V which is smaller compared to the conventional partition. At 4 min, system loads were further reduced to 0.5 kW and system bus voltage was increased to 390 V. The voltage increments during both transitions due to load variations were the same since the same droop coefficients were applied.

Case 2

This case verified the effect of online droop coefficient tuning when system unit power capacity variation occurred. The power capacity of PV was decreased to 1.5 kW. To compare the effect with and without online droop coefficient tuning, the droop coefficients and threshold voltages were kept the same as that in Case 1 with the conventional partition. The experimental results are displayed in Fig. 2.29. Initially, resistive load bank was turned on with power consumption of 0.75 kW. System bus voltage was regulated at 385 V by BES with 0.75 kW of charging power.

Linear reduction of system load consumption from 0.75 to 0.45 kW was triggered at 3 min to showcase system response during operating mode transition from H1 to H2. BES charging power increased accordingly with the decrease of load consumption. When BES charging reached the maximum charging power, BES changed from VRM to PCM with reference power of 1 kW. Meanwhile, system bus voltage was increasing gradually until 386.7 V which was the threshold voltage for the activation of PV operation mode change. Due to bus voltage discontinuity, a

45

3.3 V bus voltage jump was observed as can be seen in Fig. 2.29. Voltage surge was also observed momentarily same as in Case 1 during the operating region transition due to PV converter response delay. System was regulated at 390.3 V with PV output power of 1.45 kW.
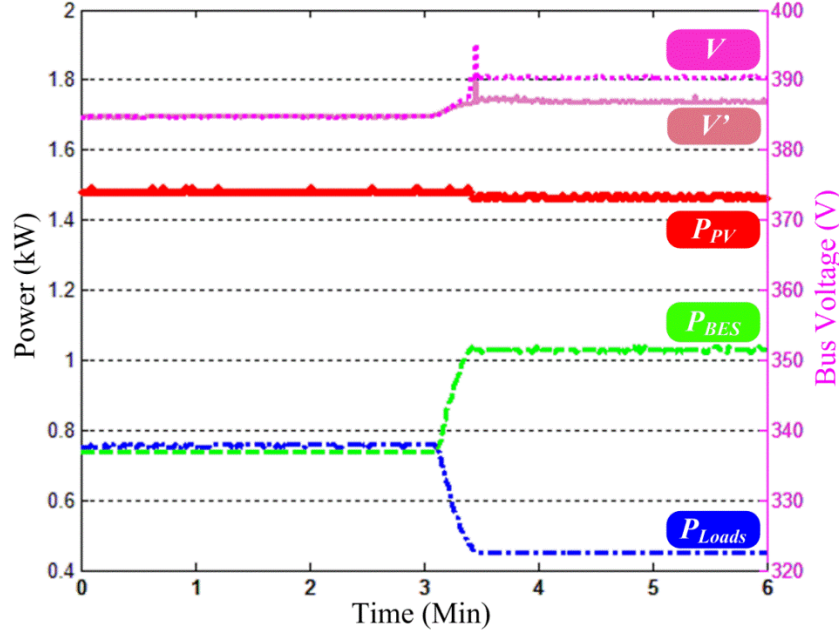
Fig. 2.29 Case 2 experimental results.

In comparison, based on estimation of the real-time PV power capacity as explained in Section 2.4.3, the droop coefficient of PV in H2 was tuned to be 8.89 V/kW. As PV converter changed to VRM, the reference bus voltage was 387. The discontinuity of bus voltage change during the transition can be eliminated. Therefore, seamless voltage region transition was fulfilled.

2.6   Conclusion

Multiple modes distributed EMS based on local bus voltage measurement has been implemented to ensure system power balance in DC microgrid. The independency from communication link makes this method more reliable compared to centralized EMS. In multiple modes distributed EMS, system bus voltage is partitioned into several regions and system units are prioritized based on their marginal utilization costs. The system units' mode operations are scheduled by the comparison between

the local bus voltage and the threshold voltages.

Verification of the effectiveness of the multiple modes distributed EMS has been performed in a lab-scale DC microgrid. Experimental operating mode change of system units have been conducted according to localized bus voltage variations and different loading conditions. In each bus voltage region, system bus voltage was able to be regulated steadily.

However, there are also some disadvantages of multiple modes distributed EMS, such as:

a   System bus voltage variations causing lower power quality occur in different voltage regions.

b   Significant bus voltage fluctuations exist during the voltage region transitions due to operating mode change of system units.

c   Active power sharing scheme is not be able to be applied in case multiple slack terminals are operating in parallel.

Therefore, to improve the performance of multiple modes distributed EMS, multiple-slack-terminal with online droop coefficient tuning distributed EMS is proposed. Droop control is an effective solution for distributed EMS operation. Implementing droop control in distributed EMS ensures continuous system bus voltage during regions transitions. In addition, active power sharing among the multiple slack terminals can be realized effectively.

To reduce excessive bus voltage variation due to load change and power sharing error due to transmission line impedance, power-capacity-based bus voltage region partition that ensures equalized droop coefficients in different bus voltage regions is adopted. Furthermore, online droop coefficient tuning based on the estimation of system units' power capacities in real time is also implemented to eliminate the bus voltage discontinuity. Same as previous distributed EMS, the effectiveness of multiple-slack-terminal with online droop coefficient tuning distributed EMS has also been verified in a lab-scale DC microgrid.

Although a lot of enhancements that has been provided by multiple-slack-terminal

with online droop coefficient tuning distributed EMS, there are drawbacks that are not able to be eliminated by implementing distributed EMS including:

a   Deviation of bus voltage in steady.

b   Error of power sharing due to transmission impedance.

c   Inability of conducting systematic optimization, *e.g.* minimization of system operation cost, is difficult to realize.

Chapter III

Multi-Level EMS Based DC Microgrids

Implementation of distributed EMS has been proven to be able to ensure the system power balance and stability. However, distributed EMS has some challenges that are impossible to be solved including system bus deviations, power sharing error and systematic optimization. Therefore, multi-level EMS is proposed to reduce or even eliminate the challenges while improving the overall system reliability.

3.1 Multiple-Slack-Terminal Multi-Level EMS of DC Microgrids

Centralized EMS is usually implemented for the operation of DC microgrid with integration of various RESs, BESs, fossil fuel based NRES and BIC as can be seen in Fig. 1.1 [26, 45, 78-80]. Centralized EMS is effectively capable of realizing the systematic optimization with control objectives not limited to minimization of bus voltage variation, minimization of operation cost, equalization of BESs stored energy, *etc*. [19, 78, 81, 82]. Supervisory control and data acquisition (SCADA) system is required for centralized EMS based DC microgrid to acquire system operation statuses, including RESs generation, load consumption, system power flow, ESs SoC, *etc*., through the communication link. Communication link plays an important role in centralized EMS. Through communication link operating commands generated based on system control objectives in the central controller are assigned to respective system units. Therefore, any failure in communication link causes chaos in system operation. Besides that, reassignment of slack terminal is also needed when the active slack terminal experiences outage which will cause system bus voltage fluctuation.

However, the effects of slack terminal outage and communication link failure can be minimized by implementing advanced multiple-slack-terminal distributed EMS as elaborated in Section 2.4 [64, 83, 84]. DBS is considered as the global

information carrier used to configure the mode operation of system units so that the system operation is free from the communication link [51, 85]. System bus voltage range is partitioned into several regions to configure mode operations of system units. The power sharing among slack terminals are accomplished through *V-P* droop relationships [28].

Theoretically, power shared by a slack terminal is proportional to the reciprocal of the imposed droop coefficient. However, in actual implementation, difference in the bus voltages at slack terminal local controllers exists because of the transmission line impedance which causes deviation in system bus voltage and error in power tracking among slack terminals [50, 61]. Besides, the bus voltage deviation that is exacerbated because of droop control implementation can degrade the voltage sensitive loads lifetime [86, 87].

To remove deviation in bus voltage and error in power sharing, several works that applied secondary control has been proposed [50, 60, 65, 88]. The droop *V-P* relationships of slack terminals are modified to control system bus voltage and slack terminal power flow. However, with the power shared among them is proportionate to the installed power capacities, which result in ineffective cost solution [65, 88]. The power references of slack terminals should be assigned according to the real-time system operation cost to achieve a cost-effective solution. Multi-level EMS is thus proposed to solve the afore-mentioned problems and enhance system control accuracy while retaining the reliability.
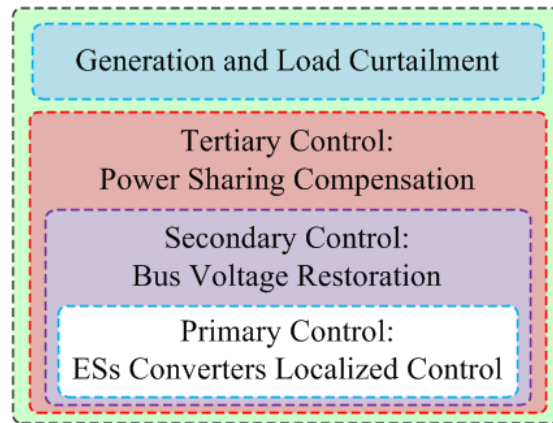
Fig. 3.1 Multi-level EMS control block diagram.

3.1.1   Multi-Level EMS

Multi-level EMS control block diagram is displayed in Fig. 3.1. The multi-level EMS strategy is divided into three level of control, *i.e.* primary, secondary and tertiary control. Generation and load curtailment are applied for the protection of DC microgrids. The details explanation of each level is provided as follows:

<u>Primary control</u>

In primary control, multiple-slack-terminal distributed EMS of DC microgrid described in Section 2.4 is employed with several system units are operated in VRM. Droop relationships for active power sharing among them and to prevent circulating current are applied in primary control. Fig. 3.2 displayed the control schematic diagram of primary control.
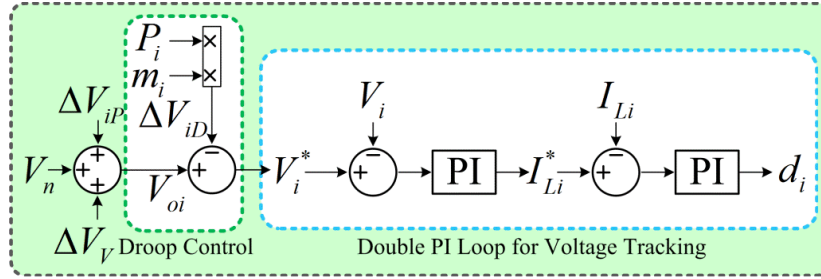
Fig. 3.2 Control schematic diagram of primary control.

It can be observed in Fig. 3.2 that to produce the droop voltage compensator ΔV_{iD} in droop control block, the ith slack terminal output power P_i is multiplied with the droop coefficient m_i. The reference output voltage of the ith slack terminal V_i^* is obtained from the difference between the threshold voltage V_{oi} and droop voltage compensator. Double-loop PI control is then occupied to track the reference output voltage by generating the duty ratio d_i for converter power switches [55].

In multiple-slack-terminal distributed EMS, slack terminals schedule their output powers and regulate bus voltage autonomously without the need of communication link. In contrast with centralized EMS, distributed EMS which is implemented in primary control has advantages as follows:

a   Better scalability of additional slack terminals.

b   Higher system controllability since no slack terminal reassignment is needed.

c   Higher capacity in voltage regulation due to the combined power capacity of slack terminals.

d   Faster system response speed as communication link is not needed.

<u>Secondary control</u>

Because of transmission line impedance and applied droop relationships, bus voltage deviation from the nominal bus voltage exists in steady state for multiple-slack-terminal distributed EMS [65]. The system bus voltage V and system net power P_{net} relationship in steady state is represented as:

$$V = V_n - m_{eq}P_{net} \qquad (3\text{-}1)$$

where m_{eq} is the combined droop coefficient of slack terminals.
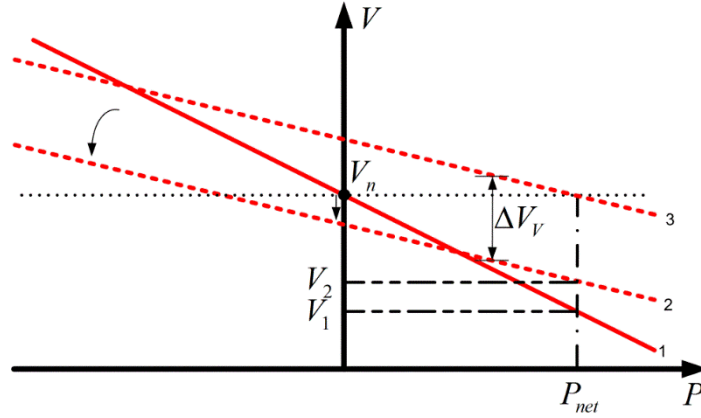
Fig. 3.3 Effect of bus voltage restoration to system characteristic.

The effect of bus voltage restoration to system characteristic curve is as can be seen in Fig. 3.3. The curve 1 represents the theoretical V-P characteristic. For the given P_{net}, the theoretical bus voltage is V_1. However, the existence of transmission line impedance causes the droop coefficient change and threshold voltage deviation are induced. The bus voltage and system net power relationship as in (3-1) changes to:

$$V = (V_n + \delta V) - (m_{eq} + \delta m)P_{net} \qquad (3\text{-}2)$$

52

where δV is the change in threshold voltage and δm is the change in droop coefficient [50]. The actual system characteristic curve becomes the dashed curve 2 due to δV and δm. For the same given system net power P_{net}, the updated bus voltage is changed to V_2.

System bus voltage deviation can degrade system power quality and affect the system units operation lifetime.
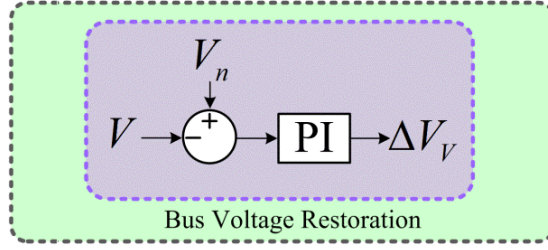
Fig. 3.4 Control schematic diagram of secondary control.

Bus voltage restoration is proposed in secondary control as displayed in Fig. 3.4 to remove the system bus voltage deviation systematically [50, 61, 66]. The system bus voltage V is compared with the nominal value V_n and the result is then handled by PI control to produce the voltage compensator ΔV_V [88]:

$$\Delta V_V = G_{BVR}(V - V_n) \tag{3-3}$$

where G_{BVR} is the PI control gain in bus voltage restoration block.

In DC microgrids, no single point bus voltage measurement can be selected to specify the system bus voltage. Therefore, to specify system bus voltage, the average value of the measured sensitive loads voltages is applied.

$$\overline{V} = \frac{1}{M}\sum V_{Si} \tag{3-4}$$

where V_{Si} is the voltage measurement at the ith sensitive load; M is total number of voltage measurements; and $\overline{V}$ is the average voltage.

The voltage compensator ΔV_V generated in the central controller, updates the threshold voltages of all slack terminals through the communication link.

53

$$V_{oi} = V_{oi} + \Delta V_V \qquad (3\text{-}5)$$

Bus voltage restoration causes the threshold voltage of system *V-P* characteristic to be increased by ΔV_V. It is the same as shifting the *V-P* characteristic curve vertically from the dashed curve 2 to the dashed curve 3 in Fig. 3.3. With bus voltage restoration the system bus voltage can thus be regulated at the nominal value V_n. Therefore, the voltage deviation is eliminated and the system power quality is enhanced.

The updating frequency of the primary control is equivalent to the switching frequency of converters to accurately track respective reference output voltage. In secondary control, the updating frequency of the bus voltage compensation constrained by the communication link is slower than that of the primary control.

Tertiary control

Power sharing compensation is implemented in tertiary control displayed in Fig 3.5 to eliminate the error in power tracking [65]. The power reference of slack terminal is obtained through economic dispatch which will be explained later in Section 3.1.2. The main goal of applying economic dispatch is to minimize system operation cost of DC microgrids.
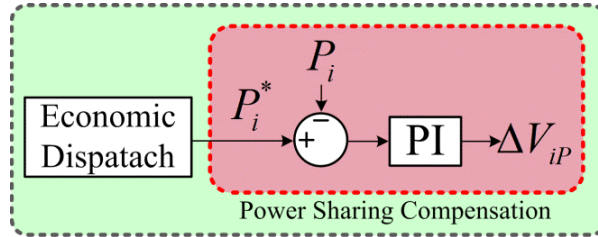
Fig. 3.5 Control schematic diagram of tertiary control.

As seen in Fig. 3.5, the ith slack terminal reference power P_i^* is compared with the ith slack terminal real-time output power P_i to generate the power tracking error. The variation is handled by a PI control to produce the power sharing voltage compensator ΔV_{iP} [65].

$$\Delta V_{iP} = G_{PSCi}(P_i - P_i^*) \qquad (3\text{-}6)$$

where G_{PSCi} is the PI control gain in power sharing compensation for the ith slack terminal.

The power sharing voltage compensator ΔV_{iP} generated in the central controller, is applied to adjust the threshold voltage of respective slack terminals. With the addition of power sharing compensation, the threshold voltage of the ith slack terminal as in (3-5) is modified to be:

$$V_{oi} = V_n + \Delta V_V + \Delta V_{iP} \tag{3-7}$$

Although it operates in VRM, power sharing compensation enables slack terminal to follow the power reference. Likewise the secondary control, the updating frequency of the power sharing voltage compensation is slower than of the primary control.

Generation and load curtailment

Generation and load curtailment are implemented for the protection of DC microgrid by limiting the range of system net power [89]. For example for an islanded DC microgrid integrated with BESs and PVs, when BESs charging power reaches the maximum value, generation curtailment by constraining solar PV generation will be activated to avoid bus voltage overshoot caused by the excess of system power [45]. Likewise when BESs discharging power reaches the maximum value, load curtailment by disconnected uncritical load will be activated to avoid significant bus voltage sag because of system power deficiency [90]. Another constraint for the decision of generation and load curtailment activation is BESs stored energy range. Generation and load curtailment will be activated when BESs upper and lower of Depth of Discharge (DoD) threshold values are reached, respectively [85].

Multi-level EMS consisted of primary, secondary and tertiary control with system protection ensures system power balance and system control accuracy. In steady state, deviation in system bus voltage and error in power tracking can be removed effectively. Secondary and tertiary controls require communication link to be operated, hence in case of communication failure they are not functioning.

55

However, system operation is still be able to be ensured by primary control but with the degraded control accuracy.

3.1.2 Economic Dispatch

Economic dispatch which determines the reference output power of each system units is proposed to minimize system operation cost including the cost of BESs, RESs, NRESs and utility grid.

$$CT = \sum C_{BESi} + \sum C_{RESj} + C_{NRES} + C_U \qquad (3\text{-}8)$$

where CT is the system overall operation cost; C_{BESi} is the cost of BESi; C_{RESj} is the cost of RESj; C_{NRES} is the cost of NRES; and C_U is the cost of utility grid. Constraints of the system operation are:

$$P_{Loads} = P_{BESs} + P_{RESs} + P_{NRES} + P_U \qquad (3\text{-}9)$$

$$P_{BESi}^{\min} < P_{BESi} \le P_{BESi}^{\max} \qquad (3\text{-}10)$$

$$DoD_i^{\min} < DoD_i \le DoD_i^{\max} \qquad (3\text{-}11)$$

$$0 < P_{NRES} \le P_{NRES}^{\max} \qquad (3\text{-}12)$$

$$0 < P_{RESj} \le P_{RESj}^{\max} \qquad (3\text{-}13)$$

$$P_U^{\min} < P_U \le P_U^{\max} \qquad (3\text{-}14)$$

where $DoD_i^{\min}$ is BESi minimum depth of discharge; $DoD_i^{\max}$ is BESi are maximum depth of discharge; $P_{NRES}^{\max}$ is the NRES maximum output power; $P_{RESj}^{\max}$ is the RESj maximum power generation; $P_U^{\min}$ is the utility grid minimum output power; and $P_U^{\max}$ is the utility grid maximum output power. The $P_U^{\min}$ and $P_U^{\max}$ are limited by the bidirectional interlinking converter.

In DC microgrids operation, cost of system units can be classified into fixed and variable costs. In this thesis, only variable cost which refers to the cost changes with cumulated output energy which comprises battery lifetime degradation cost, fuel cost, utility electricity cost, *etc.*, is considered for system operation [57].

Comparison of system units' marginal cost is proposed to minimize system operation cost instead of implementing complicated optimization algorithm. Marginal cost ($/kWh), which is the incremental costs incurred for additional electricity generation of 1 kWh, is formulized for quantitative comparison. The marginal cost of solar PV (MC_{PV}) is assumed to be zero as the energy source from solar is free. The marginal cost of NRES (MC_{NRES}) is mainly depended on the fossil fuel price which can be assumed to be fixed. The marginal cost of utility grid (MC_U) is equal to the electricity price when the DC microgrid is importing energy from the utility grid. When the DC microgrid is exporting energy to the utility grid, government incentive, which is indicated with a negative MC_U value, applies. The obtainment of BES marginal cost (MC_{BES}) which is more complicated is elaborated as the following [91].

Marginal cost of BES

Cost of BES depends on BES life. BES life Γ_R measured as the total of ampere-hour effective discharge is assumed to be finite and can be formulized as [92, 93]:

$$\Gamma_R = C_R D_R L_R \tag{3-15}$$

where C_R is the capacity at discharge current I_R; D_R is the DoD at which the rated cycle life is determined; L_R is the cycle life at D_R and I_R.

Battery cycle life which influences battery lifetime is altered in value according to the actual DoD and the discharging rate [94]. The relationship between battery cycle life with actual DoD D_A, is expressed as:

$$L = L_R \left(\frac{D_R}{D_A} \right)^{u_0} e^{u_1 \left(1 - \frac{D_A}{D_R} \right)} \tag{3-16}$$

Coefficient u_0 and u_1 in (3-16) are obtained from the curve fitting of the cycle life versus DoD data provided in the battery datasheet. The effective discharge which is also affected by discharging rate can be expressed as:

$$d_{eff} = \left(\frac{D_A}{D_R}\right)^{u_0} e^{u_1\left(\frac{D_A}{D_R}-1\right)} \frac{C_R}{C_A} d_A \qquad (3\text{-}17)$$

where d_{eff} is the effective discharge; d_A is the actual discharge; and C_A is the capacity at actual discharging current obtained from the amperes vs. discharge table provided in battery specification sheets [93].

The actual discharge of BESi is

$$d_{Ai} = \frac{P_{BESi}}{V_{BESi}} \Delta t \qquad (3\text{-}18)$$

where P_{BESi}, V_{BESi} and Δt are discharging power, terminal voltage of BESi and operating period time-step, respectively. BES power output is assumed to be fixed during Δt. The cost of BESi is

$$C_{BESi} = \frac{RC_i}{\Gamma_R} d_{eff\_i} \qquad (3\text{-}19)$$

where RC_i is the BESi replacement cost and d_{eff_i} is the effective discharge of BESi. Substituting (3-17) and (3-18) to (3-19) results in:

$$C_{BESi} = \frac{RC_i}{\Gamma_R} \left(\frac{D_{Ai}}{D_R}\right)^{u_0} e^{u_1\left(\frac{D_{Ai}}{D_R}-1\right)} \frac{C_R}{C_{Ai}} \frac{P_{BESi}}{V_{BESi}} \Delta t \qquad (3\text{-}20)$$

where D_{Ai} is BESi actual depth of discharge and C_{Ai} is the actual capacity based on the actual discharging current.

Therefore, dividing C_{BESi} with the cumulated energy output generates marginal cost of BESi which is formulated as.

$$MC_{BESi} = \left(\frac{D_{Ai}}{D_R}\right)^{u_0} e^{u_1\left(\frac{D_{Ai}}{D_R}-1\right)} \frac{K}{C_{Ai}} \qquad (3\text{-}21)$$

where K is a constant value, described as:

$$K = \frac{RC_i C_R}{\Gamma_R V_{BESi}} \qquad (3\text{-}22)$$

58

As indicated in (3-21) and (3-22), the marginal cost of BESi depends on the DoD and discharging rate. The C_{Ai} is inversely related to BES power output P_{BESi} [95]. Equations (3-21) and (3-22) show the marginal cost of BESi in discharging stage. Since the duration of the period is limited, BES DoD is assumed to be fixed within an iteration cycle.
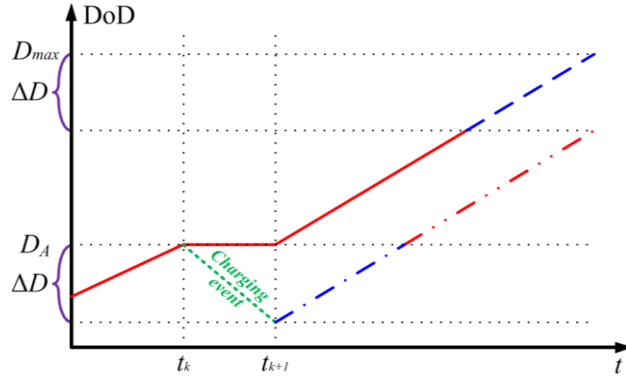
Fig. 3.6 Effect of charging stage to BES DoD.

The decreasing of DoD for all discharging event that occurs afterwards is the effect of BES charging event as displayed in Fig. 3.6. The DoD of D_A at t_k without encountered charging event will have the same DoD at t_{k+1} which is represented by solid curve.

Whereas the DoD of D_A at t_k will decrease by ΔD at t_{k+1} which is represented by dash-dot curve because the charging event that was encountered. The effect of having charging event is equivalent to replace the discharging event at DoD value of D_{max} with D_A, which can be seen in the Fig. 3.6. Therefore, difference in effective discharge for future discharging event is:

$$\Delta d_{eff} = \left(\left(\frac{D_A}{D_R} \right)^{u_0} e^{u_1 \left(\frac{D_A}{D_R} - 1 \right)} - \left(\frac{D_{max}}{D_R} \right)^{u_0} e^{u_1 \left(\frac{D_{max}}{D_R} - 1 \right)} \right) \frac{P_{BESi}}{V_{BESi}} \Delta t \qquad (3\text{-}23)$$

Replacing the D_{max} with D_R results in

$$\Delta d_{eff} = \left(\left(\frac{D_A}{D_R} \right)^{u_0} e^{u_1 \left(\frac{D_A}{D_R} - 1 \right)} - 1 \right) \frac{P_{BESi}}{V_{BESi}} \Delta t \qquad (3\text{-}24)$$

Therefore, the marginal cost of BESi in charging state, which is a negative value can be shown as:

$$MC_{BESi} = \frac{\Delta d_{eff}}{\Gamma_R} RC_i = \frac{RC_i}{\Gamma_R V_{Bi}(t)} \left(\left(\frac{D_{Ai}}{D_R} \right)^{u_0} e^{u_1 \left(\frac{D_{Ai}}{D_R} - 1 \right)} - 1 \right) \tag{3-25}$$

For each period, the marginal cost of BESi in charging stage, which is determined by D_{Ai}, is assumed to be constant since the change of actual DoD can be negligible. The marginal cost of BESi in charging and discharging stage can thus be obtained.

Comparison of marginal costs
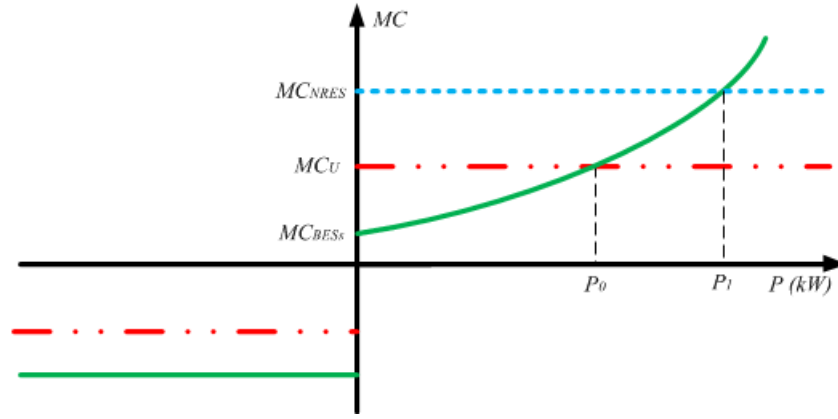
Fig. 3.7 Marginal costs of system units.

The economic dispatch is conducted by comparing the marginal costs of NRES, utility grid and BESi as displayed in Fig. 3.7. The blue dashed curve, red double-dot-dashed curve and green solid curves indicate the marginal costs of NRES, utility grid and BESs, respectively. In this case, marginal cost of NRES is assumed to be fixed and determined by the fuel price. NRES can only generate power with positive output power. The marginal cost of utility grid is positive when importing power and determined by the real-time electricity price. When DC microgrid is exporting power to the utility grid, the marginal cost MC_U is indicated with the government incentives, whose magnitude is negative and usually lower than that of electricity price. Since marginal cost of localized NRES generation is normally higher than the electricity price, the utilization priority of NRES is assigned to be the lowest. The marginal cost of BESs in discharging stage is affected by the real-

60

time DoD and the output power. In charging stage the marginal cost of BESs is constant and determined by actual DoD at the time the charging stage is occurred.

The power dispatch prioritization of system units is determined according the respective marginal cost. Lower marginal cost system unit has higher dispatch priority. Since the marginal cost of RESs is the lowest, RESs are scheduled with the highest dispatch priority. The curve MC_{BESs} intersects with the MC_{Ut} and MC_{NRES} at output power of P_0 and P_1, respectively. With system net power P_{net} is presented as:

$$P_{net} = P_{Loads} - P_{RESs} = P_{BESs} + P_{NRES} + P_U \qquad (3\text{-}26)$$

The power scheduling of NRES, utility grid and BESs based on the real-time economic dispatch is thus:

$$P_{BESs} = \begin{cases} P_{net} & (P_{net} \leq P_o) \\ P_o & (P_o < P_{net} \leq P_o + P_{BIC}^{\max}) \\ P_{net} - P_{BIC}^{\max} & (P_o + P_{BIC}^{\max} < P_{net}) \end{cases} \qquad (3\text{-}27)$$

BESs power reference is limited by the maximum discharging and charging power: $[P_{BESs}^{\min}, P_{BESs}^{\max}]$.

$$P_U = \begin{cases} P_{net} - P_{BESs}^{\min} & (P_{net} \leq P_{BESs}^{\min}) \\ P_{net} - P_o & (P_o < P_{net}) \end{cases} \qquad (3\text{-}28)$$

Output power of utility grid is limited by: $[P_U^{\min}, P_U^{\max}]$.

$$P_{NRES} = \begin{cases} 0 & (P_{net} \leq P_1 + P_U^{\max}) \\ P_{net} - P_1 - P_U^{\max} & (P_1 + P_U^{\max} < P_{net}) \end{cases} \qquad (3\text{-}29)$$

The NRES output power is constrained by $P_{NRES}^{\max}$. The economic dispatch in tertiary control is realized with the generated power references as described in (3-27) – (3-29).

The advantage of the proposed economic dispatch by comparing the marginal costs of system units is the method simplicity instead of implementing complicated

optimization for system operation cost. The comparison of marginal cost is carried out to determine the utilization priority of system units.

3.2 Seamless Transition Between Islanded and Grid-Tied Modes of DC Microgrids

To enhance system reliability, the operation of DC microgrids can be in either grid-tied or islanded mode. For grid-tied DC microgrids, both the utility grid and localized BESs can be regarded as the energy compensator to retain system power balance [26, 96-98]. DC microgrid operates in islanded mode when utility grid fault occurs to isolate it from the disturbance. Therefore, only BESs that play important role to retain system power balance [16, 24].

3.2.1 Transitions Between Grid-Tied and Islanded modes

A generic DC microgrid with integration of various system units comprising RESs, BESs and loads is displayed in Fig. 3.8.
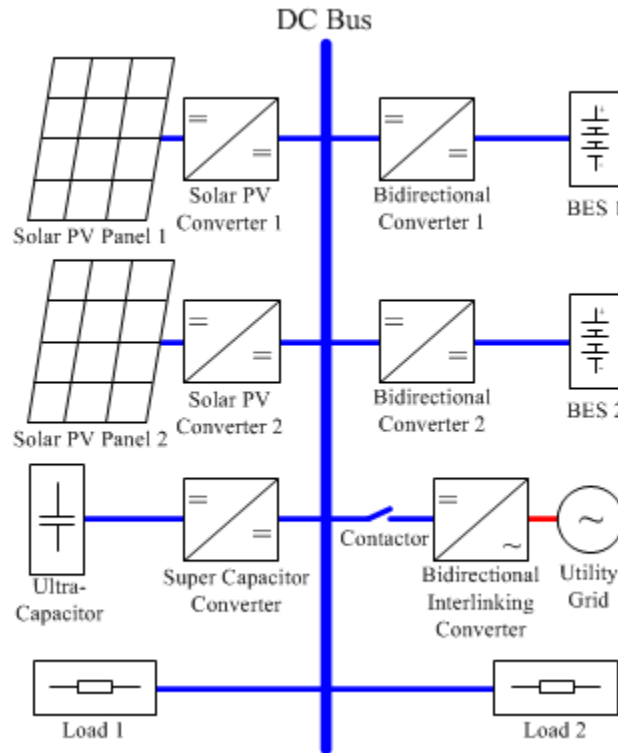
Fig. 3.8 A DC microgrid schematic diagram.

Two elements that are crucial for grid-tied mode operation of DC microgrid are bidirectional DC-AC converter and contactor.
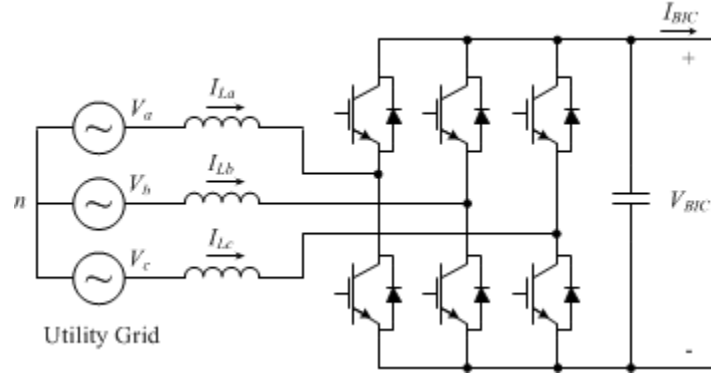
Fig. 3.9 Schematic diagram of BIC.

A bidirectional DC-AC converter is installed as a bidirectional interlinking converter (BIC) to control the power flow between the utility grid and the DC bus [99, 100]. The BIC schematic and control diagrams are presented in Fig. 3.9 and Fig. 3.10, respectively.
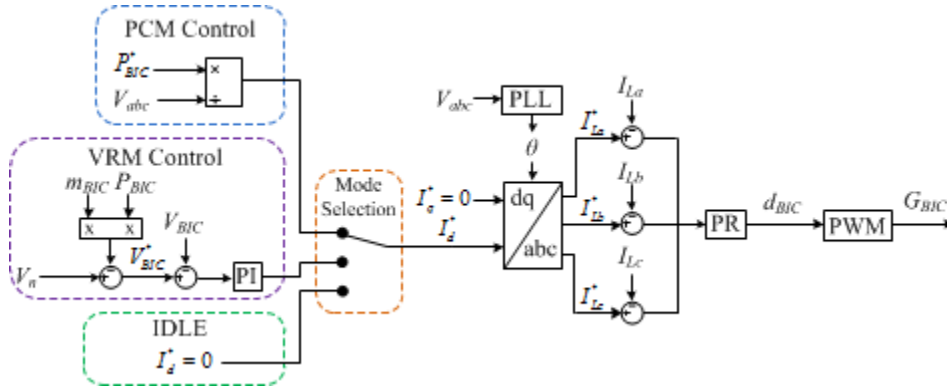
Fig. 3.10 Control diagram of BIC.

BIC can operate in two directions, when BIC injects power from DC microgrid to utility grid, BIC operates in inversion stage. In reverse, BIC operates in rectification stage when power flow is from utility grid to DC microgrid. Three modes can be configured for BIC, i.e. PCM, VRM and IDLE mode. When BIC operates in PCM, the reference inductor current in direct axis is generated with the reference power P_{BIC}^* and AC side bus voltage V_{abc}. When BIC operates in VRM, the reference output voltage V_{BIC}^* is generated by comparing the nominal bus

63

voltage with voltage compensator obtained in droop control. When BIC operates in IDLE mode, the reference inductor current is set to be zero. Conventional PR controller as described in Section 2.2.3 is applied to track the inductor current and produce switching signals G_{BIC}.

A contactor is established between DC microgrid and BIC for autonomous islanding and reconnection. The operating modes of the remaining system units are same as explained in Section 2.1.

Conventionally, when the DC microgrid is in grid-tied mode, BIC operates in VRM [27, 47, 64, 101]. Whereas, localized BESs operate in PCM whose power references are assigned according to control objectives, like ESs SoC equalization, system cost minimization, bus voltage variation minimization, *etc*. [45, 49, 96].

Upon detection of the utility grid fault, the contactor will be opened causing the DC microgrid operates in islanded mode and BIC changes the operation mode to IDLE in order to isolate the utility disturbance [24]. A BES, normally the one with the highest power capacity and ramp rate, has to change the mode operation to VRM to regulate the DC bus voltage [28, 41, 85]. However, system response delay is resulted due to operation reference assignment and data acquisition process. At this short duration, no slack terminal exists to regulate system bus voltage during transition. Therefore, system bus voltage variation could be induced.

Activation of BES operating mode change, from VRM to PCM or vice versa, based on the comparison between the local bus voltage and predefined threshold voltage in distributed EMS has been introduced [27, 28, 55]. Nevertheless, the threshold voltage for BES operation mode change always has certain deviation from the nominal bus voltage V_n because of the imposed droop control [41, 71]. As a result, during the transition significant system bus voltage variation will also be induced.

DC microgrid reconnection to the utility grid will be activated once utility grid fault has been dissolved. BIC operation mode from IDLE returns to VRM and BES from VRM returns to PCM [24]. BIC regulates AC output voltage when reconnected to utility grid. The procedure of reconnection is alike to that of the

conventional AC microgrid [102, 103]. Utility grid voltage, frequency and phase angle are synchronized with phase-locked loop (PLL) to generate the voltage reference for BIC AC output [104]. At the last step of the reconnection, when BIC AC output voltage has matched with the utility grid voltage, the contactor will be closed.

Operating modes of BIC and BESs in both grid-tied and islanded modes have been presented in many research works [24, 83, 105]. However, the detailed procedure during the transition has seldom been discussed in detail. The sequence of operating mode change during the transition between grid-tied and islanded mode is crucial. For example in reconnection process, if BES is changed first to PCM, active system bus voltage regulation does not exist during the transition, which might result in bus voltage variations. Conversely, if BIC changes first to VRM, coexistence of multiple slack terminals may cause uncontrollable circulating current [83]. In summary, the disadvantages of conventional method include:

a System bus voltage variation because of BIC and BESs mode operation changes.

b No active bus voltage regulation during transition.

c Uncontrollable circulating current in case of multiple slack terminals connected in parallel.

3.2.2 Multiple-Slack-Terminal DC Microgrid Operating Modes Transition

To cope with the aforementioned disadvantages of conventional method, advanced multiple-slack-terminal distributed EMS discussed in Section 2.4 is implemented. In case additional slack terminals are connected, implementation of droop control enables the capability of the system to limit the circulating current, which makes it suitable for DC microgrid reconnection. Both BIC and BESs operate in DC voltage regulation. Detailed transition procedures for both islanding and utility grid reconnection are explained as follows.

Islanding

Upon detection of fault in utility grid, the DC microgrid alters from grid-tied to

islanded mode. At this situation, BIC changes to operate in IDLE mode immediately by halting all power electronic switches. The contactor displayed in Fig. 3.8 is opened.

In this EMS strategy, BES mode operation remains the same at all time so that system bus voltage is actively regulated throughout the transition. The bus voltage in steady state is represented as:

$$V_{bus} = V_n - P_{net} \bigg/ \sum \frac{1}{m_{BESi}} \tag{3-30}$$

where P_{net} and m_{BESi} are the system net power and the droop coefficient of BESi, respectively. The BESi shared power is:

$$P_{BESi} = \frac{P_{BESi}^{max}}{P_{BESs}^{max}} P_{net} \tag{3-31}$$

Reconnection

Reconnection is performed when utility grid back to operate in normal condition. Instead of matching the conventional AC side bus voltage for synchronization, matching BIC DC side output voltage which is more feasible alternative is proposed. Fig. 3.11 displays the proposed reconnection procedure flowchart. First, the power quality of utility grid is monitored at BIC local controller. As the utility grid has been back to normal condition, the "cleared" signal is transmitted to the central controller.

When the utility disturbance has been cleared, BIC changes the operation mode from IDLE to VRM to regulate DC side output voltage. The reference bus voltage of BIC is generated based on droop control with the threshold voltage of V_n. As the contactor is still open, BIC DC output capacitor voltage is maintained at the nominal value with zero output power.

Because of the limited magnitude of line impedance, voltage variation across the contactor can cause significant inrush current when the contactor is closed which might cause malfunction and unintentional protection schemes activation of

66

converters [106]. Thus, before the contactor is closed, the difference between system bus voltage and BIC DC output voltage has to be minimized to reduce the inrush current. System bus voltage V_{bus} is compared with BIC output capacitor voltage V_{BIC}. BIC output voltage is considered matched with system bus voltage when the voltage variation is lesser than the predefined threshold value δV.
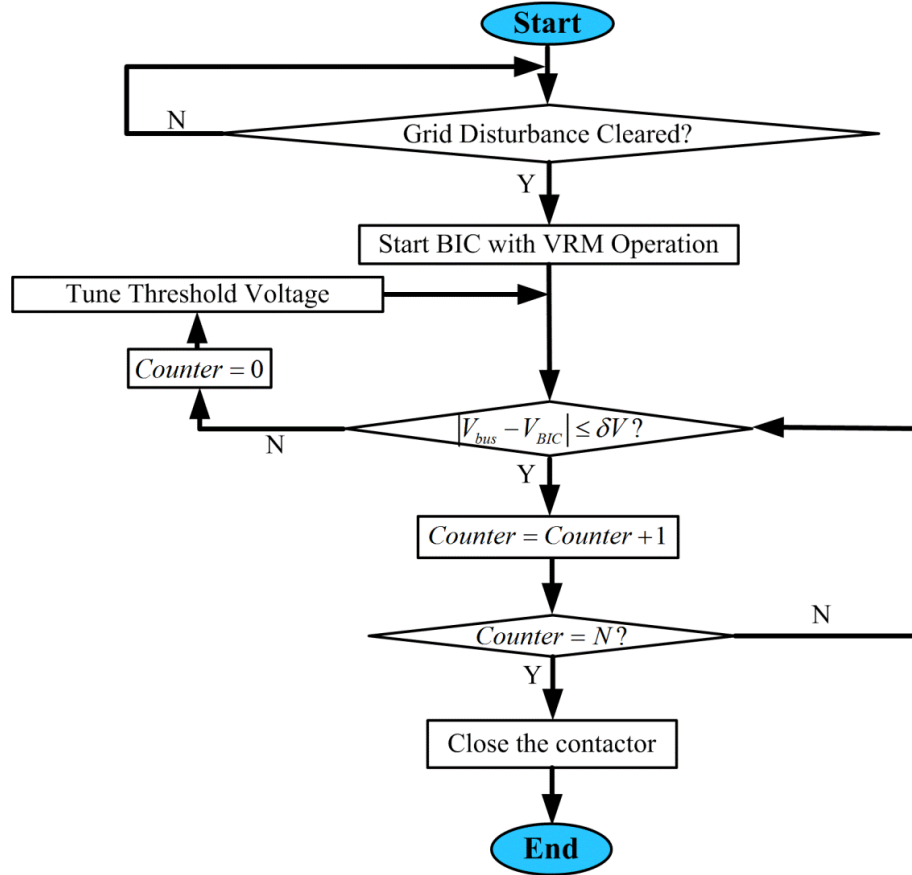
Fig. 3.11 Grid reconnection flowchart.

A counter is applied to guarantee that the voltages at both sides of the contactor have been stabilized. The counter is activated once the voltage variation is lesser than δV. Otherwise, it indicates that the significant bus voltage variation is still existed. The counter is thus reset to zero and the DC voltage checking should be restarted. The contactor is then closed to interlink the DC microgrid bus with the BIC, only if the voltage variation has been within the allowable range for N times continuously.

3.2.3 Multi-level EMS

Since deviation in system bus voltage and error in power tracking are existed in the multiple-slack-terminal distributed EMS, Multi-level EMS [61, 107] as presented in Section 3.1 is thus implemented. Conventionally, all slack terminals are normally scheduled with the equal utilization priority and the reference powers are generated in proportion to the power capacities [50, 65]. In this proposed method, BIC and BESs power references are produced according to their utilization priority, battery SoC and real-time system net power.

Bus voltage restoration in secondary control follows that as described in Section 3.1.1. To remove the voltage deviation, the threshold voltages of ESs and BIC are adjusted with the voltage compensator in real time.

Both localized BESs and the utility grid are assigned to diminish system power imbalance caused by the RESs generation intermittency and load consumption uncertainty. Because of the reliability factor, localized BESs utilization priority is higher compared to utility grid electricity [64, 108]. The BESs reference power P_{BESs}^{*} and the BIC reference power P_{BIC}^{*} are:

$$
P_{BESs}^{*} = \begin{cases} P_{BESs}^{\min} & (P_{net} \leq P_{BESs}^{\min}) \\ P_{net} & (P_{BESs}^{\min} < P_{net} \leq P_{BESs}^{\max}) \\ P_{BESs}^{\max} & (P_{BESs}^{\max} < P_{net}) \end{cases} \tag{3-32}
$$

$$
P_{BIC}^{*} = \begin{cases} P_{net} - P_{BESs}^{\min} & (P_{net} \leq P_{BESs}^{\min}) \\ 0 & (P_{BESs}^{\min} < P_{net} \leq P_{BESs}^{\max}) \\ P_{net} - P_{BESs}^{\max} & (P_{BESs}^{\max} < P_{net}) \end{cases} \tag{3-33}
$$

where $P_{BESs}^{\min}$ is the minimum output power of the combined localized BESs and $P_{BESs}^{\max}$ is the maximum output power of the combined localized BESs.

Another constraint for BESs power dispatch is the state of charge (SoC) [26, 45, 86]. Threshold values, SoC_{max} and SoC_{min}, are determined to constrain the variation of battery stored energy. When battery SoC reaches SoC_{max}, BESs charging power capacity is zero. The P_{BESs}^{*} and P_{BIC}^{*} are thus:

68

$$P_{BESs}^* = \begin{cases} 0 & (P_{net} \leq 0) \\ P_{net} & (0 < P_{net} \leq P_{BESs}^{\max}) \\ P_{BESs}^{\max} & (P_{BESs}^{\max} < P_{net}) \end{cases} \quad \text{(3-34)}$$

$$P_{BIC}^* = \begin{cases} P_{net} & (P_{net} \leq 0) \\ 0 & (0 < P_{net} \leq P_{BESs}^{\max}) \\ P_{net} - P_{BESs}^{\max} & (P_{BESs}^{\max} < P_{net}) \end{cases} \quad \text{(3-35)}$$

Likewise, when SoC reaches SoC_{min}, BESs discharging power capacity is zero. The P_{BESs}^* and P_{BIC}^* are thus:

$$P_{BESs}^* = \begin{cases} P_{BESs}^{\min} & (P_{net} \leq P_{BESs}^{\min}) \\ P_{net} & (P_{BESs}^{\min} < P_{net} \leq 0) \\ 0 & (0 < P_{net}) \end{cases} \quad \text{(3-36)}$$

$$P_{BIC}^* = \begin{cases} P_{net} - P_{BESs}^{\min} & (P_{net} \leq P_{BESs}^{\min}) \\ 0 & (P_{BESs}^{\min} < P_{net} \leq 0) \\ P_{net} & (0 < P_{net}) \end{cases} \quad \text{(3-37)}$$

Power sharing compensation is also implemented in multi-level EMS to eliminate the power tracking error.

3.3 Experimental Verifications

To validate the effectiveness of the proposed EMS, experimental verifications have been conducted. The schematic layout of the lab-scale DC microgrid consisted of BESs, solar PVs, NRESs and various loads, is as displayed in Fig. 3.12.
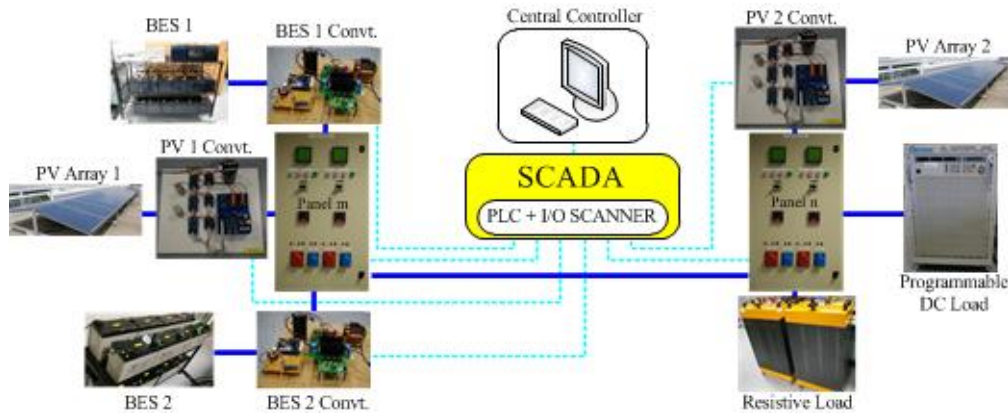
Fig. 3.12 Schematic diagram of a lab-scale DC microgrid.

Supervisory control and data acquisition (SCADA) system with the standard Modbus TCP/IP communication is integrated in central controller with the 1 Hz of updating frequency. The SCADA system consists of programmable logic controller (PLC) as the controller and I/O scanner to facilitate the data acquisition and command transmission. Every circuit panel is considered as a remote terminal unit (RTU) with a unique IP address. Every power electronic converter is embedded with communication module and also with a unique IP address. All of them communicate with central controller to ensure the stability of DC microgrid operation.

3.3.1 Multi-Level EMS of Multiple Slack Terminals DC Microgrids

The voltage compensators are updated every 1 second same with the updating frequency of SCADA system. The allowable system bus voltage range was ± 10 V. The respective BES1 and BES2 droop coefficients assigned according to (2-10) are 10 V/kW and 5 V/kW. The experimental specifications of BESs for case studies as followed are as represented in Table 3.1.

Table 3.1 BESs experimental specifications.

Parameters	BES1	BES2
Initial DoD	0.8	0.5
Droop coefficient (V/kW)	10	5
Terminal Voltage (V)	120	240
Power capacity (kW)	1	2
L_R	2055	2055
D_R	1	1
C_R (Ah)	137	137
u_0	1.67	1.67
u_1	-0.52	-0.52
Replacement cost ($)	18088.4	36172.8

Case 1

The operation of primary control, distributed EMS, was verified in Case 1. The operation modes of system units were as stated in Table 3.2. The reference voltages of BES1 and BES2 were determined according to the droop control. NRES is only activated once its local bus voltage has achieved the lower voltage boundary *i.e.* 370 V. Fig. 3.13 showcases the experimental results of this case.

Table 3.2 Operation mode of each system unit.

System Units	Operation Mode
BES1	VRM
BES2	VRM
PV	MPPT mode
NRES	IDLE mode

Initially, resistive load power consumption around 0.5 kW was switched on. The output power of solar PVs was 1.6 kW. For the given generation and load profile, system bus voltage was regulated at 384.4 V. The deviation from the nominal voltage *i.e*. 380 V was 4.4 V. Theoretically BES1 and BES2 shared power proportionally according to their power capacities. However, power tracking error exists because of transmission line impedance. The comparison of the theoretical with the actual output power of BES1 *ΔP* has been illustrated in Fig. 3.13.

At 5 min, the programmable load with load consumption of 1 kW was switched on, BESs charging power thus reduced immediately to keep system power balance. Because of the response delay of the BESs converters during the transition, bus voltage sag of 2 V was induced. At steady state, system bus voltage was regulated at 379.2 V.

At 10 min, the programmable load was further increased to 2 kW, and caused BESs to function in discharging stage. Therefore, system bus voltage was decreased to 374 V subsequently with 6 V voltage deviation.

At 15 min, the programmable load was decreased back to 1 kW and caused BESs to function in charging stage. At this loading profile, the bus voltage was stabilized at 379.6 V. Because of response delay of the BESs converters during the transition, bus voltage surge with magnitude of 2 V can be observed.

At 20 min, system bus voltage was further increased to 384 V when programmable load was disconnected. Since significant PV generation fluctuations occurred during 20-25 min, BESs charging power and system bus voltage have followed the fluctuations accordingly.
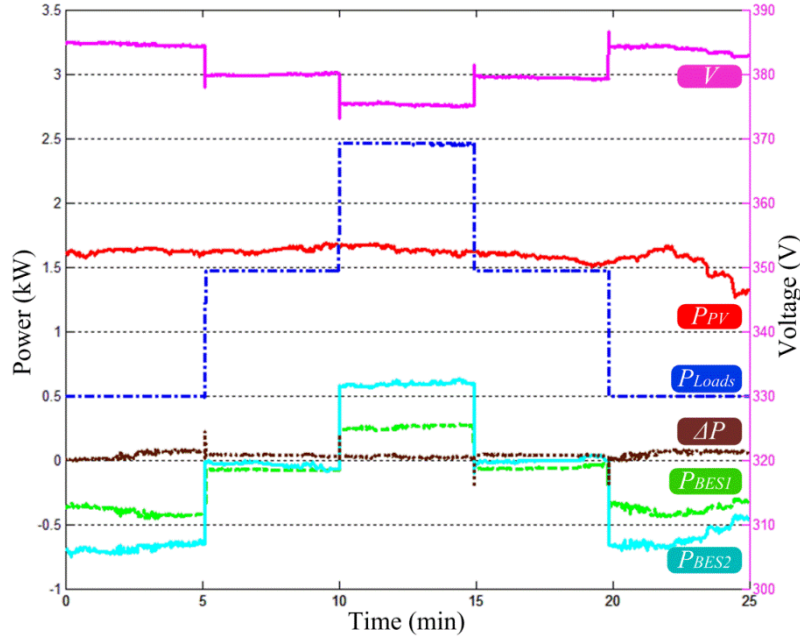
Fig. 3.13 Case 1 experimental results.

The primary control which is distributed EMS can schedule the operation of all system units autonomously irrespective of the system net power variations. However, steady state bus voltage deviation can still be observed. Besides, because of transmission line impedance, BESs power tracking errors has been induced.

Case 2

Multi-level EMS with implementation of bus voltage restoration and power sharing compensation was carried out in this case for comparison. The voltage compensator generated in (3-3) tuned the threshold voltages of BESs to the nominal value. Concurrently, the voltage compensators for power sharing compensation were generated to eliminate BESs power tracking errors. BESs threshold voltages are thus tuned using (3-7) accordingly. The loading profile was stayed the same as in the previous case. The experimental results are as can be seen in Fig. 3.14.

Initially, with system load consumption of 0.5 kW both BES1 and BES2 operated in charging stage. With secondary control, system bus voltage deviation can be eliminated in steady state. Likewise, BESs power tracking error of ΔP was kept at zero with power sharing compensation as displayed in Fig. 3.14.

72

At 5 min, 1 kW of load power was added to system load consumption, BESs discharged power to rebalance system power. Due to instant power decrease, system bus voltage sag of 6.4 V was detected. The resulted bus voltage variation was sent to the voltage restoration block to be processed through PI control to produce voltage compensator. The generated voltage compensator later tuned the BESs threshold voltages. The duration of the transition was 0.4 min before the bus voltage was restored to the nominal value because the voltage step change was limited to 0.1 V every 1 s. BESs power sharing error was also able to be eliminated as specified from curve ΔP.
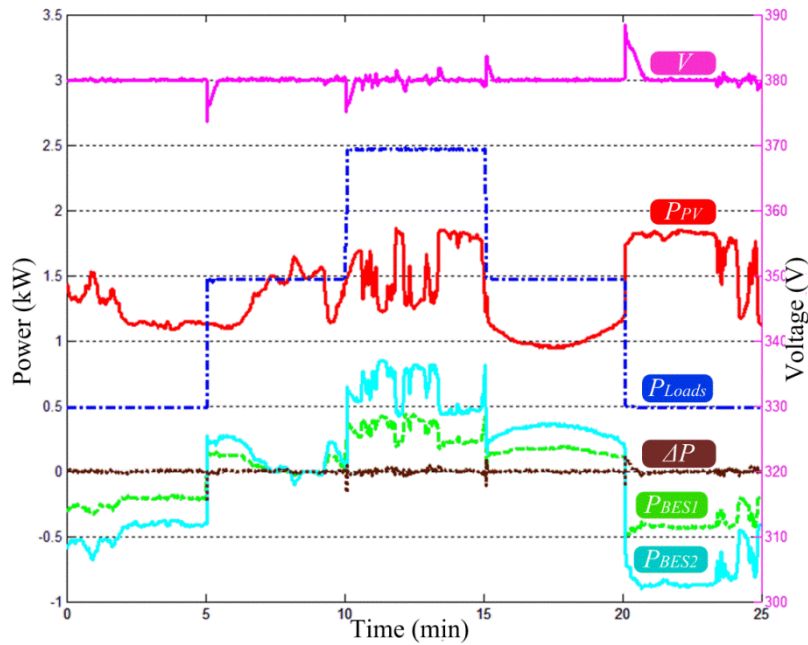
Fig. 3.14 Case 2 experimental results.

For all transitions at 10 min, 15 min and 20 min, the proposed method can eliminate both steady state bus voltage deviation and power sharing error. Because significant fluctuations of solar irradiation have happened between 10 min to 15 min, high frequency variations of BESs output power fluctuations were occurred. The proposed multi-level EMS realized both system bus voltage regulation and power sharing accurately in steady state.

Case 3

In this case, economic dispatch based on comparison of system units' marginal

costs as discussed in Section 3.1.2 was demonstrated. Utilization prioritization is based on system unit's marginal cost to minimize system operation cost. With the proposed economic dispatch, system units power references are thus generated according to (3-27) – (3-29).

Fig. 3.15 shows the experimental results. Initially, with load consumption system net power of 0.25 kW was resulted. To maintain system power balance, BESs thus operated in discharging stage. Bus voltage was regulated at nominal bus voltage with bus voltage restoration in secondary control. At this time, since NRES' marginal cost was much higher than that of BESs hence NRES operated in IDLE mode. The marginal costs at discharging of BES1 and BES2 were calculated based on (3-21) – (3-22). The initial DoD of BES2 was lower than of BES1 hence the cost curve of BES2 located under curve of BES1. BES1 power reference was thus assigned to be zero and BES2 compensated the power deficiency.
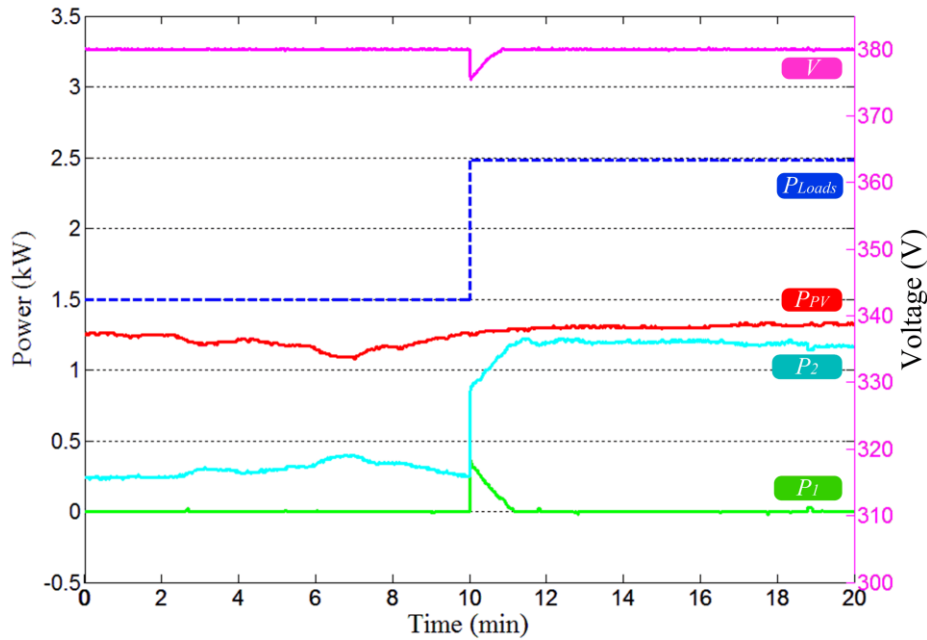
Fig. 3.15 Case 3 experimental results.

At 10 min, system load consumption became 2.5 kW, both BES1 and BES2 output power has increased instantaneously to rebalance system power. During transition, bus voltage sag of 4.1 V was observed because of the imposed droop relationship. When bus voltage deviation was detected, BESs threshold voltages were adjusted

with ΔV_V. It needed 0.7 min for the system to restore bus voltage to the nominal value. Since the cost curve of BES 2 was still beneath BES1, the generated BES1 power reference remained the same. The total operation cost incorporated for this case study was 5.214 cents. In contrast, if the conventional proportional BESs power sharing was implemented, the incorporated system operation cost will be 6.736 cents, which is 29.1% more compared to the proposed economic dispatch.

Case 1 demonstrated that system bus voltage regulation and power sharing were realized effectively with primary control only. However, since primary control implemented droop control, steady state deviation in bus voltage and error in power tracking exist. In comparison, Case 2 showcased multi-level EMS that eliminated the problem arisen in Case 1 by implementing bus voltage restoration and power sharing compensation. In Case 3, economic dispatch based on comparison of system units' marginal costs has been performed which resulted in significant reduction of the overall system operation cost compared to the conventional proportional sharing.

3.3.2 Seamless Transition Between Islanded and Grid-tied Mode of DC Microgrids

The schematic diagram of the lab-scale DC microgrid for experimental purpose is displayed in Fig. 3.16.
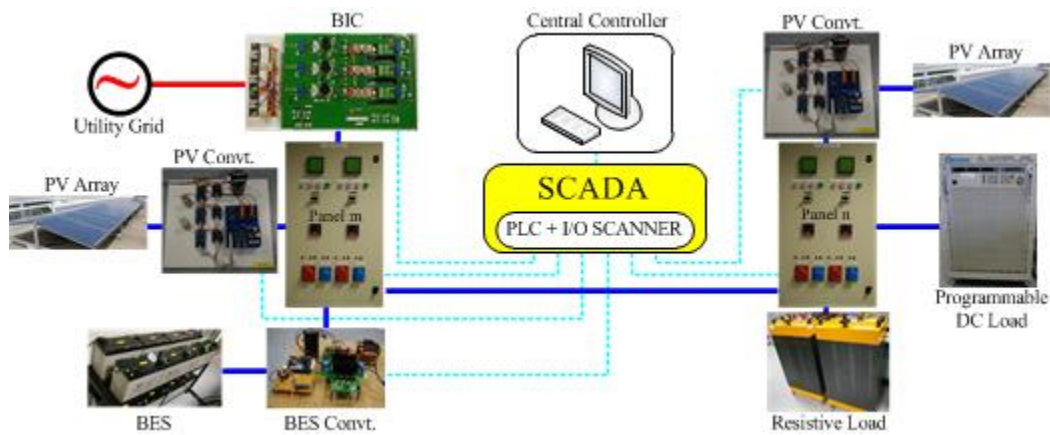
Fig. 3.16 Schematic diagram of the lab-scale DC microgrid.

The lead-acid battery bank is integrated as the localized BES. The DC bus is linked to the utility grid through a BIC. The contactor is installed inside the circuit panel. Specifications of experimental specifications are presented in Table 3.3. BES and BIC droop coefficients are determined with allowable bus voltage variation of ±10 V.

Table 3.3 Experimental specifications.

Parameters	Unit	Setting
PV1 power capacity	kW	1.3
PV2 power capacity	kW	1.4
BES power capacity	kW	2
BIC power capacity	kW	2
BES droop coefficient	V/kW	5
BIC droop coefficient	V/kW	5
Nominal bus voltage	V	380
System bus capacitance (grid-tied)	μF	5340

Case 1

Comparison for islanding processes between the conventional method and the proposed method was conducted in Case 1. Fig 3.17 showcased the experimental results, including BES output current, BIC output current and bus voltage, for the conventional method obtained with oscilloscope. In the beginning, BIC was in VRM at 380 V and BES was in PCM with output power of 0 kW. The 1 kW of system load was thus supplied by BIC. The bus voltage at BES output capacitor was 378.3 V.
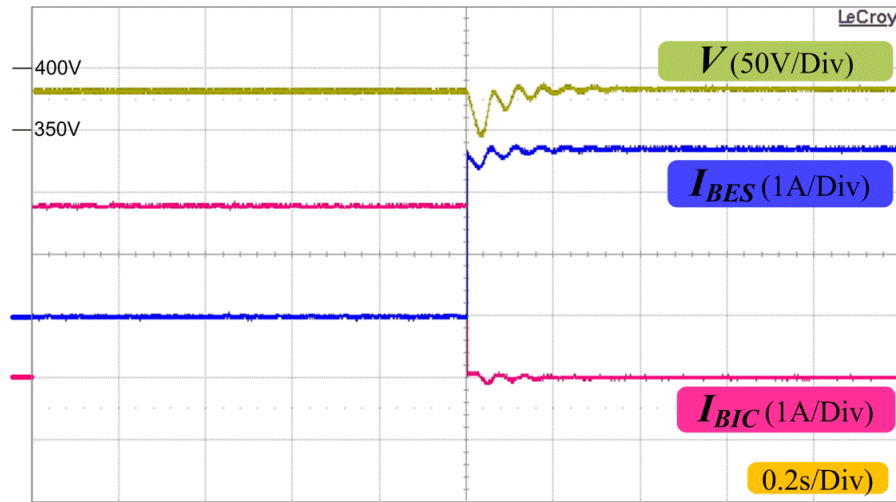
Fig. 3.17 Islanding system response with the conventional method.

76

When utility grid disturbance was detected, BIC changed to operate in IDLE mode with 0 A output current. At this time system bus voltage dropped can be observed because of system power deficiency. BES changes to operate in VRM by comparing with the threshold voltage, *i.e.* 365 V. The load consumption thus was compensated by BES. The voltage sag of 37 V occurred because of the response delay of BES. After transition the steady state bus voltage at BES output was 380 V.

In comparison, DC microgrid islanding with the proposed multiple-slack-terminal DC microgrid was employed. Initially, both BES and BIC were in VRM to eliminate BES operating mode change during islanding. The threshold voltage of BIC was increased gradually until BES output power was stabilized at 0 kW to compare the result more intuitively. BIC thus compensated load consumption as in the conventional method. The experimental results are displayed in Fig. 3.18.

As islanding of the DC microgrid is activated, BES operating mode remained the same and the output power has increased immediately to compensate the system power deficiency. Bus voltage sag during transition was mainly because of the response delay of BES and instant system power deficiency. The voltage sag was 18 V at the time of the transition, which was much smaller compared to that in the conventional method. In steady state, system bus voltage decrease of 5 V was induced because of the increase in output power.
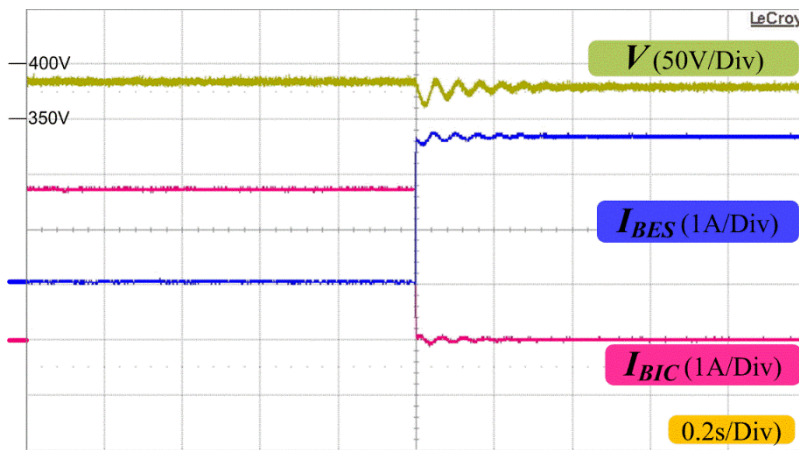
Fig. 3.18 Islanding system response with the proposed method.

This case demonstrated DC microgrid islanding with multi-level EMS. DC meter data acquired through the SCADA system was used to showcase system operation statuses. The experimental results are displayed in Fig. 3.19. The system bus voltage was determined from the average value of the bus voltages measured at the loads.
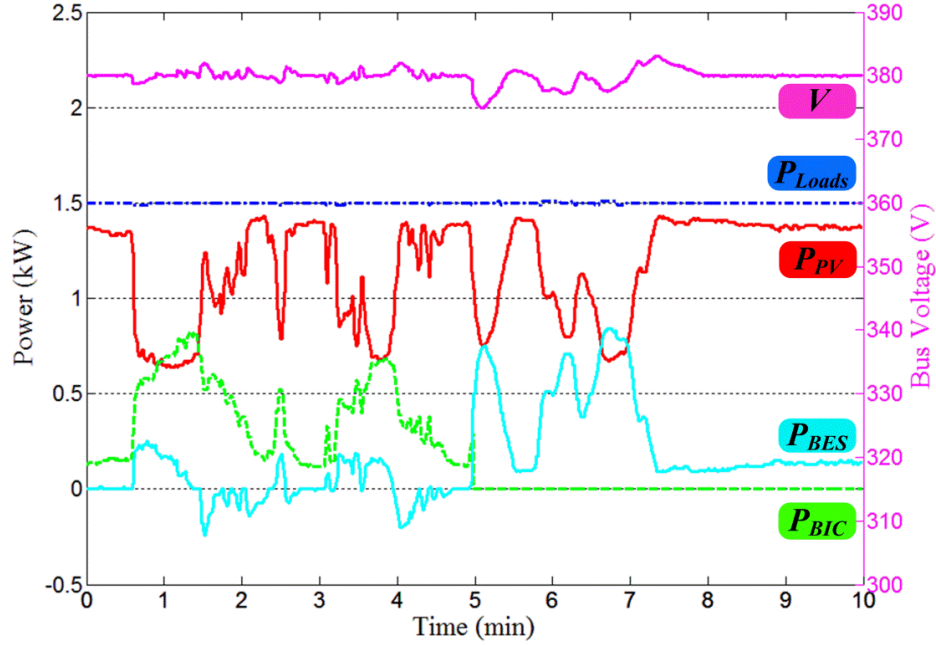
Fig. 3.19 Case 2 experimental results

During 0.5-7.3 min because of the real-time solar irradiation change, significant PV generation variation was observed. The load consumption was operated with constant load power of 1.5 kW. System bus voltage was sent to the central control as a feedback to produce the voltage compensator. Threshold voltages of BES and BIC were adjusted accordingly to regulate the bus voltage at nominal value. Since BES initial SoC was set at the minimum value SoC_{min}, hence BES discharging power capacity was zero. As the system net power was 0.14 kW, the respective power references of BES and BIC were 0 and 0.14 kW.

Significant output power change of BES and BIC have been observed because of the fluctuations of PV generation from 0.5 min onwards. Because of the droop relationships imposed and system power changes, system bus voltage variations

78

have occurred accordingly. However in steady state, with the implementation of multi-level EMS, system bus voltage was regulated to the nominal value and BES output power has followed the reference value of 0 kW.

As utility grid disturbance was detected at 5 min, BIC operation of IDLE mode was activated with zero output power. The DC microgrid has thus changed to operate in islanded mode. BES turned out to be the only slack terminal for mitigation of system net power. BES output power has increased instantaneously to regulate system bus voltage and maintain system power balance.

During the transition, because the PV generation reduction of 0.65 kW has happened simultaneously, system power deficiency has been enlarged. Therefore, bus voltage sag of 5.1 V was induced. As bus voltage deviation was detected, bus voltage restoration adjusted BES threshold voltage to the nominal value. Afterwards, BES output power has followed the variation of PV generation accordingly. At 7.6 min, system was stabilized and system bus voltage was maintained at the nominal value.

With multi-level EMS, system bus voltage deviations were removed in steady state. Power sharing compensation was also implemented to actualize active power dispatch of BESs and BIC according to the utilization priority settings, battery SoC and the real-time system net power. Therefore, system control accuracy was enhanced with multi-level EMS both in grid-tied and islanded states.

Case 3

Comparison between the conventional and proposed methods of DC microgrid reconnection was realized in Case 3. The reconnection experimental result with the conventional method is displayed in Fig. 3.20. Initially, the DC microgrid was in islanded mode with BES was in VRM regulating system bus voltage at 380 V. After that, BIC switched to run in VRM where V_n serves as the reference voltage of once utility grid disturbance was cleared. At this time, the contactor remained open hence BIC output power was 0 kW. In order to reduce the difference voltage in

both of the contactor's sides, BIC DC side voltage was adjusted as represented in the flowchart of Fig. 3.11. The threshold voltage δV was set to be 1 V.
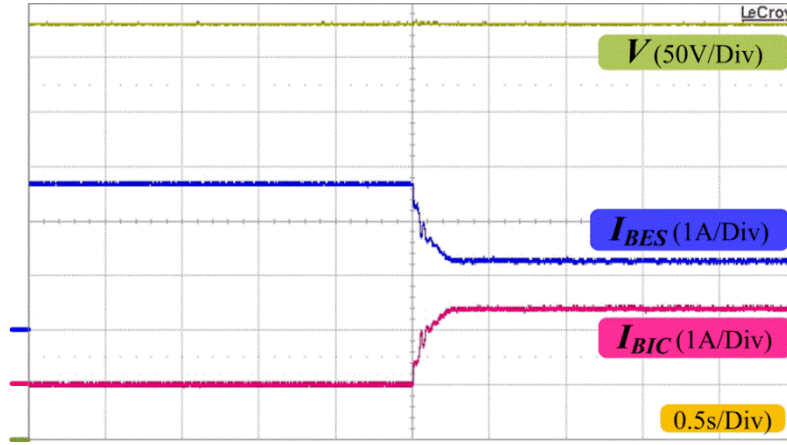
Fig. 3.20 Reconnection system response with the conventional method.

When bus voltages have been stabilized until 100 continuous iteration cycles at both sides of the contactor, the contactor was closed. Uncontrollable circulating current theoretically will be induced when there are more than one slack terminals arranged in parallel. However, practically the output power change of BES was constrained by the line impedance. BES output current reduction of 1.4 A was stabilized within 0.25 s after transition. Insignificant magnitude bus voltage swell with small amount of duration time was experienced at the time of the transition.
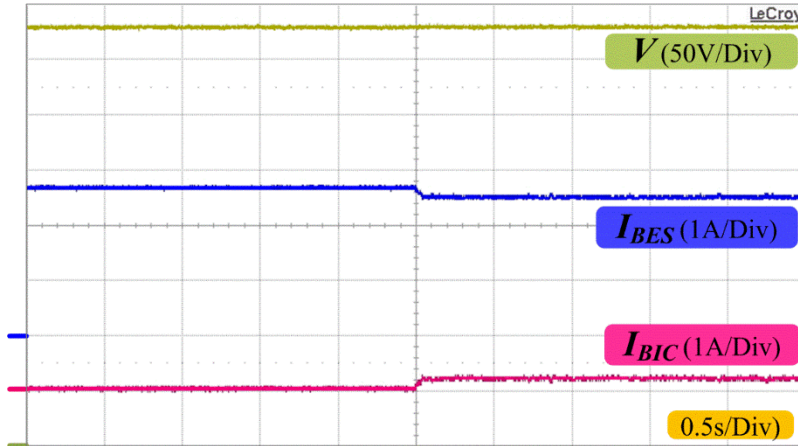
Fig. 3.21 Reconnection system response with the proposed method.

In contrast, reconnection was repeated with the proposed multiple-slack-terminal DC microgrid. Fig. 3.21 showcased the experimental results. The BES and BIC

80

operated in VRM with the implementation of droop control throughout the case study. Same like the previous, when the voltage variation was lower than the threshold value has been achieved for 100 continuous iteration cycles, the contactor was closed. After transition, BES output current was showing a lower reading by 0.2 A, this result was much lesser compared with the result obtained with conventional method. The time needed for the transition was also significantly decreased to 0.05 s. Throughout the whole transitions, the bus voltage of the system has stayed the same.

Seamless transition was ensured during the reconnection by implementing the procedure proposed as in Fig. 3.11. Bus voltage variations during the transition for both methods were insignificant. However, with the conventional method, abrupt change in the output current of BES has been induced when the contactor was closed due to the coexistence of more than one slack terminals in parallel. This issue was solved with the proposed multiple-slack-terminal which resulted in significant reduction of DC BES output power change due to the imposed droop relationships.

Case 4
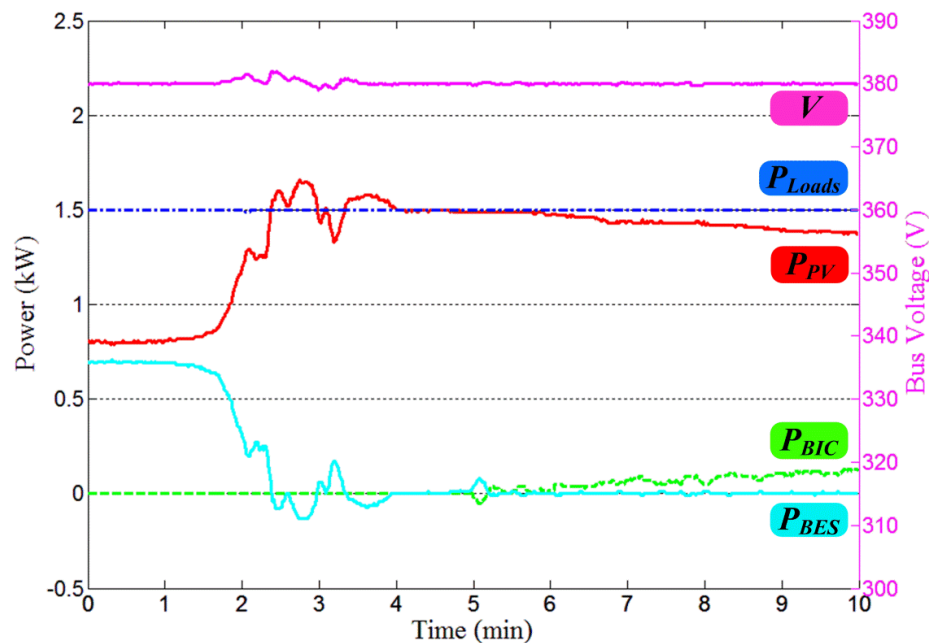
Fig. 3.22 Case 4 experimental results.

Case 4 verified the reconnection of DC microgrid using the proposed multi-level EMS as displayed in Fig. 3.22. Initially, the only slack terminal used for the system bus voltage regulation was the BES. The system net power was autonomously facilitated by BES. BES output power has followed the net power change closely when significant variations of solar generation happened during 2-4 min. The variation of the bus voltage occurred because of system power imbalance. However, in steady state, the implementation of bus voltage restoration is able to retrieve system bus voltage back to its nominal value.

When BIC has detected the clearance of utility grid disturbance, DC microgrid reconnection was activated which has followed the procedure as in Fig. 3.11. The contactor was closed when the bus voltages at two sides of the contactor have been matched for 100 continuous iteration cycles at 5 min. Grid-tied mode DC microgrid was thus in operation. Insignificant change that happened on the system bus voltage during the transition was observed. Because of the actual bus voltage variation between V_{BIC} and V_{bus}, BES instant power increase of 0.08 kW was induced. Since the net power of the system was positive and BES SoC was at the minimum value, BES was then set with lower utilization priority. Therefore, the compensation in power sharing was activated to track the BES reference power to be 0 kW in steady state.

3.4 Multi-Level EMS for Hybrid AC/DC Microgrids

The hybrid AC/DC microgrid, which is comprised of both AC and DC sub-grids, is proposed to enhance the system energy efficiency by minimizing the number of DC/AC/DC power conversions [100, 109]. In hybrid AC/DC microgrid, AC-compatible system units are connected to the AC sub-grid and DC-compatible system units are connected to the DC sub-grid. To realize bidirectional power flow between both sub-grids, the BIC is required. When AC sub-grid power surplus is detected, BIC power transfer from AC to DC sub-grid is activated to retain system power balance at both sides, and vice versa.

Distributed EMS of hybrid AC/DC microgrid has been suggested in [110] to cope the issue of communication link failure in centralized EMS [69]. System active power balances in the sub-grids of AC and DC are indicated with the AC frequency and DC bus voltage, respectively. Frequency/active power (f/P_{ac}) droop relationships are applied to AC power sources and bus voltage/output power (V/P_{dc}) droop relationships are applied to DC energy storages [105, 111]. To compare system power balance in AC and DC sub-grids intuitively, deviations of AC frequency and DC voltage are normalized by comparing the actual deviation with maximum allowable value. However, the existence of AC frequency and DC voltage deviations in steady state degrades power quality of the system and results in deterioration of system units' lifetime operation.

In this report, multi-level EMS of hybrid AC/DC microgrid is proposed to improve system control accuracy while retaining the communication fault ride-through capability. In primary control, distributed EMS is employed. AC frequency and DC bus voltage are considered as information carrier for AC and DC sub-grids, respectively, so that system units schedule their operations based on local information autonomously. BIC is occupied to equalize the normalized deviations of AC frequency and DC bus voltage. In secondary control, bus voltage restoration is implemented to enhance DC sub-grid power quality. In grid-tied mode AC frequency follows the frequency of utility grid. Whereas in islanded state, AC frequency restoration is implemented to restore the nominal frequency. In tertiary control, the marginal costs of all system units are compared and the one that has lesser marginal cost is assigned with higher utilization priority to dispatch power. Power sharing compensation is also implemented to eliminate the error in power tracking.

3.4.1 Distributed EMS of Hybrid AC/DC Microgrids

The schematic layout of the hybrid AC/DC microgrid is displayed in Fig. 3.23. DC system units including DC load, solar PV and BESs are connected to the DC sub-grid whereas AC system units including AC load, wind turbine, utility grid and diesel generator are connected to the AC sub-grid. Solar PV is integrated to the DC

sub-grid with a DC-DC converter and normally operates in MPPT. Bidirectional DC-DC converters are used to incorporate the BESs with the DC bus. Wind turbine is integrated to the AC bus with AC-AC power converter. The power transfer between the sub-grids of AC and DC is performed with the BIC. In this report only active power management is considered.
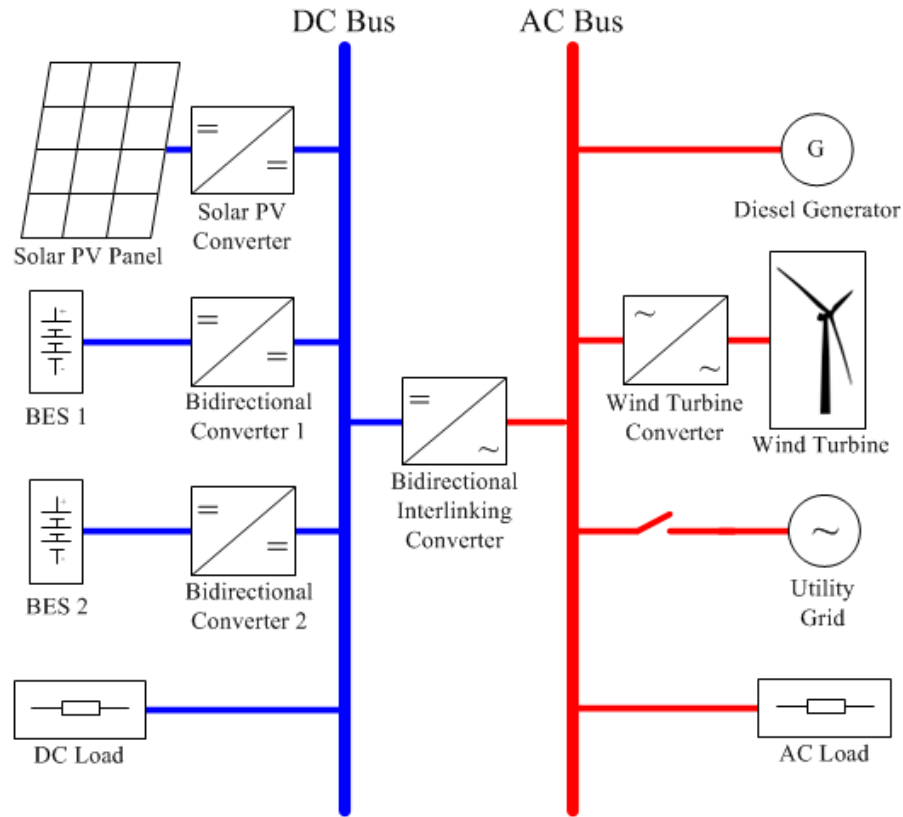
Fig. 3.23 Schematic layout of the hybrid AC/DC microgrid.

DC Sub-grid

The operation of distributed EMS on DC microgrid imposing droop relationship to all system units which has been elaborated in Section 2.4 is also implemented here.

AC Sub-grid

There two modes operation of AC sub-grid, *i.e.* grid-tied and islanded modes. In grid-tied state, AC voltage and frequency follow that of the utility grid. All system units connected to the AC bus operate as power terminals. When utility grid fault occurs, the relay connecting the utility grid and the AC sub-grid is opened to isolate the utility disturbance and the AC sub-grid thus operates in islanded mode.

84

In this islanded mode, AC bus voltage and frequency are regulated by local AC non-renewable distributed generations (NRDGs) which in this case are diesel generators (DGs). Wind turbine converter operates in MPPT mode. The f/P_{ac} droop relationship control is implemented for active power sharing among DGs.

$$f_i^* = f_{oi} - m_i P_{Gi} \tag{3-38}$$

where f_i^* is the reference frequency of DGi, f_{oi} is the threshold frequency of DGi, m_i is the droop coefficient of DGi and P_{Gi} is the output power of DGi.

The droop coefficient is:

$$m_i = \frac{\Delta f_{max}}{P_{Gi}^{max}} \tag{3-39}$$

where Δf_{max} is the maximum allowable frequency variation and P_{Gi}^{max} is the power capacity of DGi.

Power shared by DGi is:

$$P_{Gi} = \frac{P_{Gi}^{max}}{P_{Gs}^{max}} P_{net\_ac} = \frac{P_{Gi}^{max}}{P_{Gs}^{max}} (P_{L\_ac} - P_{WT}) \tag{3-40}$$

where P_{Gi}^{max}, P_{Gs}^{max} P_{net_ac}, P_{L_ac} and P_{WT} are the power capacity of DGi, combined power capacity of DGs, AC sub-grid net power, combined load consumption and wind turbine generation, respectively. The combined f/P_{ac} droop relationship becomes:

$$f = f_n - m_{eq} P_{net\_ac} \tag{3-41}$$

where m_{eq} is the equivalent droop coefficient of DGs.

BIC Control

System power balance in the sub-grids of AC and DC can be indicated from the AC frequency and DC bus voltage accordingly with droop control. The deviations of the AC frequency and DC bus voltage from their nominal values are proportional to the magnitude of net power in each sub-grid. To compare the power

85

balance in two sub-grids intuitively, the deviations are normalized by comparing the actual deviations with the maximum allowable variations as:

$$N_V = \frac{V - V_n}{\Delta V_{\max}} \qquad (3\text{-}42)$$

where N_V is the normalized DC bus voltage deviation.

$$N_f = \frac{f - f_n}{\Delta f_{\max}} \qquad (3\text{-}43)$$

where N_f is the normalized AC frequency deviation. The ranges of N_V and N_f are [-1, 1].
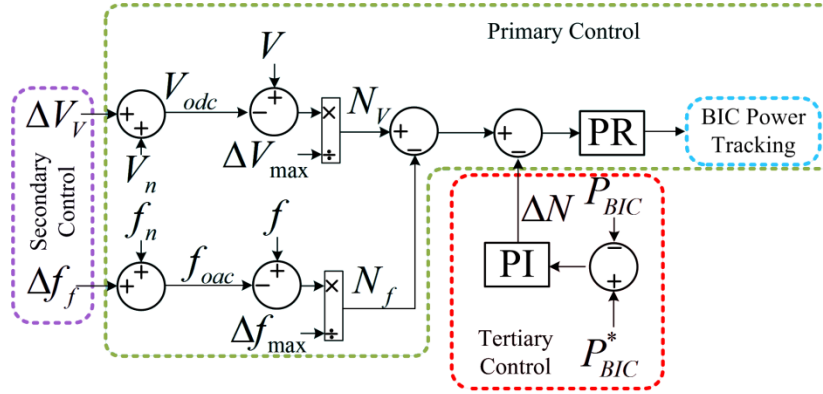
Fig. 3.24 Control diagram of BIC.

The control diagram of BIC is as displayed in Fig. 3.24. Actual values of DC bus voltage V and AC frequency f are compared with their threshold value V_{odc} and f_{odc}, respectively, and the deviations are then normalized in BIC local controller. The normalized voltage N_V and frequency N_f are compared and the difference are compared again with normalized compensator for power transfer. The difference is then treated with a PI control to produce BIC power reference [97, 110]. BIC inductor reference currents for three phases are thus obtained and tracked with Proportional-Resonant (PR) control in BIC power tracking block. With equalized normalized deviations, BESi and DGi shared powers are:

$$P_{BESi} = \frac{P_{BESi}^{\max}}{P_{BESs}^{\max} + P_{Gs}^{\max}}(P_{net\_dc} + P_{net\_ac}) \qquad (3\text{-}44)$$

86

$$P_{NRDGi} = \frac{P_{Gi}^{\max}}{P_{BESs}^{\max} + P_{Gs}^{\max}}(P_{net\_dc} + P_{net\_ac}) \qquad (3\text{-}45)$$

Therefore, the normalized deviation in steady state is:

$$N_V = N_f = \frac{P_{net\_dc} + P_{net\_ac}}{P_{BESs}^{\max} + P_{Gs}^{\max}} \qquad (3\text{-}46)$$

3.4.2 Multi-Level EMS of Hybrid AC/DC Microgrids

System power management within the sub-grids of AC and DC together with the power flow between them can be realized autonomously distributed EMS of hybrid AC/DC microgrid. However, AC frequency and DC bus voltage varies as an effect of the changes in real-time system net power. Moreover, the power sharing among BESs, utility grid and DGs is based on predefined priority setting, which is not suitable for system real-time operation. Therefore, multi-level EMS is proposed to improve the control accuracy while still retaining system reliability. In multi-level EMS, distributed EMS as discussed previously is applied as primary control.

Secondary Control

In secondary control, bus voltage restoration is implemented to remove the voltage deviation. The control diagram of BESi is displayed in Fig 3.2 and Fig 3.4. The operation of BESi in secondary control is the same with the one that has been explained in Section 3.11.
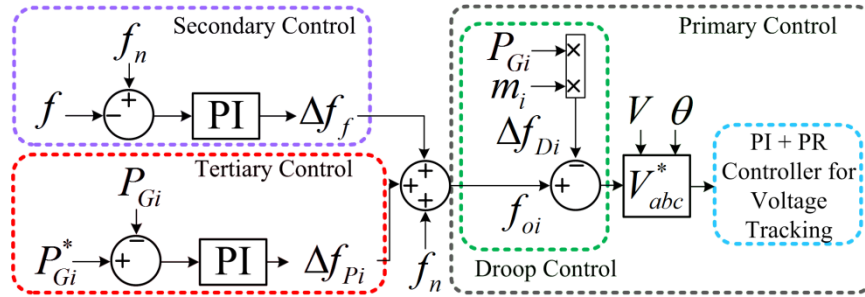
Fig. 3.25 Control diagram of DGi.

Similarly, frequency deviation exists in AC sub-grid due to the imposed f/P_{ac} droop relationship. Therefore, frequency restoration is implemented to enhance system power quality. Fig. 2.35 displays the control diagram of DGi. In primary control,

the reference frequency is generated with droop control in the local controller. Reference voltage can thus be generated based on the magnitude of nominal voltage and phase angle. Conventional PI + PR controller is implemented to track the reference voltage [110]. In secondary control, the real-time frequency is compared with the nominal value. The variation is then treated with a PI control to produce the frequency compensator Δf_f.

$$\Delta f_f = G_{FR}(f_n - f) \tag{3-47}$$

where G_{FR} is the PI controller gain in frequency restoration. The frequency compensator Δf_f is added to the nominal frequency to generate the threshold frequency.

Tertiary Control

As indicated with (3-44) and (3-45), the power sharing among ESs and DGs are accomplished based on their power capacities, which is not cost optimized. In this report, system operation cost is taken into consideration for the power dispatch of system units in tertiary control by comparing the system units' marginal costs which indicates the cost induced for additional unit of energy generated ($/kWh). The economic dispatch as explained in Section 3.1.2 is also implemented in this case.

Upon generation of the reference power, power sharing compensation is applied to minimize the error in power tracking. The power sharing compensation for BESi is as can be seen in the tertiary control in Fig. 3.2 and Fig. 3.5.

Similarly, for AC sub-grid, the actual and reference power of AC source are compared and the variation is treated with a PI control to produce the frequency compensator Δf_{Pi}. The threshold frequency for i^{th} AC source is:

$$f_{oi} = f_n + \Delta f_f + \Delta f_{Pi} \tag{3-48}$$

BIC power reference is generated as:

$$P_{BIC}^* = P_{net\_dc} + P_{BESs}^* \tag{3-49}$$

88

where P^*_{BESs} is BESs combined reference power. Power sharing compensation is implemented in tertiary control as displayed in Fig. 3.24. The difference between the actual and reference BIC power is treated with a PI control to produce the normalized compensator for power transfer ΔN. The difference in the normalized voltage and frequency is compared with ΔN to tune BIC power reference.

Deviations of DC bus voltage and AC frequency can be restored to the nominal values by implementing secondary control. In tertiary control, the power references of system units are obtained based on their marginal costs to minimize system operation cost. Power sharing compensation is also implemented to minimize the error in power tracking. In case of communication failure, system operation can still be supported with primary control. Therefore, both control accuracy and system reliability can be retained with the proposed multi-level EMS.

3.5   Simulation Verifications of Multi-level EMS for Hybrid AC/DC Microgrids

To verify the proposed multi-level EMS of the hybrid AC/DC microgrid, MATLAB/Simulink simulation has been performed. The schematic layout of the simulation model follows the schematic layout as in Fig. 3.23. The specifications of the simulation model are presented in Table 3.4.

Table 3.4 Simulation setups.

Parameters	*Value*
Nominal DC Voltage (V)	380
Allowable Voltage Variation (V)	±20
Nominal AC Frequency (Hz)	50
Allowable Frequency Variation (Hz)	±1
BES Power Capacity (kW)	10
DG Power Capacity (kW)	10
BIC Power capacity (kW)	5
DC Load (Ω)	36.1
AC Load 1 (kW)	2
AC Load 2 (kW)	4

Case 1

BES converter operated in VRM with droop control and the droop coefficient was 2 V/kW. System operated in islanded mode, thus DG operated in droop control as

well and the droop coefficient was 0.1 Hz/kW. BIC was disabled to isolate the sub-grids of AC and DC. The simulation results including load consumptions, normalized deviations of DC bus voltage and AC frequency are displayed in Fig. 3.26.
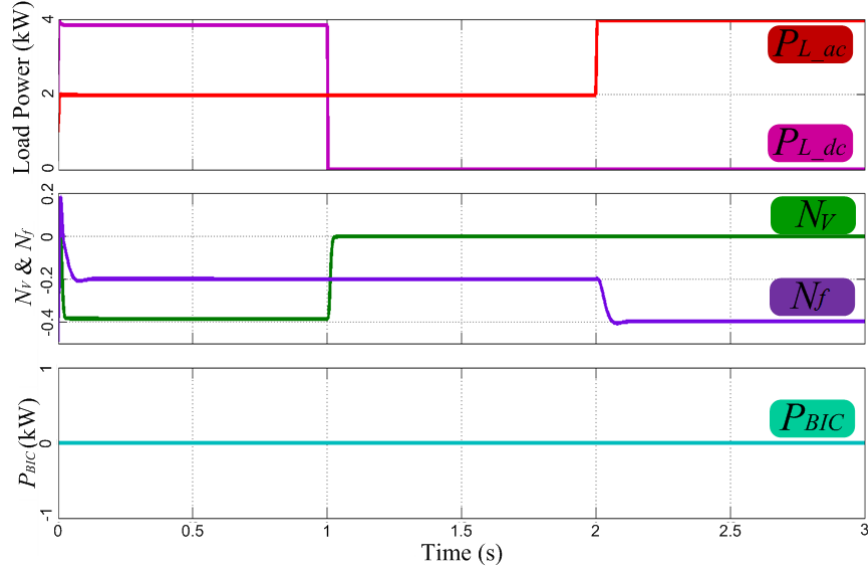
Fig. 3.26 Case 1 simulation results.

Initially, DC load and AC load 1 consumptions were 3.84 kW and 2 kW, respectively. DC bus voltage was regulated by the BES at 372.32 V with normalized deviation of -0.384 in steady state. AC frequency was regulated by DG at 49.8 Hz and the normalized deviation was -0.2. At 1 s, DC load was turned off, ES output power reduced to zero and thus the output voltage has increased to 380 V. The normalized DC bus voltage deviation changed to zero. At 2 s, AC load 2 was turned on and the combined AC load consumption was increased to 4 kW. AC frequency was decreased to 49.6 Hz with normalized deviation of -0.4 accordingly.

Case 2

The loading profile was unchanged from the one in Case 1 and the BIC was activated to operate in distributed manner. The simulation results are displayed in Fig. 3.27. Upon detection of AC frequency and DC bus voltage in BIC local controller, the deviations were normalized and compared to generate BIC power reference. BIC power transfer was stabilized at 0.17s with magnitude of 0.89 kW

from AC to DC sub-grid. With reduction of BES output power, DC bus voltage has increased. The normalized deviations of DC voltage and AC frequency were equalized and stabilized at -0.287.
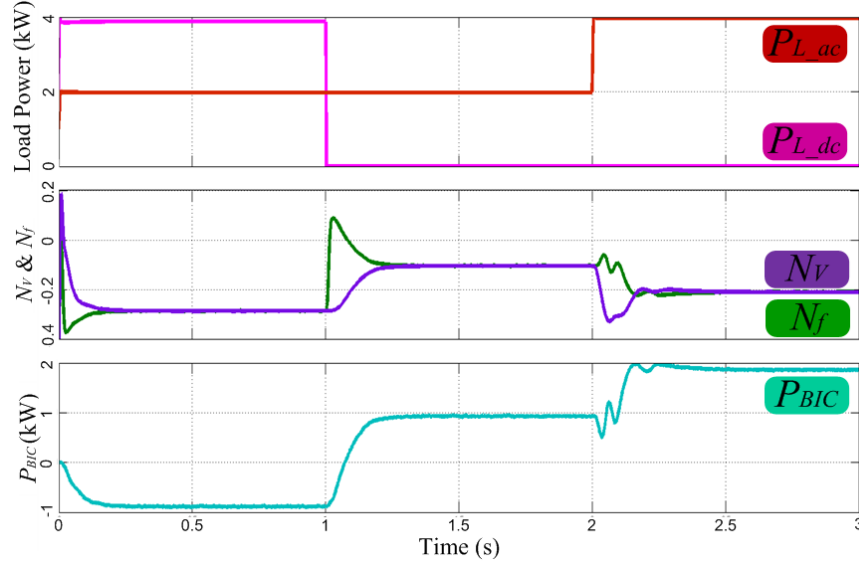
Fig. 3.27 Case 2 simulation results.

At 1 s, DC load reduction was activated hence DC bus voltage deviation was increased instantly. BIC changed the power transfer direction and stabilized at 0.93 kW from DC to AC. The normalized DC voltage deviation and AC frequency deviation were -0.105 in steady state. Similarly, at 2 s when AC load was increased to 4 kW, the difference in N_V and N_f was eliminated with the increment of BIC power transfer. System was stabilized with BIC power transfer of 1.86 kW and normalized deviations of -0.21. The oscillation during the transition was mainly due to the lag of BIC power tracking.

Case 3

Restorations of DC bus voltage and AC frequency was realized in secondary control. The resultant compensators for voltage restoration and frequency restoration were used to adjust the threshold voltage and frequency for BES, BIC and DG accordingly. The simulation results are as shown in Fig. 3.28.
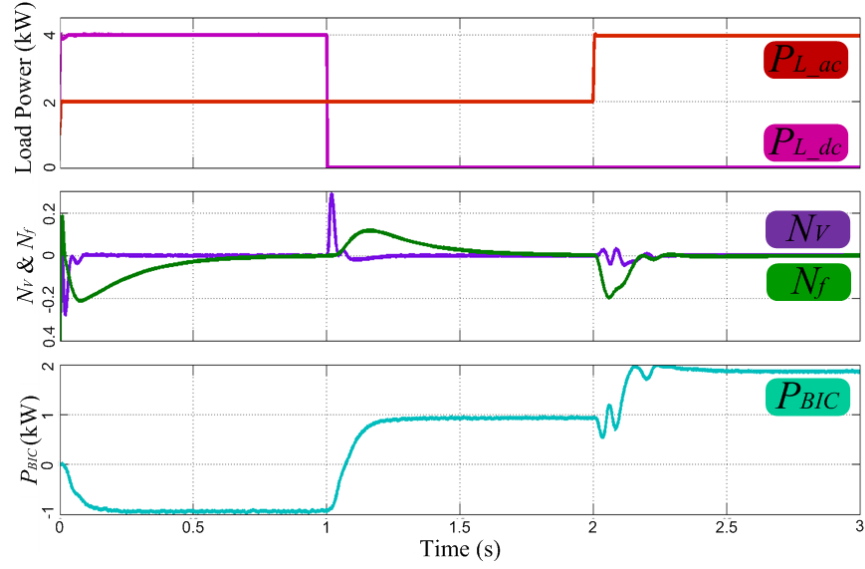
Fig. 3.28 Case 3 simulation results.

The normalized deviations of DC bus voltage and AC frequency were stabilized at zero in steady state in different loading conditions.

Case 4
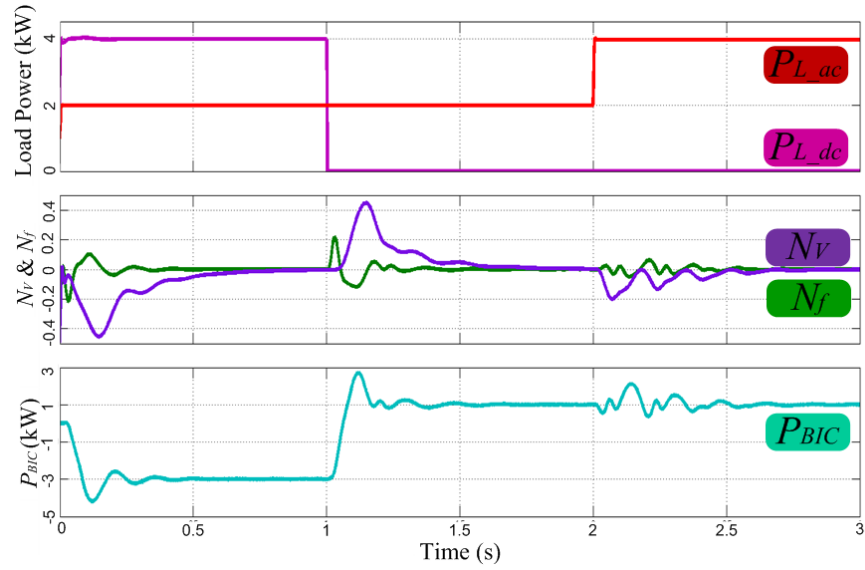
Fig. 3.29 Case 4 simulation results.

In tertiary control, the marginal costs of BES and DG were compared to determine their utilization priorities. The threshold power for activation of DG was determined to be 1 kW. Therefore, when the combined net power was lower than 1 kW, DG power reference was set to be zero and BES was scheduled to compensate

92

for the total load consumption. Otherwise, BES power reference should be set as 1 kW and the remaining power deficiency was to be compensated by DG until reaching its power capacity. BIC power reference was obtained to be -3 kW, 1 kW and 1 kW in the first, second and third loading profiles, respectively. The simulation results are as shown in Fig. 3.29. Compared with Case 3, the steady state BIC power has followed the reference values in different loading conditions.

Simulation cases have verified the effectiveness of the proposed multi-level EMS of hybrid AC/DC microgrid. In Case 1, sub-grids response in case of load variations without BIC for power transfer was verified. Deviations of AC frequency and DC voltage were proportional to the net power of the respective sub-grid. In Case 2, the deviations were normalized and compared to determine BIC power flow. The normalized deviations of AC frequency and DC voltage were equalized in steady state. In Case 3, DC voltage and AC frequency restorations were realized in secondary control to improve system power quality. The normalized deviations were restored to zero in steady state. In Case 4, marginal costs comparison was carried out for system power scheduling. Power sharing compensation helped minimizing the power tracking error. In case of communication failure, system stability can be remained with primary control in distributed manner as in Case 2. Therefore, the multi-level EMS improved system control accuracy while maintained the system reliability.

3.6   Conclusion

System bus voltage regulation and power sharing can be realized autonomously and effectively in distributed EMS. However, deviation in system bus voltage and error in power tracking become the main shortcomings due to the unpredictable transmission line impedance and the imposed droop relationship. Multi-level EMS of multiple-slack-terminal DC microgrid is thus proposed to enhance system control accuracy while retaining the reliability in case of communication failure.

Multi-level EMS for DC microgrid with multiple slack terminals has been validated with experimental cases in a lab-scale DC microgrid. The experimental

results show that bus voltage restoration is able to minimize bus voltage deviations in steady state. Economic dispatch which is applied in tertiary control to generate power references for slack terminals is also able to minimize system operation cost. Furthermore, power tracking error can be eliminated by implementing power sharing compensation.

For the transitions between islanded and grid-tied mode of DC microgrid, employment of multiple-slack-terminal DC microgrid has facilitated the reducing of bus voltage fluctuation and inrush current. BESs mode operation change is needless during islanding so that system bus voltage can be regulated actively throughout the transition. The proposed procedures can ensure seamless transitions between grid-tied and islanded modes. The contactor assisted decoupling BIC operating mode change and grid connection. The implementation of counter has ensured that voltages at both sides of contactor have been matched stably. Multi-level EMS implemented has eliminated the deviation in system bus voltage and error in power tracking both at grid-tied and islanded modes. BESs and BIC power dispatch based on utilization priority setting, battery SoC and real-time system net power has been successfully performed. The effectiveness of the proposed control methods has been validated with experimental case studies.

Multi-level EMS is also proposed for hybrid AC/DC microgrid control. In primary control, droop relationships are imposed for the sub-grids of AC and DC distributed EMS. System power balance can be indicated with AC frequency and DC voltage accordingly. The deviations of AC frequency and DC bus voltage are normalized and compared to determine BIC power transfer locally. In secondary control, restorations of DC bus voltage and AC frequency are implemented to enhance system power quality. The comparison of marginal costs of system units is implemented to determine their utilization priority in tertiary control. MATLAB Simulink model was developed to validate the proposed multi-level EMS for hybrid AC/DC microgrid control.

Chapter IV

EMS Strategy for Hybrid Energy Storages

4.1   Hybrid Energy Storages

Localized energy storages (ESs) are usually integrated in DC microgrid operation to mitigate system power imbalance because of the intermittency of RESs generation and uncertainty of load consumption [136]. There are many types of ESs that can be classified based on power density (kW/kg), energy density (kWh/kg), life cycle, ramp rate (kW/min), *etc.* [137-140]. Different types of ESs *e.g.* ultra-capacitor (UC), electro-chemical battery, flow-battery, compressed-air, pump-hydro, *etc.*, have different characteristics for different application hence none of ES satisfies all expected features [141]. For instance, with high power density and ramp rate ultra-capacitor only has low energy density [142]. In contrast, with high energy density flow battery only has limited ramp rate [17]. The implication is if only one type ES is implemented as in [55, 75], high installation cost will be resulted in order to meet all design specification of system.

Instead of increasing the number of ESs of the same type, hybrid energy storage system (HESS), which utilizes the most of different ESs characteristics, has been demonstrated to optimize the total system operation cost [80, 143-147]. Besides that, implementation of HESS also extends lifetime of ESs because power dispatch of ESs is conducted based on the characteristic of ESs. By dispatching power based on ESs' characteristics, *e.g.* limiting the output power change rate of low-ramp-rate ESs, the stress of low-ramp-rate ESs can be reduced significantly [79, 148, 149]. HESS has been applied in electrical vehicle (EV) and hybrid electrical vehicle (HEV) [150-152], buildings and offshore platforms [35, 152-154].

HESS coordination can be classified as passive [148], semi-active [142] or active [155]. The topologies of different HESS coordination with UC and battery are shown in Fig. 5.1 [156]. In passive coordination, both battery and UC are in parallel and directly connected to the bus. The uncontrollable power sharing

between battery and UC is expected since it depends on the terminal voltage variations. The implementation of passive coordination can be seen in EV and HEV.
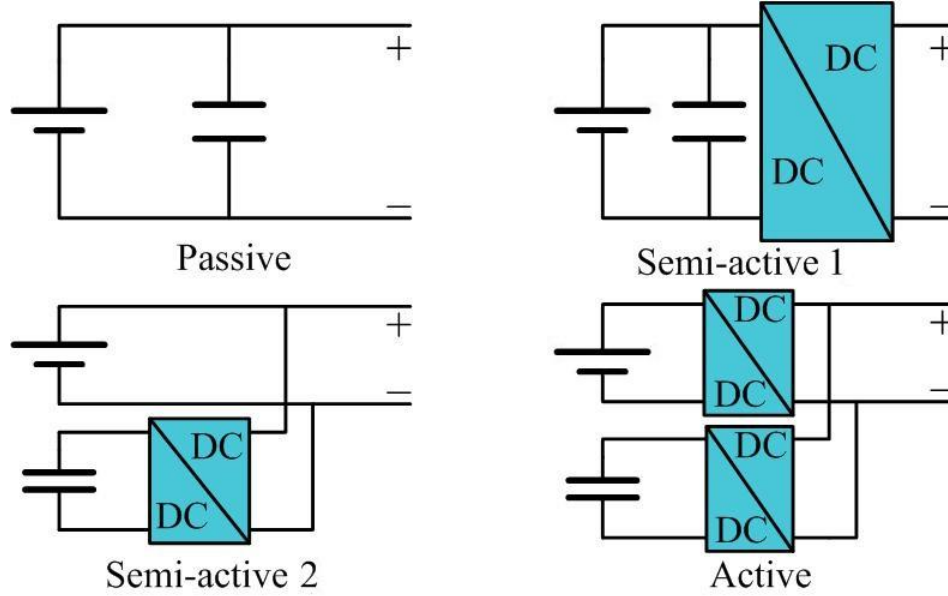
Fig. 4.1 Different types of HESS coordination topologies.

There are two kinds of semi-active coordination as shown in Fig. 4.1. HESS coordination of Semi-active 1 implements a DC/DC converter at the common connection point of battery and UC. This topology enables active output power control of ESs and eliminates the requirement of voltage matching between system bus voltage and ESs terminal voltage. However, UC energy capacity, which is proportional to its terminal voltage variations, is not be able to be fully utilized because UC terminal voltage variation is limited by the insignificant change of battery terminal voltage. In HESS coordination of Semi-active 2, a DC/DC converter is integrated at the output of UC. Therefore, the output power of UC might be controlled actively. Then again, the output power of the battery becomes uncontrollable since the battery terminal voltage is required to be matched with the nominal bus voltage.

As can be seen in Fig. 4.1, DC/DC converters are introduced at the outputs of both battery and UC in active coordination. The active coordination is the most superior of them all, not only because it eliminates the necessity of matched voltage

96

between ESs terminal voltages and system bus voltage [157], but also it can actively schedule ESs output power to fully utilize the power and energy capacities [158, 159]. Therefore, ESs active coordination is applied for HESS EMS strategy in this report.

The schematic layout of DC microgrid with the integration of RESs and various ESs is displayed in Fig. 4.2. RESs normally operate in MPPT mode with output power of P_{RESs}. The P_{Loads} indicates the combined load power consumption. The mismatched power between system load consumption and RESs generation is defined as system net power P_{net}.

$$P_{net}(t) = P_{Loads}(t) - P_{RESs}(t) \tag{4-1}$$

The ESs are integrated with their respective bidirectional DC/DC converters. Detailed schematic diagrams, mode operations and control methods of the converters follow as the one elaborated in Chapter II. P_{ESi} denotes the output power of the ith ES and P_{HESS} is the combined output power of ESs.
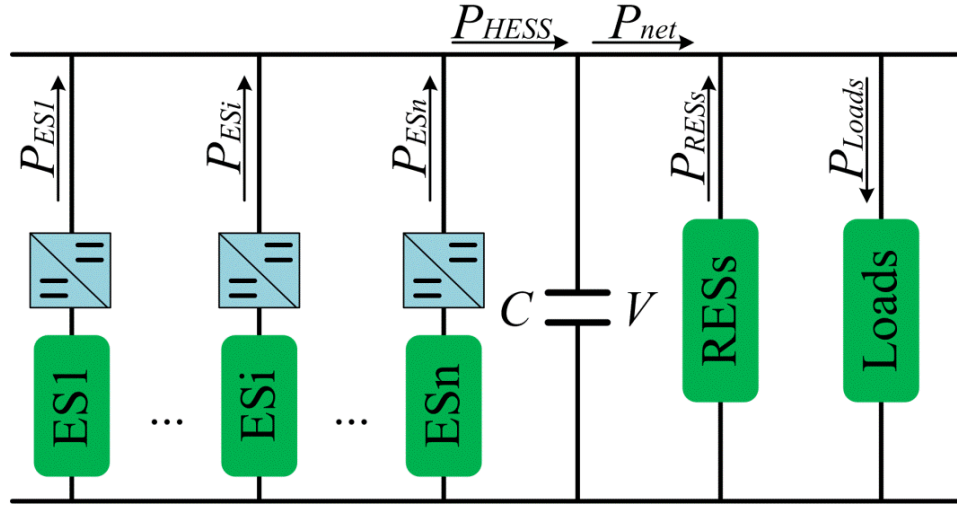
Fig. 4.2 Schematic layout of a generic HESS in DC microrgid.

The formulation of the relationship between the real-time bus voltage and real-time system power balance is as follows:

$$V(t)C\frac{dV(t)}{dt} = P_{HESS}(t) - P_{net}(t) \tag{4-2}$$

where C, V(t), P_{HESS}(t) and P_{net}(t) are the equivalent bus capacitance, system bus voltage in real-time, real-time ESs combined output power and real-time system net power, respectively. Bus voltage variation is eliminated only when the combined output power of ESs is the same with system net power. Therefore, the operation of HESS should be well controlled to track system net power precisely.

In the operation, system net power can be decomposed into high and low frequency elements [35, 160]. Power variations for hours is considered as the low frequency element, while power variation for minutes, seconds or even milliseconds is considered as the high frequency element [161-163]. To compensate the high frequency element, ESs with high response speed is needed to ensure rapid system net power tracking in order to minimize system bus voltage variation due to power imbalance [84, 142, 158, 160, 164].

ESs response speed is constrained by the thermal constraints, chemical reaction, *etc*. Ramp rate refers to the dynamic response of energy sources like traditional generator and RESs. In this report, ramp rate indicates the output power change of ESs in unit time (kW/min). Detailed ramp rate, energy capacity, power capacity and respective application of different type ESs have been included as in Table 4.1.

Table 4.1 Characteristics and applications of typical energy storages.

Energy Storage	Ramp Rate/Power Capacity	Power Capacity kW	Energy Capacity kWh	Application
Lead Acid Battery	$> \dfrac{0.18\text{kW / ms}}{1.26\text{kW}}$ [159]	<1000	1-1000	Power quality; Renewable source integration
VRB	$\dfrac{31\text{ MW / s}}{6\text{MW}}$ [165]	$10\text{-}10^7$	$<10^6$	Frequency regulation; Power quality
Fuel Cell with Electrolyzer	$\dfrac{0.25\text{ kW / min}}{3\text{kW}}$ [166]	<1000	$<2*10^6$	Vehicles; Time shifting
Ultra-capacitor	Considered infinite	1-100	<1	Frequency regulation; Transient stability
Compressed Air	$\dfrac{18\text{ MW / min}}{110\text{MW}}$ [167]	$10\text{-}10^6$	$10\text{-}10^6$	Load shifting

Energy storages are prioritized according to their ramp rates in this report. For convenience, with n total number of installed ESs, ES1 denotes the ES with the

highest priority and ESn is prioritized the lowest. ES with high ramp rate is termed as high ramp rate energy storage (HRES) and ES with low ramp rate is termed as low ramp rate energy storage (LRES) [168]. The main challenges of HESS coordination comprise system net power decomposition and ESs power dispatch based on their characteristics.

4.2   Distributed EMS of Hybrid Energy Storage System

HESS net power decomposition and power dispatch are normally fulfilled by implementing centralized EMS [81, 155, 169, 170]. Some techniques that have been implemented in HESS including low pass filter/high pass filter (LPF/HPF) [155], fuzzy logic control [80], wavelet [171], *etc*. The high frequency element of system net power is assigned as the power reference to HRES while the low frequency element to LRES [141, 171-175]. However, response delay because of the time needed for system status acquisition and ESs operating references assignment degrades the accuracy of real-time system net power. Consequently, significant bus voltage variations will be induced that degrades the system power quality.

Forecasting techniques for estimation of system net power to compensate the time delay have been proposed [79, 161]. Nevertheless, the forecasting time step of minutes or even hours are needed. It is thus not suitable for real-time operation. Besides, forecasting error also exists.

To minimize the effect of response delay, HRES is scheduled to operate in VRM and the rest LRESs operate in PCM [155, 176]. The low frequency elements of system net power are set as the power references for LRESs. HRES which operates in VRM regulates system bus voltage and autonomously compensates system power imbalance, whose variations are of high frequency [35]. All control algorithms for HESS introduced forehead are based on centralized EMS which heavily depends on the fluency of the communication link. If failure happens in communication link, the stabilized system operation cannot be retained.

99

4.2.1　System Net Power Decomposition

To improve system reliability in case of communication link failure, distributed EMS of HESS is proposed [177]. System bus voltage is considered as the global indicator for system power balance [41]. ESs operation is scheduled based on local bus voltage variations. ES1, which is of the highest ramp rate, operates in VRM with droop control [50, 62]:

$$V_{ES1}^{*} = V_{n} - m_{ES1} P_{ES1} \tag{4-3}$$

where m_{ES1}, P_{ES1} and V_{ES1}^{*} are the droop coefficient, output power and reference voltage of ES1, respectively. The remaining LRESs function in PCM and the power references which are obtained with reverse droop control is expressed as:

$$P_{ESi}^{*} = \frac{V_{n} - V}{m_{ESi}} \tag{4-4}$$

where m_{ESi} is the droop coefficient of ESi and P_{ESi}^{*} is the power reference of ESi. The droop coefficients of ESs are determined with their respective power capacity and the bus voltage range [55]. Therefore, ESi output power P_{ESi} in steady state is:

$$P_{ESi} = P_{net} \bigg/ (m_{ESi} \sum\nolimits_{j=1}^{n} \frac{1}{m_{ESj}}) \tag{4-5}$$

The relationship between bus voltage and system net power is:

$$V = V_{n} - (P_{net} \bigg/ \sum\nolimits_{j=1}^{n} \frac{1}{m_{ESj}}) \tag{4-6}$$

Implementing droop relationship, system bus voltage indicates the system net power variations. The control block diagrams of the HRES and LRESs are displayed in Fig. 4.3. ES1, which is of HRES, operates in VRM with droop control. Double-loop PI control is used to track the reference voltage. The rest ESs, which are of LRESs, operate in PCM whose power references are generated based (4-4). The reference inductor current is obtained by dividing the power reference with its respective terminal voltage V_{teri}. PI controller is implemented to track the reference inductor current.

100

(a)

(b)
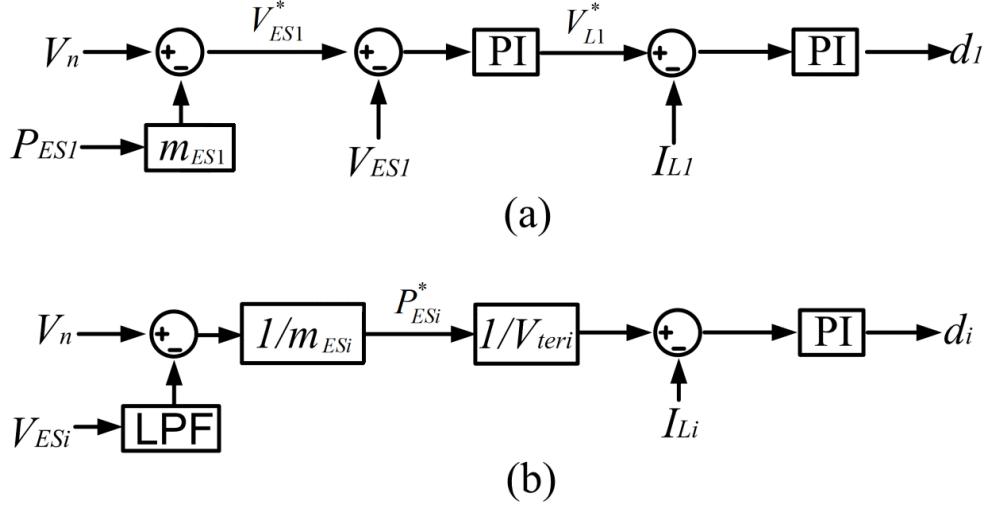
Fig. 4.3 Control block diagrams of HESS in distributed EMS for (a) ES1; (b) remaining ESs.

The output powers of LRESs are determined according to the comparison between local bus voltages and the nominal value. As seen in Fig. 4.3(b), to accomplish the decomposition of system net power, LPFs are integrated at the feedback bus voltage of LRESs. Low frequency element of local bus voltage is then compared with V_n and the difference is multiplied with the reciprocal of the droop coefficient to obtain the power reference P_{ESi}^*.

The cut-off frequency of LPF is determined based on the ramp rate of respective ES [149]. The relationship between ESi output power $P_{ESi}(t)$ and bus voltage $V(t)$ in real time is as follows:

$$(V_n - \frac{e^{(-t/T_{ESi})}}{T_{ESi}}V(t))\frac{1}{m_{ESi}} = P_{ESi}(t) \tag{4-7}$$

where $e^{(-t/T_{ESi})}/(T_{ESi})$ represents the first order LPF of ESi in time domain; T_{ESi} is the reciprocal of the cut-off frequency f_{ESi}. Differentiate (4-7) and combine with (4-2):

$$\left[\frac{1}{T_{ESi}^2}V(t) - \frac{1}{T_{ESi}CV(t)}\frac{dP_{net}(t)}{dt}\right]e^{(-t/T_{ESi})} = m_{ESi}\frac{dP_{ESi}(t)}{dt} \tag{4-8}$$

LRES output power changes with low frequency element of net power variation as indicated in (4-8). Therefore, this explains how decomposition of net power and

power dispatch among ESs are realized in distributed EMS. The ramp rate of ESi constrains the output power change of ESi.

$$f_{ESi}^2 V(t) - \frac{f_{ESi}}{CV(t)} \frac{dP_{net}(t)}{dt} \le \frac{m_{ESi} r_{ESi}}{e^{(-t/T)}} \tag{4-9}$$

where r_{ESi} is the ramp rate of ESi. The right hand side component is minimum when $t = 0$.

$$f_{ESi}^2 V(t) - \frac{f_{ESi}}{CV(t)} \frac{dP_{net}(t)}{dt} - m_{ESi} r_{ESi} \le 0 \tag{4-10}$$

From (4-10), the range of cut-off frequency can be obtained. The maximum cut-off frequency f_{ESi}^{max} is normally employed to maximize the utilization of ESs ramp rates.

$$f_{ESi}^{max} = \frac{dP_{net}^{max} + ((dP_{net}^{max})^2 + 4V(t)^3 C^2 m_{ESi} r_{ESi})^{1/2}}{2V(t)^2 C} \tag{4-11}$$

where dP_{net}^{max} is the maximum system net power change rate.

4.2.2   SoC Recovery in Distributed EMS

Since ES1 is the only slack terminal for system bus voltage regulation, it is critical to ensure stable operation of ES1. The output power of ES1 obtained based on (4-5) indicates that ES1 shares system net power with LRESs based on their droop coefficient setting. As long as system power imbalance exists, ES1 output power can never be zero. Usually ES with high ramp rate, like UC, is of low energy density. As a result, the stored energy of ES1, which is indicated with SoC, can vary significantly. Therefore, ES1 should operate in PCM to recover the nominal SoC SoC_{nom} in case SoC range is violated. Concurrently, reassignment of slack terminal is needed to regulate system bus voltage. System bus voltage variation will thus be induced during the reassignment process.

Therefore, to diminish the possibility of ES1 SoC range violation and the consequent system bus voltage variations due to slack terminal reassignment, autonomous SoC recovery is proposed for HESS distributed EMS [157].
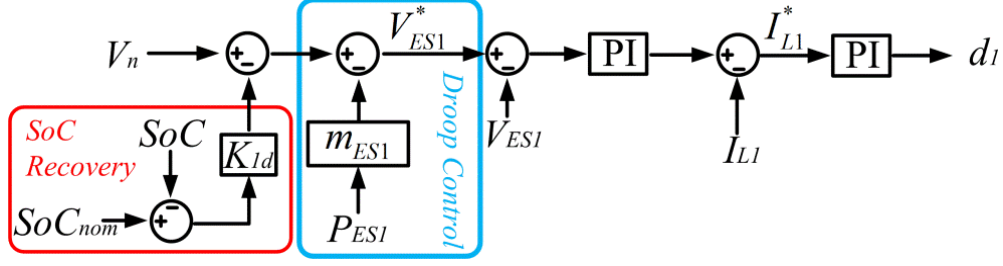
Fig. 4.4 ES1 control block diagram in distributed EMS of HESS with autonomous SoC recovery.

Fig. 4.4 displays the control block diagram of HESS distributed EMS with SoC recovery. A voltage compensator adjusts the reference voltage of ES1 to realize SoC recovery.

$$V^*_{ES1} = V_n - k_{1d}(SoC_{nom} - SoC) - m_{ES1}P_{ES1} \tag{4-12}$$

where K_{1d} is the autonomous SoC recovery coefficient of ES1 in distributed EMS. The modified ESs power sharing with SoC recovery is represented as:

$$P'_{ES1} = \frac{m_{ESs}P_{net} - K_{1d}(SoC_{nom} - SoC)}{m_{ESs} + m_{ES1}} \tag{4-13}$$

$$P'_{ESs} = \frac{m_{ES1}P_{net} + K_{1d}(SoC_{nom} - SoC)}{m_{ESs} + m_{ES1}} \tag{4-14}$$

where P'_{ES1} and P'_{ESs} are the modified output power of ES1 and rest ESs, respectively. m_{ESs} is the equivalent droop coefficient of the combined ESs (ES2 to ESn):

$$m_{ESs} = 1 \Big/ \left(\sum_{i=2}^{n} \frac{1}{m_{ESi}} \right) \tag{4-15}$$

The coefficient K_{1d} is determined as:

$$K_{1d} = \frac{m_{ESs}(P^{max}_{net} - P^{min}_{net})}{SoC_{max} - SoC_{min}} \tag{4-16}$$

where P^{max}_{net} is the maximum system net power, P^{min}_{net} is the minimum system net power, SoC_{max} is the upper boundary of ES SoC range variations and SoC_{min} is the lower boundary of ES SoC range variations. When the ES1 SoC is higher than SoC_{nom}, the compensated power is positive, and vice versa. ES1 SoC stabilizes

103

when P'_{ES1} is zero. The relationship between the bus voltage and system net power is expressed as:

$$V = V_n - \frac{K_{1d}m_{ESs}(SoC_{nom} - SoC) + m_{ES1}m_{ESs}P_{net}}{m_{ESs} + m_{ES1}} \tag{4-17}$$

4.3   Multi-level EMS of Hybrid Energy Storage System

With the proposed distributed EMS of HESS as elaborated in Section 5.2, system net power decomposition and ESs power dispatch can be realized effectively in distributed manner. System reliability and speed of response are enhanced as the communication link is not required. The proposed autonomous SoC recovery assists in reducing the possibility of slack terminal SoC range violation. However, degraded power quality and control accuracy, including bus voltage deviation and ES1 SoC variation in steady state, are always the main shortcomings of distributed EMS.
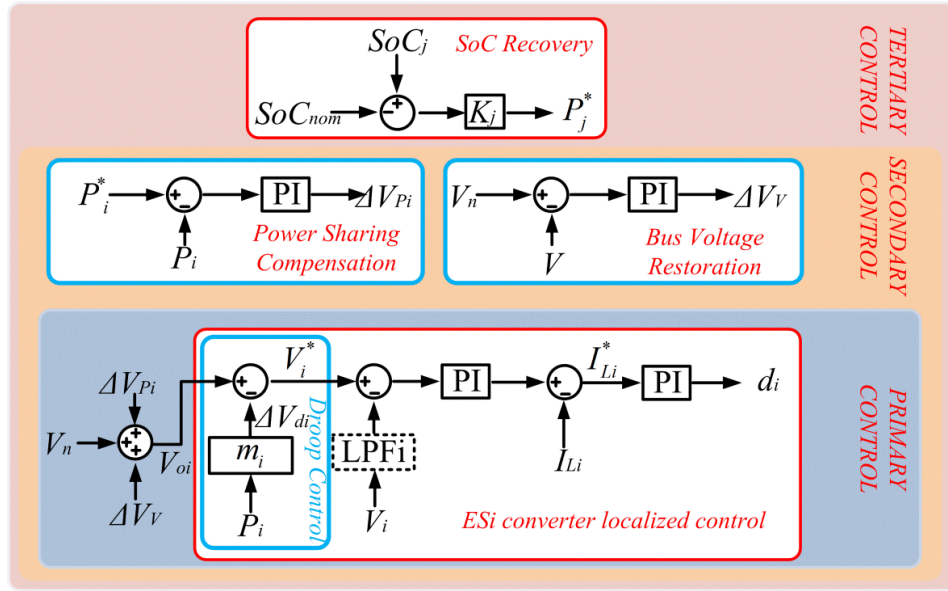
Fig. 4.5 Control diagram of multi-level EMS of HESS.

Therefore, hierarchical control of HESS, which is comprised of both centralized and distributed controls, has been proposed to ensure both system control accuracy and system reliability [177]. System operates with centralized EMS in normal state.

In case of communication failure, distributed control of HESS will be activated automatically to retain system operation with degraded control accuracy.

Nevertheless, hierarchical control of HESS has two main drawbacks, which are

    a Slack terminal reassignment in case ES1 SoC range is violated. System bus voltage is not regulated actively during the reassignment which will induce significant bus voltage variations.

    b Operating mode changes of ESs during the transition from centralized to distributed EMS in case of communication failure.

Therefore, to cope with the problems of hierarchical control of HESS, multi-level EMS of HESS is proposed. HESS distributed EMS with multiple-slack-terminal DC microgrid is applied as the primary control as displayed in Fig. 4.5. Localized LPF is installed for system net power decomposition and ESs power sharing in the primary control. Bus voltage restoration and power sharing compensation explained in Section 3.1 are employed in secondary control to enhance system control accuracy. In tertiary control, HRES SoC recovery is occupied to retrieve HRES SoC to the nominal value in steady state.

4.3.1　Primary Control

Distributed EMS with implementation of the multiple-slack-terminal described in Section 2.4 is realized in primary control. All ESs operate as slack terminals to regulate system bus voltage. Droop relationships are implemented for power sharing among ESs. The steady state bus voltage varies with the real-time system net power as expressed in (4-6).

The control schematic diagram for HRES remains the same as in Fig. 4.3(a). The reference voltage is produced based on droop control. The double-loop PI control is implemented to track the reference voltage and produce the duty ratio for power electronic switches. While for ESi of LRES, localized LPFi is applied at the feedback voltage so that it only responds to low frequency bus voltage variations as can be seen in Fig. 4.6.
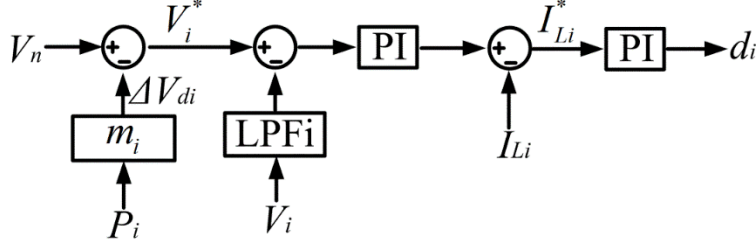
Fig. 4.6 Control diagram of ESi of LRES.

The difference between the reference voltage and low frequency element of the actual bus voltage is treated with a PI control to produce the reference inductor current. The relationship between ESi inductor current and system bus voltage is:

$$I_{Li}(t) = K_{Pi}(V_n - m_i P_i(t) - \frac{e^{-t/T_i}}{T_i}V(t)) + K_{Ii}\int(V_n - m_i P_i(t) - \frac{e^{-t/T_i}}{T_i}V(t)) \quad (4\text{-}18)$$

where K_{Pi} is the proportional coefficients of ESi and K_{Ii} is the integral coefficients of ESi in outer voltage loop, hence ESi output power is represented as:

$$P_i(t) = V_{teri}K_{Pi}(V_n - m_i P_i(t) - \frac{e^{-t/T_i}}{T_i}V(t)) + V_{teri}K_{Ii}\int(V_n - m_i P_i(t) - \frac{e^{-t/T_i}}{T_i}V(t)) \quad (4\text{-}19)$$

where V_{teri} is ESi terminal voltage. By deriving (4-19) and simplifying the equation with constant A:

$$A = K_{Pi} + K_{Ii}V_n - K_{Ii}m_i P_i(t) \quad (4\text{-}20)$$

Equation (4-19) becomes:

$$\frac{dP_i(t)}{dt} = \frac{(A - K_{Ii}\frac{e^{-t/T_i}}{T_i}V(t))(-\frac{e^{-t/T_i}}{T_i}\frac{dV(t)}{dt} + \frac{e^{-t/T_i}}{T_i^2}V(t))}{\frac{1}{V_{teri}} + m_i(A - K_{Ii}\frac{e^{-t/T_i}}{T_i}V(t))} \quad (4\text{-}21)$$

Substituting the differentiation of bus voltage with net power variation as stated in (4-2), the relationship between system net power change ΔP_{net} and ESi output power change turn out to be:

106

$$\frac{dP_i(t)}{dt} = \frac{(A - e^{-t/T_i} K_{Ii} f_i V(t))(\frac{-f_i \Delta P_{net}}{V(t)C} + e^{-t/T_i} f_i^2 V(t))}{\frac{1}{V_{teri}} + m_i (A - e^{-t/T_i} K_{Ii} f_i V(t))} \qquad (4\text{-}22)$$

where f_i is the cut-off frequency of LPFi. The ESi maximum ramp rate r_{ESi}^{max} constrains the output power change. The maximum output power variation takes place at $t=0$.

$$\frac{(A - K_{Ii} f_i V(t))(\frac{-f_i \Delta P}{V(t)C} + f_i^2 V(t))}{\frac{1}{V_{teri}} + m_i (A - K_{Ii} f_i V(t))} \leq r_{ESi}^{max} \qquad (4\text{-}23)$$

Substitute the real-time bus voltage to be the nominal value V_n.

$$\frac{-K_{Ii} V_n^2 f_i^3 + (AV_n + \frac{K_{Ii} \Delta P_{net}}{C}) f_i^2 - \frac{A \Delta P_{net}}{V_n C} f_i}{\frac{1}{V_{teri}} + m_i A - m_i K_{Ii} V_n f_i} \leq r_i^{max} \qquad (4\text{-}24)$$

Solve the equation (4-24) by taking the net power variation ΔP_{net} with the maximum system net power change dP_{net}^{max}, the maximum cut-off frequency f_{ESi}^{max} can be acquired. Therefore, the utilization of LRESi ramp rate can be maximized by setting the cut-off frequency for the LPF of LRESi to be f_{ESi}^{max}.

4.3.2 Secondary Control

Distributed EMS of HESS in primary control is not able to remove deviation in system bus voltage and error in power tracking because of imposed droop relationships and transmission line impedance, respectively [65]. Besides, HRESs shared powers in steady state are determined by system net power and their power capacities. It might lead to HRESs SoC range violation, which will result in degraded HESS overall ramp rate. Therefore, secondary control should be added.

In secondary control, the variation between the nominal bus voltage and actual system bus voltage is treated with a PI control to produce voltage compensator for

bus voltage restoration ΔV_V. Furthermore, power sharing compensation is realized by processing the variation between the reference and actual output power with PI control to produce the voltage compensator for power sharing compensation of respective slack terminal ΔV_{Pi}. The voltage compensators obtained in secondary control is used to adjust the threshold voltage of slack terminals.

$$V_{oi} = V_n + \Delta V_V + \Delta V_{Pi} \tag{4-25}$$

The updated threshold voltage generated in the central controller is sent to converter local controllers and generate respective reference voltage in droop control block.

4.3.3 Tertiary Control

Autonomous SoC recovery is proposed as tertiary control to avoid HRES SoC range violation as displayed in Fig. 4.5. The SoC of HRESj is compared with the nominal value SoC_{nom}. The variation is multiplied by coefficient K_j to produce power reference P_j^*.

$$P_j^* = K_j (SoC_j - SoC_{nom}) \tag{4-26}$$

When the SoC_j is lower than the nominal value, a negative power reference is produced to charge HRESj, and vice versa. The coefficient for autonomous SoC recovery is:

$$K_j = \frac{P_j^{max}}{\Delta SoC_j^{max}} \tag{4-27}$$

The generated power references are used to produce the voltage compensator for power sharing compensation in secondary control.

The advantages of the proposed multi-level EMS based control for HESS include:

a Eliminated the necessity for slack terminal reassignment in the event of ES1 outage.

b Seamless transition between centralized and distributed control as no operating mode change is needed.

4.4   Experimental Verifications of Multi-level EMS for HESS

A lab-scale DC microgrid as can be seen in Fig. 3.12 is used for experimental verification. The central controller acquires system operation status with updating frequency of 1 Hz. Li-ion battery with higher ramp rate and power capacity is assigned as ES1 to compensate the high frequency element of system net power variations and lead acid battery as ES2 to compensate the low frequency element of system net power. As the physical characteristics of ES1 and ES2 are close, the ramp rate of lead acid battery is set to be 1 kW/min to showcase the effectiveness of both HESS hierarchical and multi-level EMS control more intuitively. Detailed experimental setups are as represented in Table 4.2.

Table 4.2 Experimental setups.

Parameters	Unit	Setting
Nominal bus voltage	V	380
Allowable bus voltage variation	V	±10
PV1 power capacity	kW	1.3
PV2 power capacity	kW	1.4
HRES power capacity	kW	2
LRES power capacity	kW	1
LRES ramp rate	kW/min	1
HRES droop coefficient	V/kW	5
LRES droop coefficient	V/kW	10
Maximum load power change	kW	1
System equivalent capacitance	μF	3140

Two experimental cases have been performed to verify the effectiveness of the multi-level EMS for HESS control.

Case 1

Case 1 demonstrated HESS distributed EMS for system net power decomposition and ESs power scheduling. Both ES converters operate in VRM. Droop relationships were implemented for both ESs. The nominal bus voltage was 380 V and the maximum allowable bus voltage variation ΔV_{max} was ±10 V. Droop coefficients of ES1 and ES2 can thus be obtained to be 5 and 10 V/kW, respectively. As the maximum load power change rate is set to be 1 kW/min, the cut-off frequency of ES2 LPF was determined with (4-24) to be 1 Hz. Fig. 4.7

showed experimental results including PV generation, system bus voltage, ESs output powers and load consumption.
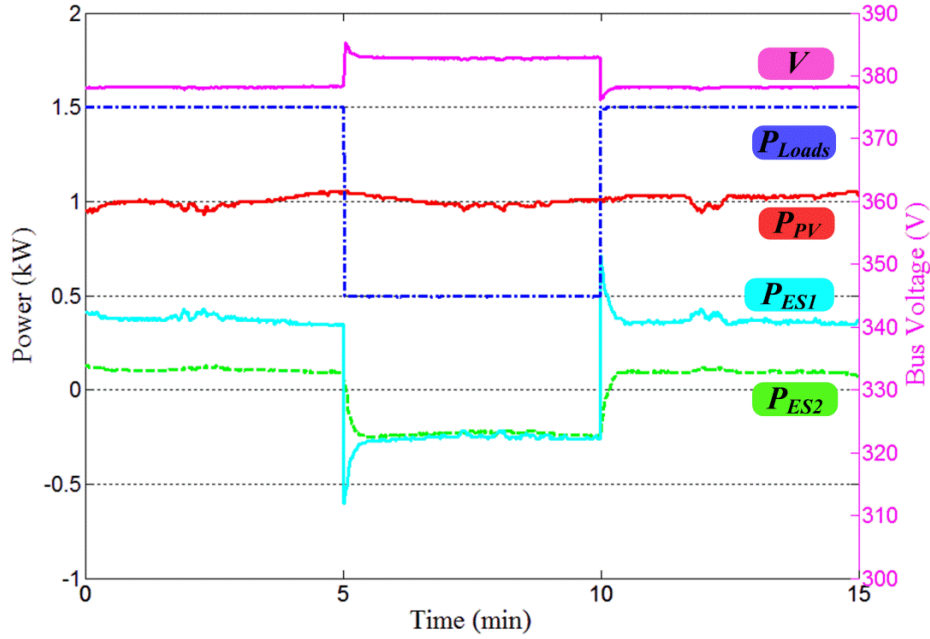
Fig. 4.7 Experimental results of distributed EMS for HESS.

Initially, system net power was 0.51 kW with load consumption of 1.5 kW and PV generation of 0.99 kW. Theoretically system bus voltage and ES1 shared power were 378.3 V and 0.34 kW, respectively. However, due to the transmission line impedance, ES1 shared power was 0.38 kW. System bus voltage, which was indicated with the average value of the measurements at both resistive and programmable loads, was stabilized at 378.2 V. The bus voltage deviation from the nominal value was 1.8 V.

At 5 min, load consumption was reduced to be 0.5 kW hence system net power was reduced to -0.52 kW. Therefore, to retain system power balance ES1 changed to charging stage immediately. Instant bus voltage surge of 7.1 V was observed because of the droop control and HESS response delay. ES2 output power was reduced gradually as it only response to low frequency element. System was stabilized at 5.4 min with ES2 output power of -0.25 kW and system bus voltage of 383 V. The steady state deviation in system bus voltage and error in power tracking were 3 V and 0.08 kW, respectively.

<u>Case 2</u>

In comparison, the operation of multi-level EMS for HESS was demonstrated in Case 2. HESS distributed control implemented in Case 1 was assigned as the primary control. Secondary control applied bus voltage restoration and power sharing compensation. The voltage compensators produced from secondary control were used to adjust the threshold voltage of respective ES local controller. ES1 energy capacity was set to be 0.5 kWh and the nominal SoC was 50% to show the effectiveness of the autonomous SoC recovery in tertiary control. ES1 power reference in steady state was determined with (4-26). The experimental results are displayed in Fig. 4.8.

From Fig. 4.8, it can be observed that the significant solar irradiation variation was observed. Output power range of PV converter was 0.84-1.28 kW. Initially, the load consumption was 0.5 kW and ES1 SoC was 58%. System bus voltage was retained at the nominal value with bus voltage restoration. ES1 output power has followed the reference value, which was 0.32 kW according to (4-26). The experimental result for HRES real-time SoC, reference power P_{ES1}^* and the actual output power P_{ES1} are displayed in Fig. 4.9. The SoC of ES1 was approaching to the nominal value during 0-5 min. HRES actual output power has followed the reference value closely with power sharing compensation. Because of the solar irradiation, variations ES1 output power oscillation with insignificant magnitude was observed.

At 5 min, load consumption was increased to be 1.5 kW hence instant ES1 output power increase was observed. The magnitude of system bus voltage sag was 6 V, which was similar to that of distributed EMS. However, when bus voltage deviation was detected, the voltage compensator ΔV_V was added to ESs threshold voltages to restore the system bus voltage. System bus voltage was restored to the nominal value at 5.6 min. Negative voltage compensator was generated in ES1 power sharing compensation block and was used to tune its threshold voltage. Thus ES1 output power was decreased gradually. ES1 output power was stabilized at 8

min with SoC of 50% and reference power of 0 kW. ES2 has countered the low frequency bus voltage variations and the output power was increased gradually.
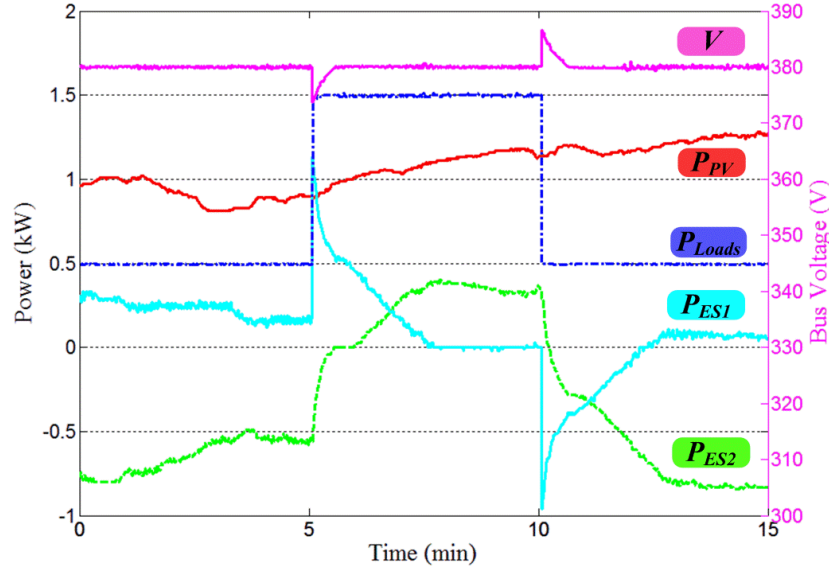
Fig. 4.8 Experimental results of multi-level EMS for HESS.
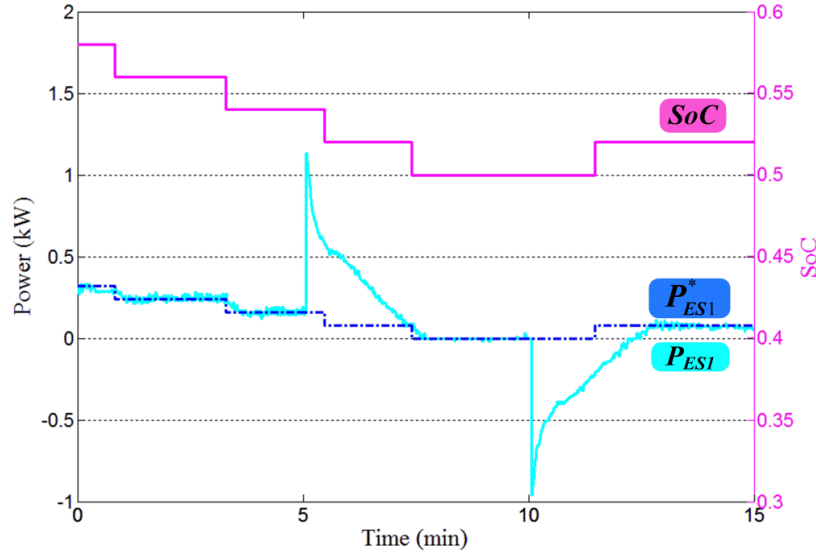
Fig. 4.9 Autonomous SoC recovery in Case 2.

At 10 min, load power reduction to 0.5 kW was activated hence ES1 discharged 1 kW of power instantly to rebalance system power. On the contrary, ES2 output power reduced gradually from 0.35 kW to -0.8 kW. Because of charging stage happened during the transition, ES1 SoC was raised to 52% at 11.5 min. ES1 output power was maintained at 0.08 kW with zero error in power tracking at 12.8

min. During the transition, bus voltage surge of 6.6 V has occurred. However it could be subsided within the duration of 0.66 min.

Case 1 has verified the effectiveness of HESS distributed EMS for system net power decomposition and ESs power scheduling. ES1 has accommodated the high frequency net power variations whereas ES2 has reacted to low frequency variations autonomously in case of system net power change. However, bus voltage deviation and power sharing errors exist in steady state. Therefore, multi-level EMS of HESS thus implemented in Case 2. Case 2 has proven that system control accuracy has been enhanced by employing multi-level EMS of HESS. Bus voltage restoration and power sharing compensation have eliminated deviation in system bus voltage and error in ESs power tracking, respectively. In tertiary control, autonomous SoC recovery has limited ES1 stored energy range variation effectively. Multi-level EMS for HESS has shown higher control accuracy compared with the distributed EMS, but the durations of bus voltage stabilization and ESs power tracking were longer.

4.5   Conclusion

EMS strategies for HESS coordination are proposed in this report. Two types of strategy, *i.e.* distributed and multi-level EMS of HESS have been elaborated. System net power decomposition and ESs power dispatch can be achieved autonomously and effectively in distributed EMS of HESS. Since local bus voltage is used as global indicator of system power balance the communication link is not required. Besides, the slack terminal SoC range violation can be avoided by implementing autonomous SoC recovery. However, the main drawbacks of distributed EMS including degraded power quality and control accuracy always exist.

Therefore, multi-level EMS of HESS is proposed to improve system control accuracy and reliability. Multi-level EMS of HESS consists of primary, secondary and tertiary control. In primary control, multiple-slack-terminal distributed EMS of HESS, in which all ESs are scheduled to operate in VRM, is implemented. With

the implementation of multiple-slack-terminal in primary control, slack terminal reassignment in the event of ES1 failure and ESs operating mode change in the event of disruption in communication link can be eliminated. System net power decomposition and ESs power sharing are performed autonomously using the integration of LPFs at LRESs. The relationship between the cut-off frequency and ES ramp rate has been elaborated in detail. In secondary control, bus voltage restoration and power sharing compensation are applied to remove the voltage deviation and power sharing errors, respectively. Moreover, autonomous SoC recovery is used in tertiary control to limit the SoC variation of the ESs with high ramp rate. In case of communication failure, system operation can still be retained with primary control. The effectiveness of multi-level EMS of HESS control has been verified with a lab-scale DC microgrid in experimental verifications section.

Chapter V

Optimal Depth-of-Discharge Range and Capacity Settings for Battery Energy Storage

Battery energy storages play an important role in mitigating system power imbalance in DC microgrids due to RESs intermittency and sudden load change. Since BES capital cost is proportional to its capacity size, selection of BES capacity should be optimized to reduce system cost [112]. A lot of works related to battery sizing have been done in DC microgrids [113-118]. Research in [113-115] determined the optimal rating of energy storage based on an optimal scheduling and cost-benefit analysis in DC microgrids. Optimal BES sizing considering reliability aspect is also implemented in DC microgrids [117, 118]. However, depth of discharge (DoD) and DoD range (DoD_r) during system operation have not been considered.

The DoD_r is a range that limit BES operation set between the minimum DoD to protect BES from over-charged and the maximum DoD to protect BES from over-discharged [59]. The DoD_r should be considered in DC microgrid operation since it affects the actual BES capacity and lifetime. Different implementation of DoD_r results in different amount of system operation cost.

System cost of DC microgrids includes fixed and variable cost. System operation cost is of variable cost which varies according to the power output including fuel cost, replacement cost, BES lifetime degradation cost, cost of energy not supplied, *etc*. Chaouachi, *et.al*. [119] and Mohamed, *et.al*. [120] have proposed the multi-objectives methods to optimize DC microgrid system operation cost and environmental impacts. However, the cost of BES lifetime degradation in the system operation was not considered. Sechilariu, *et.al*. [121] and Carpinelli, *et.al*. [122] included the cost of BES lifetime degradation in optimization method but the actual DoD of BES that is an important factor of BES lifetime was not modeled. The quantified relationship between the actual DoD of BES during the operation

which affects the BES lifetime and the system operation cost has been investigated [92, 93, 123]. However, DoD_r setting based on system resource and load conditions was missed.

Lifetime of a BES depends on many parameters such as operating DoD, discharge rate, temperature, *etc*. [124-126]. One important parameter is the actual DoD which is constrained by DoD range [124, 126]. In most studies, the DoD range was set without considering the effect to overall system operation cost. The smaller range of DoD which is selected, the longer BES lifetime will be expected. However, small DoD range limits the actual BES capacity. Lower available energy capacity causes more load curtailment or energy not supplied. Customer interruption cost will be incurred in the event of load curtailment [127]. Customer interruption cost due to energy not supplied was not considered in system operation cost functions of most studies.

In this report, BES lifetime degradation and the cost of energy not supplied are modeled as two important components of system operation cost. The cost of BES lifetime degradation is derived from replacement cost and the expected BES lifetime while cost of energy not supplied is obtained using the sector customer damage functions. The DoD range and BES capacity are selected under the minimum system operation cost. The system resource and load conditions are also considered in the optimization. An analytical method is implemented to solve the optimization problem and to obtain the optimal BES DoD range and capacity. MATLAB simulations have been carried out to verify the proposed method.

5.1 Modeling of System Units

A typical DC microgrid as can be seen in Fig. 1.1 usually consists of RESs, conventional generators, energy storages, and loads. It can either be grid-tied or islanded mode of operation. Photovoltaic (PV) panels, wind turbine and BES are connected to a DC microgrid through bidirectional DC/DC converters, wind turbine converter and bidirectional converter, respectively. Non-critical and critical loads are connected either directly or through converters to the DC microgrid.

116

RES power output is proportional to the source which varies in times and depends on the weather conditions. These fluctuations and load changes cause system power imbalance in DC microgrids. Power imbalance causes system bus voltage variation which reduces the power quality. Hence, BES is implemented to compensate RESs generation variations and to enhance system power quality. The models of components are elaborated as follows:

5.1.1 PV Modeling

The model of a solar PV cell has been presented in Section 2.2.1. The power output of PV arrays is depended on atmospheric insolation and weather condition. The 24-hour atmospheric insolation I_s at a particular location is determined based on the declination of a PV array, solar hour angle and sunset hour angle [128].

The optimal operation and control of a DC microgrid requires the accurate PV output model. Insolation data can be obtained using the forecasting techniques such as the artificial neural networks [116, 129], auto-regressive moving average (ARMA) [130, 131] or nonlinear auto-regressive with exogenous input [132]. The ARMA model which is used in this paper to model insolation $I_s(t)$ at period time t is expressed as:

$$I_s(t) = \sum_{i=1}^{p} \alpha_i I_s(t-i) + \sum_{j=1}^{q} \beta_j e(t-j) \tag{5-1}$$

where p, α_i, q, β_j and $e(t)$ are the order of the auto-regressive (AR) process, the AR coefficient, the order of the moving average (MA) error term, the MA coefficient and the white noise that produces random uncorrelated variables with zero mean and constant variance, respectively [131].

The power output of a PV array at period time t can be calculated as [116]:

$$P_{pv}(t) = \eta \cdot S \cdot I_S(t) \cdot \left(1 - 0.005 \cdot \left(t_0(t) - 25\right)\right) \tag{5-2}$$

where η, S, and $t_0(t)$ are the conversion efficiency, the array area (m^2), and the air temperature (°C), respectively.

117

The operating cost of the given PV arrays is assumed to be zero in cost modeling since the fuel cost is free. Therefore, PV generation system is normally controlled to operate in maximum power track (MPPT) mode at most of the time in order to harness the maximum power.

5.1.2 Load Modeling

Load profile is important for operation control and BES sizing of a DC microgrid. Time varying load model is usually determined using load forecasting techniques [118]. Load forecasting techniques include regression method, time series method, artificial neural networks method, fuzzy logic method [133]. The ARMA model used to forecast the load level $P_{load}(t)$ at period time t is expressed as:

$$P_{load}(t) = \sum_{i=1}^{r} \delta_i P_{load}(t-i) + \sum_{j=1}^{s} \varepsilon_j g(t-j) \tag{5-3}$$

where r, δ_i, s, ε_j and $g(t)$ are the order of the AR process, the AR coefficient, the order of the MA error term, the MA coefficient and the white noise that produces random uncorrelated variables with zero mean and constant variance, respectively [131].

5.1.3 BES Modeling

BES is installed to mitigate the power imbalance of DC microgrids especially in islanded mode. To retain the power balance in islanded DC microgrids with the integration of renewable energy sources and BES, operating mode of a BES is frequently changed with time between charging and discharging state. Two important on-line parameters at period time t for modeling the operation of a BES are discharging/ charging current $I(t)$ and actual depth of discharge $D_A(t)$ [134].

The DoD of a BES is an absolute discharge capacity relative to the rated BES capacity. The actual DoD at the end of period time t can be determined as:

$$D_A(t) = \begin{cases} D_A(t-1) - \left(\dfrac{\Delta t \cdot I(t)}{C_R} \right), & \text{at charging event} \\[2ex] D_A(t-1) + \left(\dfrac{\Delta t \cdot I(t)}{C_R} \right), & \text{at discharging event} \end{cases} \tag{5-4}$$

where $D_A(t-1)$, Δt, $I(t)$, C_R are the actual DoD at the end of period time $t-1$, duration of charging/discharging event, charging/discharging current at period time t and rated capacity, respectively. During system operation, the value of $D_A(t)$ is constricted within the DoD range.

The lifetime degradation cost of a BES is influenced by the expected BES lifetime which depends on charging/discharging pattern in system operation. Therefore, the estimation of expected BES lifetime is required. The expected BES lifetime $EBL(T)$ for operation time T, which has experienced the specified usage pattern is determined as [134]

$$EBL(T) = \frac{C_R \cdot D_R \cdot L_R}{\displaystyle\sum_{m=1}^{n} d_{eff}(m)} T \tag{5-5}$$

where C_R is the rated capacity (Ah) at rated discharge current; D_R is the DoD at which the rated cycle life was determined; L_R is the cycle life at rated depth of discharge D_R and rated discharge current; n is the number of discharge events that are experienced during T; $d_{eff}(m)$ is the effective capacity discharge (Ah) for discharge event m which is occurring at period time $t = t_m$, as adjusted for the actual depth of discharge $D_A(t_m)$ and the actual rate of capacity discharge $d_{actual}(t_m)$. The formulation of $d_{eff}(m)$ is as follow:

$$d_{eff}(m) = \left(\frac{D_A(t_m)}{D_R} \right)^{u_0} e^{u_1\left(\frac{D_A(t_m)}{D_R} - 1 \right)} \frac{C_R}{C_A(m)} d_{actual}(t_m) \tag{5-6}$$

where $d_{actual}(t_m)$ is expressed as:

$$d_{actual}(t_m) = \Delta t \cdot I(t_m) \tag{5-7}$$

Coefficients u_0 and u_1 in (5-6) are determined by applying a curve fitting technique to the cycle life versus DoD data provided in the battery datasheet [92]. Once the cumulative effective amp-hour discharge is obtained for T, EBL can be evaluated using (5-5) for the calculation of the annual operating cost of BES lifetime degradation.

One year operation time is used with a timestamp of half-an-hour in this case. During the simulation of one year microgrid operation the cumulative effective discharge of BES, the amount of load curtailment and the generation curtailment for certain DoD range and BES capacity are obtained. These results are used for the calculation of system operation cost that is elaborated in the later section.

However, the model has some limitations which are it does not take into account the battery environmental conditions, it is not capable to capture the charge redistribution phenomenon and the non-linear losses taking place in the BES.

5.2 DC Microgrids System Operation Cost Modeling

The operation costs of a DC microgrid consist of the cost of BES lifetime degradation, cost of fuel, price of electricity, cost of reliability due to customer interruption, *etc*. System operation cost models of an islanded microgrid under different DoD range, DoD_r and different BES capacity, C_R are presented as follows:

5.2.1 BES Lifetime Degradation Cost

The one-time capital cost (CC) which includes the BES investment and installation cost is proportional to rated capacity (C_R) and rated power (P_B^{max}) of BES. It is expressed as:

$$CC = k_P \cdot P_B^{\text{max}} + k_C \cdot (\frac{C_R \cdot V_B}{1000}) \tag{5-8}$$

where k_P, k_C and V_B are the rated power cost rate ($/kW), the rated capacity cost rate ($/kWh) and BES terminal voltage (V), respectively. Because the main concern is system operation cost which varies according to actual output and the BES is not newly installed, only replacement cost (RC) is considered in cost of BES lifetime

degradation. The amount *RC* of is assumed to be 60% of *CC* since *RC* does not include the preliminary installation cost [135]. In this work, the main concern is the capacity of BES, therefore the rated power of BES is tied proportionally with the capacity of BES.

The annual BES lifetime degradation cost changes with different *EBL* according to the selection of *DoD$_r$*. The minimum DoD of *DoD$_r$* in this paper is set to be 0%. Based on *EBL* and the interest rate *r*, the equivalent annual BES lifetime degradation cost (*C$_{BES}$*) under certain *DoD$_r$* and *C$_R$* can be calculated as:

$$C_{BES}(DoD_r, C_R) = \frac{r(1+r)^{EBL}}{(1+r)^{EBL} - 1} \cdot RC \tag{5-9}$$

Larger *DoD$_r$* and *C$_R$* means larger available capacity which cause larger *C$_{BES}$* because of the extensive utilization of BES. The reverse also applies; smaller *DoD$_r$* and *C$_R$* cause smaller *C$_{BES}$*.

5.2.2   Cost of Energy Not Supplied

When the total generation from RES and stored energy of BES is less than the total load, some loads have to be curtailed. Load curtailment incurs customer interruption cost. For the same load curtailment, the cost may not be the same for different customers. The sector customer damage functions (SCDFs) were used to determine customer interruption cost (*CIC*) [118, 127]. The annual cost of the load curtailment *C$_{ENS}$* based on *CIC* under *DoD$_r$* and *C$_R$* is expressed as:

$$C_{ENS}(DoD_r, C_R) = \sum_{z=1}^{N} CIC(\Delta ls_z) \cdot P_{LS}(t_z) \tag{5-10}$$

where *N* is the number of load curtailment events for a year; *P$_{LS}$(t$_z$)* is load curtailment for event *z* which is occurring at period time *t = t$_z$*; and *Δls$_z$* is duration time of the load curtailment for event *z*.

5.3 Problem Formulation and Solution Procedure

5.3.1 Problem Formulation

The selection of DoD_r and C_R affect the scheduling of BES discharging/charging event, the total of load curtailment, the total of generation curtailment and *EBL*, which may lead to different total system operation cost (*TC*) of a DC microgrid. The *TC* of a DC microgrid consists of the cost incurred from BES lifetime degradation and the cost of energy not supplied, which is represented as:

$$TC(DoD_r, C_R) = C_{BES}(DoD_r, C_R) + C_{ENS}(DoD_r, C_R) \tag{5-11}$$

The objective of the optimization algorithm is to determine the optimal DoD_r (DoD_r^{opt}) and optimal C_R (C_R^{opt}) under the minimum *TC* subject to the following constraints:

Power balance constraint:

$$P_B(t) = \left(P_{PV}(t) - P_{PVc}(t)\right) - \left(P_{load}(t) - P_{LS}(t)\right) \tag{5-12}$$

where P_B is BES charging/discharging power to compensate power mismatch, P_{PV} is PV power, P_{PVc} is PV generation curtailment power, P_{load} is load consumption, P_{LS} is load curtailment power.

BES charging/discharging constraint:

$$0 \leq P_B \leq P_B^{\max} \tag{5-13}$$

where $P_B^{\max}$ is the upper limit of charging/discharging power of BES.

DoD range constraint:

$$DoD_r^{low} \leq DoD_r \leq DoD_r^{upp} \tag{5-14}$$

where DoD_r^{low} and DoD_r^{upp} are the lower and the upper limit of DoD_r, respectively.

5.3.2 Solution Procedure

Let $\mathbf{x} = \begin{bmatrix} DoD_r & C_R \end{bmatrix}$, the objective function (J_{DC}) is expressed as:

122

$$J_{DC} = \min\left[TC(\mathbf{x})\right] \qquad\qquad (5\text{-}15)$$

The objective is to determine the optimal $\mathbf{x}$. The flowchart of the optimization procedure is shown in Fig. 5.1. The iteration procedure is implemented to obtain optimal $\mathbf{x}$. For each iteration and the updated DoD_r and C_R, power mismatch to be compensated by BES and the corresponding TC will be calculated.
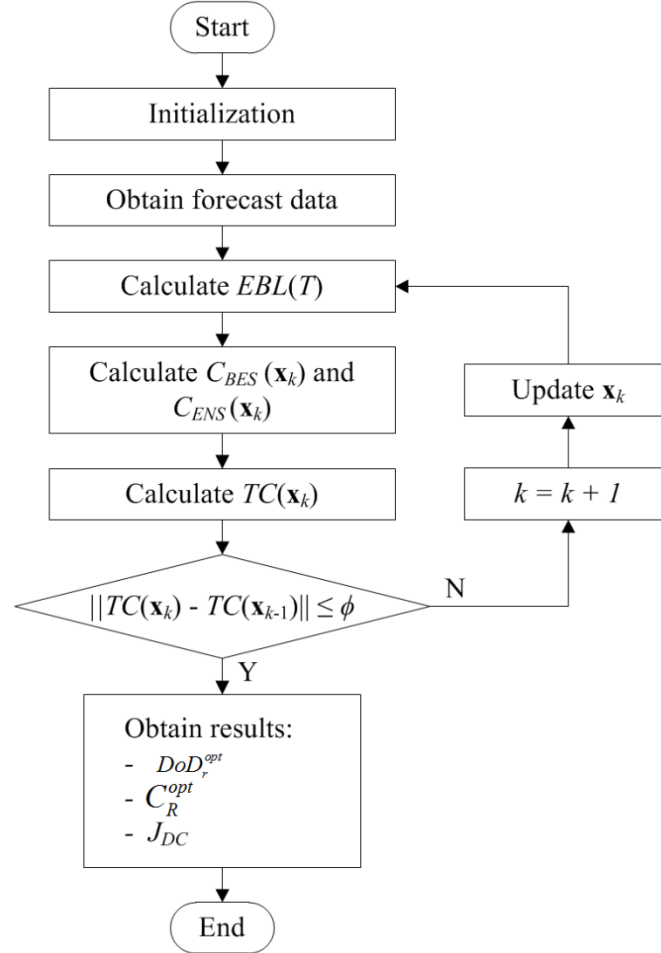
Fig. 5.1 Flowchart of DoD_r and C_R optimization procedure.

This algorithm will obtain the TC minimum under different DoD range between DoD range constraint as stated in (5-14); and under different BES capacity. This algorithm is executed as long as the termination conditions or the limit of the parameter has not been reached. The termination condition is satisfied when the global minimum TC (J_{DC}) is reached. The termination condition is expressed as.

$$\left\| TC(\mathbf{x}_k) - TC(\mathbf{x}_{k-1}) \right\| \leq \phi \qquad\qquad (5\text{-}16)$$

where $TC(\mathbf{x}_k)$, $TC(\mathbf{x}_{k-1})$ and ϕ are the TC at iteration k, the TC at iteration $k-1$ and the termination value, respectively. The J_{DC} is reached when the difference between $TC(\mathbf{x}_k)$ and $TC(\mathbf{x}_{k-1})$ is equal or lower than ϕ. With this condition, J_{DC} is equal to TC at iteration $k-1$.

$$J_{DC} = TC(\mathbf{x}_{k-1}) \qquad\qquad (5\text{-}17)$$

Under J_{DC}, optimal DoD range (DoD_r^{opt}) and capacity (C_R^{opt}) are obtained. The detail of the algorithm is as follows:

1) Set the initial value of DoD range ($DoD_r^{ini} = DoD_r^{upp}$), set the initial value of BES capacity (C_R^{ini}), set the initial index k to be 1.
2) Obtain forecast PV power output and forecast load model data.
3) Calculate the cumulative effective discharge of BES, the amount of load curtailment and the generation curtailment under DoD_r and C_R. Then calculate $EBL(T)$ using (4-5).
4) Calculate $TC(\mathbf{x}_k)$ consisted of $C_{BES}(\mathbf{x}_k)$ and $C_{ENS}(\mathbf{x}_k)$.
5) Check whether the termination condition in (4-16) has been reached or not. If the termination condition has been reached, the process can continue to step 7.
6) Update $\mathbf{x}_k$ which consist of DoD_r and C_R. In updating $\mathbf{x}_k$, the algorithm checks whether $DoD_r(k)$ has reached the lower limit DoD_r^{low} or not. If not, updates index k using $k = k + 1$; updates DoD_r using $DoD_r(k) = DoD_r(k-1) - \Delta D$; and updates $C_R(k)$ using $C_R(k) = C_R(k-1) + \Delta C$. Where $DoD_r(k-1)$, ΔD, $C_R(k-1)$, ΔC are the previous DoD_r, the iteration step size of DoD range, the previous C_R, and the iteration step size of BES capacity, respectively. Repeat step 3 to 6 until termination condition is met or the limit of the parameter has been reached.
7) Obtain DoD_r^{opt}, C_R^{opt} and J_{DC}.

5.4 Simulation Verifications

The islanded DC microgrid as can be seen in Fig. 1.1 is simulated using MATLAB to illustrate the proposed models and method. Intensium Flex High Energy Lithium-Ion battery is used in this simulation. Based on the 2014 historical data obtained from Water and Energy Laboratory at Nanyang Technological University

and Energy Market Authority Singapore of solar irradiance and load profiles, respectively, one year data of PV power output and load profiles are obtained from the simulation as shown in Fig. 5.2. The dotted line represents PV power output while the solid line represents the load.
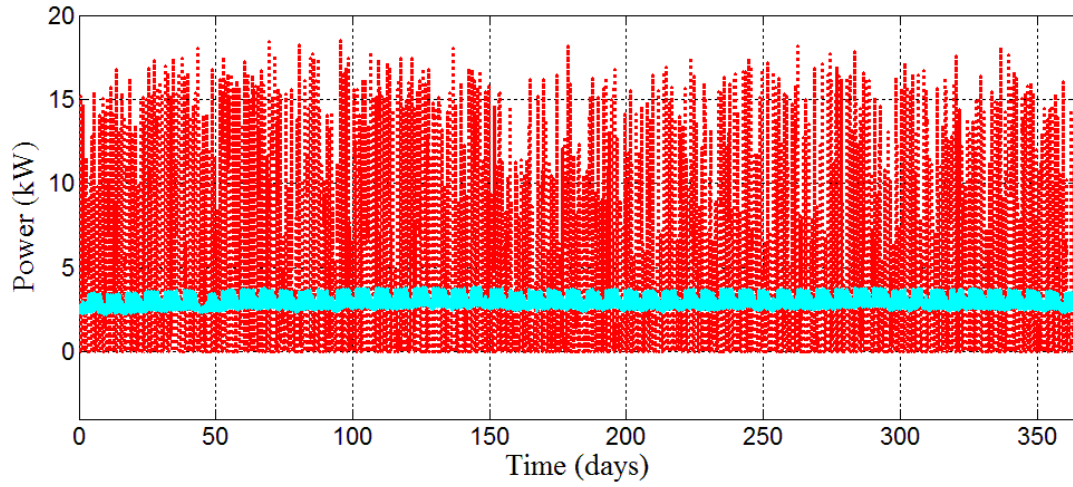
Fig. 5.2 Half-hourly PV power output and load profiles for a year.

The PV power output and load profiles for a certain day are shown in Fig. 5.3. The dashed line in Fig. 5.3 shows the power mismatch P_{diff} between PV output and load profiles.
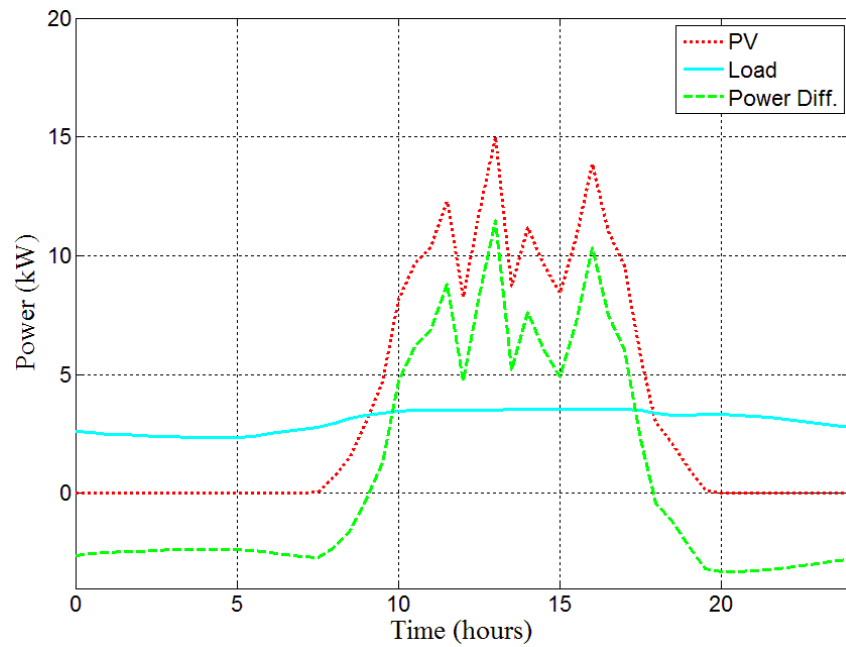
Fig. 5.3 PV power output and load profiles for a certain day.

The time interval of a period is 30 minutes. The average energy consumed by load is 75 kWh/day and the average energy produced by PV is 70 kWh/day. The residential sector of SCDFs is used for the evaluation of C_{ENS}. The P_{diff} is compensated by discharging/charging of BES, load curtailment, or generation curtailment. Mode switching of BES is based on the resource and load conditions. The simulation parameters and initial values to verify the proposed optimization method are shown in Table 5.1. Three cases are conducted in this research to verify the optimization method:

Table 5.1 Simulation setups.

Parameters	Setting
BES lifetime at +20 °C perm (year)	20
Battery Voltage, V_B (V)	96
C_R^{ini} (Ah)	135
P_B^{max} (kW)	16
PV Power Capacity (kWp)	20
Interest Rate, r (%)	5
ΔD	0.01
ΔC (kWh)	22.5
k_P ($/kW)	3000
k_C ($/kWh)	1000
DoD_r^{low}	0.7
DoD_r^{upp}	0.9
L_R (cycles)	3000
D_R	0.8

Case 1

In Case 1, DoD range and BES capacity were not optimized. The DoD range was fixed to be 90% and BES capacity was set at 180 Ah. The simulation results were displayed in Figs. 5.4 and 5.5.

Fig. 5.4 showed the operation of BES for day 24 of mitigating power mismatch in DC microgrid operation. BES discharged or charged to keep the system power balance. When actual DoD reached the limitations, the system activated generation curtailment or load curtailment accordingly. The load curtailment event was not observed in Fig. 5.4 since there was sufficient energy provided by BES.

126
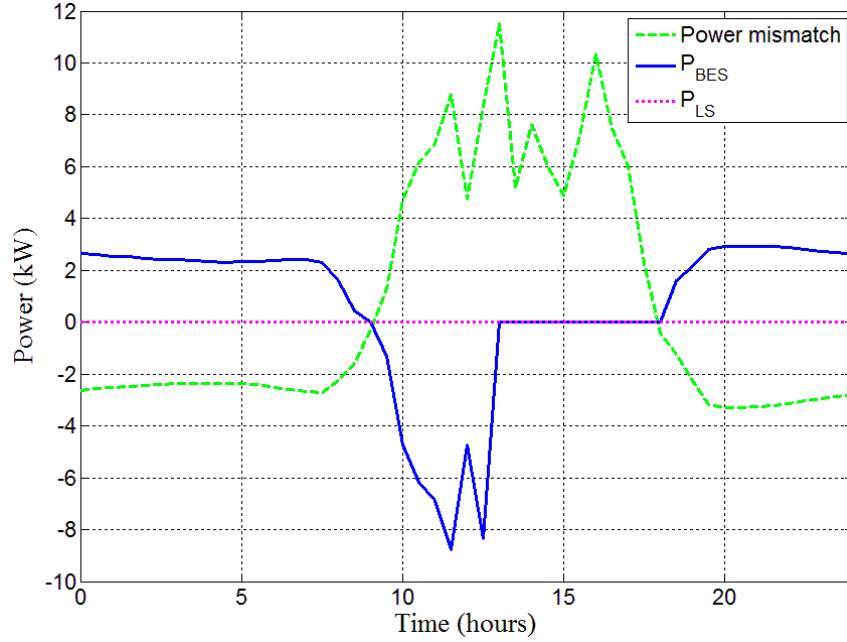
Fig. 5.4 One day BES operation without optimization.
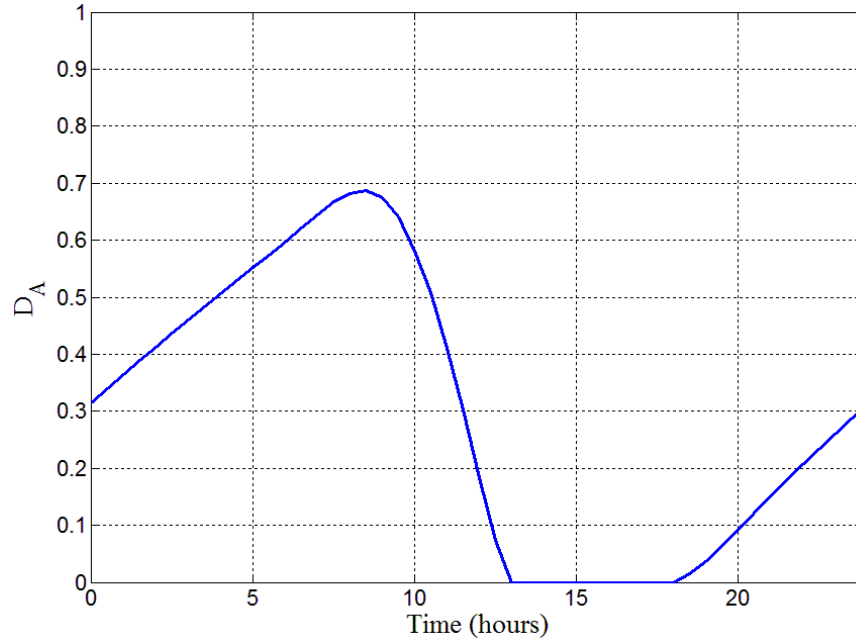
Fig. 5.5 One day respective actual DoD of BES without optimization.

The respective actual DoD of BES $D_A(t)$ for the respective day was shown in Fig. 5.5. When $D_A(t)$ reached zero at $t = 13$ hours, BES stopped charging although there was excess power from PV. The annual system operation cost and the *EBL* were $ 9,721.48 and of 17.81 years, respectively.

127

Case 2

In Case 2, the DoD_r optimization was implemented to obtain the minimum TC while C_R was remained constant during the simulation of DC microgrid operation. The setting of C_R was the same as in the previous case. The results of simulation were displayed in Figs. 5.6 and 5.7.
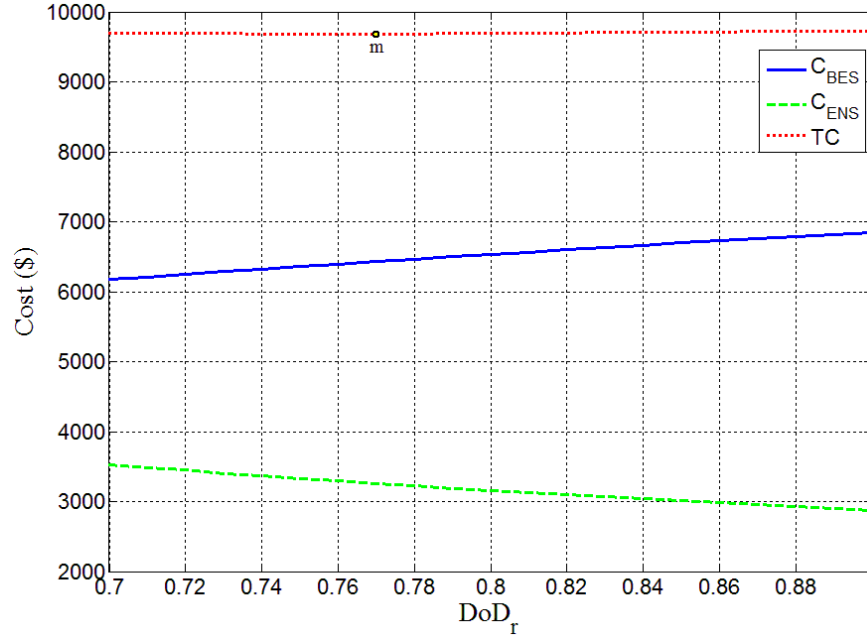
Fig. 5.6 The total system operation cost for different *DoDr*.

Fig. 5.6 showcased the relationship between the selection of DoD_r and the total system operation cost. The total system operation cost of DC microgrid changed with different selection of DoD_r. It can be seen from Fig. 5.6 that C_{BES} increased with DoD_r. This trend was occurred because with more capacity, BES charged and discharged more frequently under resource and load variations. On the other hand, C_{ENS} reduced because the load curtailment events were reduced. The trend of TC reduced while DoD_r increased until it reached the minimum point which was indicated with point "m" in Fig. 5.6. After the minimum point has reached, TC increased with DoD_r. The DoD_r^{opt} was 0.77 with the annual system operation cost of $ 9,684.48.

Selection of DoD_r was not only affecting the total system operation cost but also affecting *EBL* which was displayed in Fig. 5.7. It can be observed from Fig. 5.7

128

that *EBL* reduced with the increase of DoD_r. The *EBL* under the DoD_r^{opt} of 0.77 was 19.72 years.
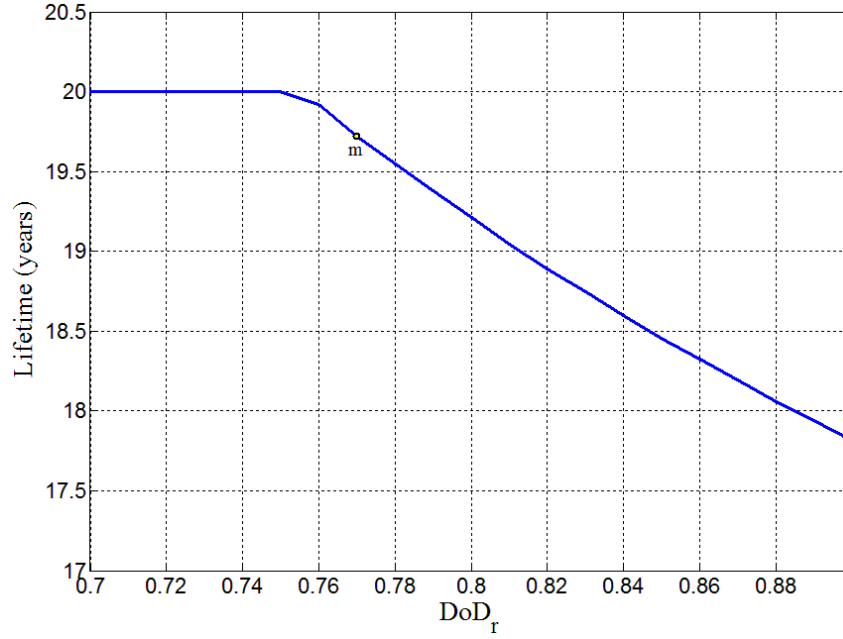
Fig. 5.7 The respective expected BES lifetime for different DoD_r.

The simulation results showed that DC microgrid operation with only DoD_r optimization delivered better result than the one without any optimization. The *TC* of Case 2 was lower by 0.38% than of Case 1. Besides, *EBL* of case 2 was longer by 10.72% than of Case 1.

Case 3

In Case 3, both DoD_r and C_R were optimized. The results of the simulation were shown in Figs. 5.8 and 5.9. Fig. 5.8 showed the relationship between *TC*, DoD_r and C_r. It can be seen from Fig. 5.8 that DoD_r decreased when C_R was increased to reach the minimum *TC* for each capacity setting. For the given generation and loading profile, the DoD_r^{opt}, C_R^{opt} and J_{DC}, were 88%, 157.5 Ah and \$ 9,639.92, respectively.

Selection of DoD_r and C_R was not only affecting the total system operation cost but also affecting *EBL* which was displayed in Fig. 5.9. It can be observed from Fig. 5.9 that using greater capacity and smaller DoD_r resulted in longer *EBL*. The *EBL*

under DoD_r of 88% and C_R of 157.5 Ah was 16.11 years which was indicated with point "m" in Fig. 5.9.
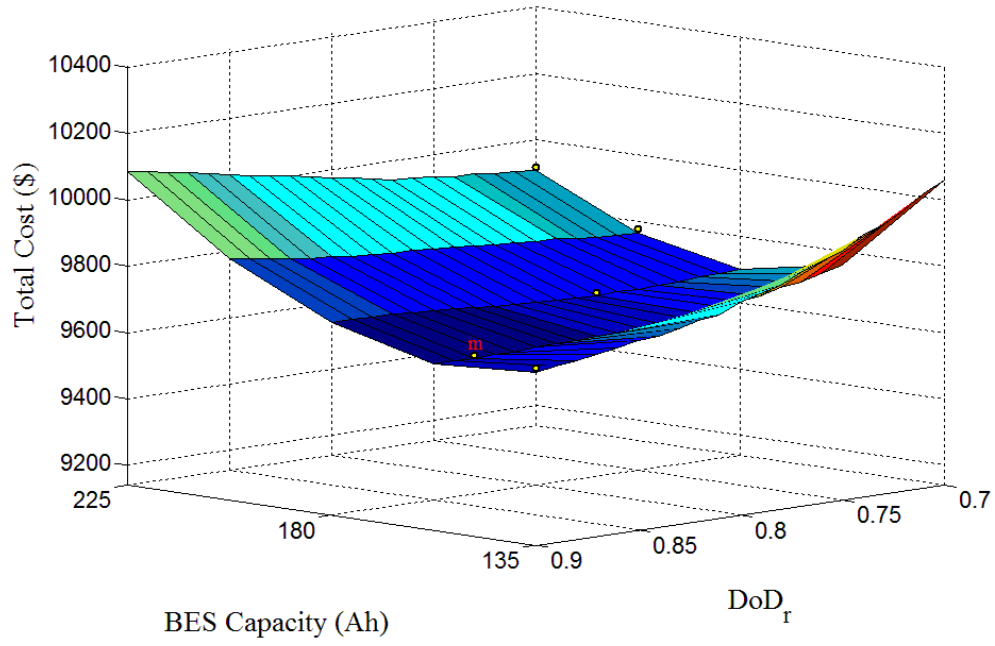
Fig. 5.8 Total system operation cost for different DoD_r and C_R.
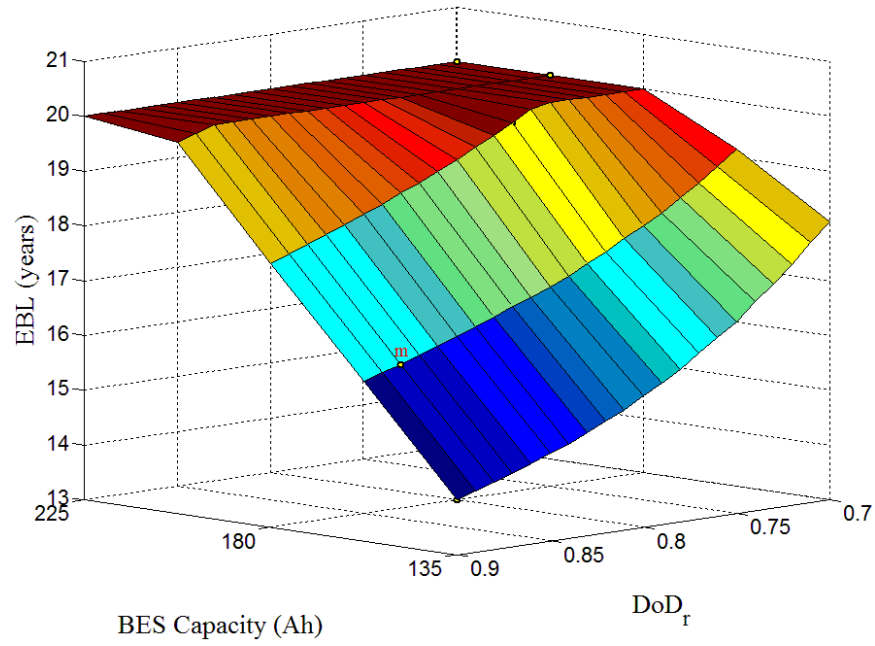
Fig. 5.9 The respective *EBL* for different DoD_r and C_R.

The simulation results demonstrated that DC microgrid operation with DoD_r and C_R optimization delivered better result in minimum TC than DC microgrid operation with only DoD_r optimization. The TC of Case 3 was lower by 0.46% than of Case 2. However, EBL of Case 2 was longer by 22.41% than of Case 3. This result occurred because in Case 3 the selected C_R was smaller while the selected DoD_r was larger compared to Case 2. This configuration caused more frequent discharge/charge events which decreased EBL.

5.5   Conclusion

Since the price of BES is of high cost, selection of BES capacity should be optimized to reduce system cost. In this report, a method is proposed to select depth of discharge range and capacity under the minimum system operation cost. The system operation cost including BES lifetime degradation cost and cost of energy not supplied were taken into consideration. The cost of BES lifetime degradation was derived from replacement cost and the expected BES lifetime while cost of energy not supplied is obtained using the sector customer damage functions. The DoD range and BES capacity are selected under the minimum system operation cost.

The proposed method has been investigated and implemented to a DC microgrid operation. MATLAB simulation has been carried out and the simulation results clearly showed the importance of selection of BES DoD range and capacity in a microgrid. Both DoD range and capacity directly affect the total system operation cost and the estimated BES lifetime. The proposed method is able to achieve J_{DC} at DoD_r^{opt} and C_R^{opt}.

Chapter VI

Real-Time Economic Dispatch of
DC Microgrids

6.1   Economic Dispatch of DC Microgrids

Many methods have been proposed in economic dispatch in DC microgrids. To ensure minimized system operation cost, distributed economic dispatch has been considered [57, 178, 179]. Droop control with the modification in droop coefficient based on generation cost of each component has been applied in those works. The economic dispatch is realized autonomously based on component's generation cost. The studies have successfully shown the implementation of efficient economic dispatch while still maintained the simplicity of the control method. However, those studies have only included distributed generation components, while ignoring others such as energy storages. In addition, distributed economic dispatch has main drawbacks which are the existence of system bus voltage variations in DC microgrids.

Multi-objective optimization has also been implemented in economic dispatch of microgrids [119, 180-182]. Authors in [180] has used the weighted sum and the ε–constrained methods to solve the multi-objective problem. While fuzzy logic and pareto-optimal have been implemented in work [119] and [181], respectively. The simulation results have demonstrated the effectiveness of the control method. However, there were some drawbacks in computational time and resources since the control method required a complicated calculation which   required up to 15 minutes to obtain optimization results for each iteration [182]. Thus, those control methods are not suitable for real-time application. Real-time economic dispatch with 5 minutes iteration time implementing Lyapunov optimization control method has been investigated [183]. However, the time resolution of 5 minutes is not suitable for real-time operation where the changes in power balance can happen in order of seconds or even smaller than that. Other than that, in most studies

marginal cost of each component was not considered. Besides, marginal cost adoption are able to simplify the optimization of the system operation cost [184].

Economic dispatch for DC microrids has been discussed in Section 3.1.2. This chapter is the extension work of what has been done in that section with more detail formulation. System units prioritization based on marginal cost for real-time power dispatch in microgrids is proposed. Marginal costs of diesel generator, BES, utility grid and interruptible load are derived. BES actual DoD and discharging rate are considered to formulate a precise BES cost model. Besides, loads are also considered as dispatchable energy assets and the correspondent marginal cost is formulated based on the customer interruption cost. The marginal costs of all system units' are compared. Those with lower marginal costs are prioritized higher and are to be dispatched first. The proposed method is implemented for real-time power dispatch in a lab-scale DC microgrid based on multi-level EMS with time resolution of 1 second.

6.2   Marginal Costs of System Units

6.2.1   Marginal Cost of Distributed Generator

The generation cost of a fossil-fueled distributed generator which in this case is diesel generator (DG) depends on the price of fuel, power rating, *etc.* [185]. The cost function of DGi for time *t* is expressed as.

$$C_{Gi}(t) = a_i + b_i P_{Gi}(t) + c_i P_{Gi}^2(t) \tag{6-1}$$

where P_{Gi} is the power output of DGi. Coefficients a_i, b_i and c_i represent the fuel consumption characteristics of DGi. The marginal cost of DGi is the derivative of cost function. The marginal cost of DGi for time *t* is expressed as.

$$MC_{Gi}(t) = \frac{dC_{Gi}(t)}{dP_{Gi}(t)} = b_i + 2c_i P_{Gi}(t) \tag{6-2}$$

DG power output is assumed to be fixed during time *t*.

The order of DG cost function is reduced to linear function. Thus, the computational process for DG utilization can be simplified. Marginal cost of DGi is proportional to P_{Gi}.

6.2.2 Marginal Cost of BES

Marginal cost of BES formulation follows that has been elaborated in Section 3.1.2. Therefore, marginal cost of BESi at discharging stage at time t is formulated as.

$$MC_{Bi}(t) = \left(\frac{D_{Ai}(t)}{D_R}\right)^{u_0} e^{u_1\left(\frac{D_{Ai}(t)}{D_R}-1\right)} \frac{K}{C_{Ai}(t)} \tag{6-3}$$

where K is a constant value, described as:

$$K = \frac{RC_i C_R}{\Gamma_R V_{Bi}(t)} \tag{6-4}$$

And the marginal cost of BESi in charging state at time t, which is a negative value can be shown as:

$$MC_{Bi}(t) = \frac{\Delta d_{eff}}{\Gamma_R} RC_i = \frac{RC_i}{\Gamma_R V_{Bi}(t)}\left(\left(\frac{D_{Ai}(t)}{D_R}\right)^{u_0} e^{u_1\left(\frac{D_{Ai}(t)}{D_R}-1\right)} - 1\right) \tag{6-5}$$

For each period, the marginal cost of BESi in charging stage, which is determined by $D_{Ai}(t)$, is assumed to be constant since the change of actual DoD can be negligible. The marginal cost of BESi in charging and discharging stage can thus be obtained.

6.2.3 Marginal Cost of Utility Grid

Cost of utility grid electricity which is incurred in every event of extracting from or injecting to the utility grid is determined by power market. The cost of utility grid for time t is expressed as.

$$C_U(t) = U(t)P_U(t)\Delta t \tag{6-6}$$

where $U(t)$ and $P_U(t)$ are utility tariff and utility power, respectively.

The marginal cost of utility grid is the first derivative of (6-6) with respect to cumulative energy. Thus, the marginal cost function of utility grid electricity for time t is expressed as.

$$MC_U(t) = U(t) \qquad (6\text{-}7)$$

The positive utility tariff denotes that the microgrid is buying electricity from utility grid while the negative value denotes that the microgrid is selling electricity to utility grid.

6.2.4 Marginal Cost of Interruptible Load

In a deregulated market, system loads can be modeled as an interruptible load to enhance system flexibility [89]. In the occasion when the total generation is a lesser amount of the total load consumption, electricity supply to some loads has to be curtailed. The load curtailment is performed based on the criticality criterion of loads in the system, *e.g.*, non-critical load to be curtailed first. Most of the time, load curtailment event causes some inconveniences to customers. Customer interruption cost (*CIC*) which is the function of load curtailment duration will be incurred in the event of load curtailment to compensate customers' inconveniences. That function is adopted from the sector customer damage functions (SCDFs) obtained from the postal surveys conducted by the University of Saskatchewan [118, 127].

The marginal cost of interruptible load based on customer interruption cost for load curtailment power of interruptible Loadi $P_{LCi}(t)$ for time t is expressed as:

$$MC_{Li}(t) = CIC(\Delta T_{LCi}) \cdot P_{LCi}(t) \qquad (6\text{-}8)$$

where ΔT_{lc} is the duration time of the interruption. The marginal cost of energy not supplied depends on the load curtailment power and ΔT_{lc}. In the real-time implementation, ΔT_{lc} is fixed at a certain value, thus $MC_{Li}(t)$ is linearly proportional with $P_{LCi}(t)$.

6.3   Marginal Costs Comparison Based Economic Dispatch

Economic dispatch is implemented to maintain the power balance while minimizing the system operation cost in real-time. The power balance in a microgrid at time t consisting components of BESs, utility grid, DGs, RESs, and loads is expressed as:

$$P_{Bs}(t)+P_U(t)+P_{Gs}(t)+P_{LCs}(t)=P_{Loads}(t)-P_{RESs}(t)=P_{net}(t) \tag{6-9}$$

where $P_{Bs}(t)$, $P_U(t)$, $P_{Gs}(t)$, $P_{LCs}(t)$, $P_{RESs}(t)$, $P_{Loads}(t)$ and $P_{net}(t)$ are power output of battery energy storages, power output of utility grid, power output of diesel generators, interruptible loads power, power output of renewable energy sources, system loads power consumption and system net power, respectively.

The objective of economic dispatch is to minimize the operation cost of microgrids with considering system constraints which include:

- *Microgrid power balance*

The power balance of the microgrid as expressed in (6-9) has to be retained during system operation.

- *BESs charging/discharging limits*

$$P_{Bs}^{\min} \leq P_{Bs}(t) \leq P_{Bs}^{\max} \tag{6-10}$$

where $P_{Bs}^{\min}$ and $P_{Bs}^{\max}$ are the maximum charging and discharging power of BESs, respectively.

- *Actual DoD limits*

$$D_{\min} \leq D_A(t) \leq D_{\max} \tag{6-11}$$

where D_{min} and D_{max} are the DoD lower limit to protect BES from over-charged and the DoD upper limit to protect BES from being over-discharged, respectively.

- *Utility power limits*

$$P_U^{\min} \leq P_U(t) \leq P_U^{\max} \tag{6-12}$$

where $P_U^{\min}$ and $P_U^{\max}$ are the maximum injecting and extracting power to and from the utility grid, respectively. The utility power is limited by the converter which interlinks the utility grid and the microgrid.

- *DGs power limit*

$$0 \le P_{Gs}(t) \le P_{Gs}^{\max} \tag{6-13}$$

where $P_{Gs}^{\max}$ is the maximum power rating of DGs.
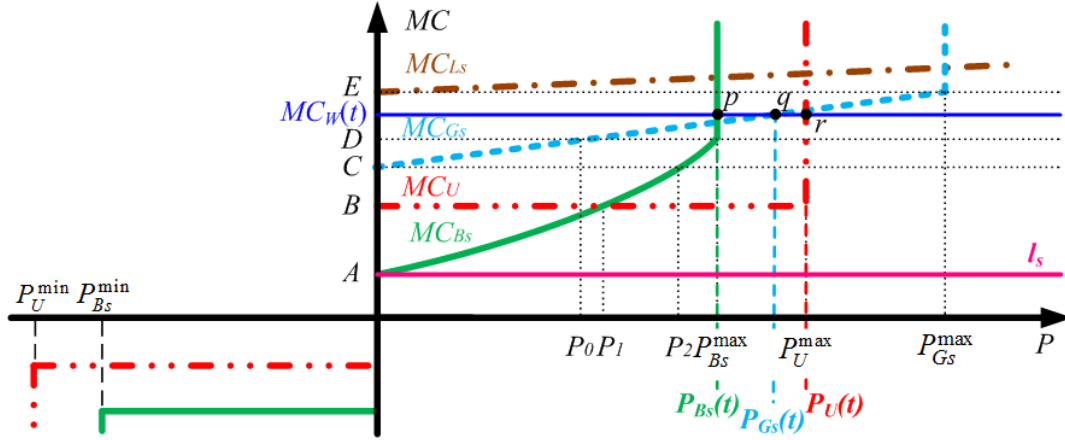
Fig. 6.1 Marginal cost vs. output power of system units.

Marginal cost of DGs, BESs utility grid, and interruptible loads are compared as can be seen in Fig. 6.1. Prioritization of system unit utilization is established based on the marginal cost of system units. System unit with the lowest marginal cost is assigned to dispatch power with the highest priority. RESs are normally scheduled to operate in maximum power point tracking (MPPT) mode to maximize the utilization. DGs only operate with positive power output and the marginal cost is determined by (6-7). The marginal cost of utility grid is determined by the real-time electricity price. When the microgrid sells the excess electricity, the marginal cost $MC_U(t)$ is indicated with the government incentives for energy injection into the utility grid, whose magnitude is usually lower than that of electricity price. Normally, marginal cost of localized DGs generation is higher than the electricity price and BES. Therefore, the utilization priority of DGs is lower than BES and utility grid. Because the marginal cost of interruptible loads is the highest, load curtailment activation has the lowest priority. The marginal cost of BESs is

affected by $D_A(t)$ and the magnitude of marginal cost is positively related to the power output in discharging stage. In charging stage, marginal cost of BESs is affected by $D_A(t)$ when BES starts to charge which can be observed in (6-5).
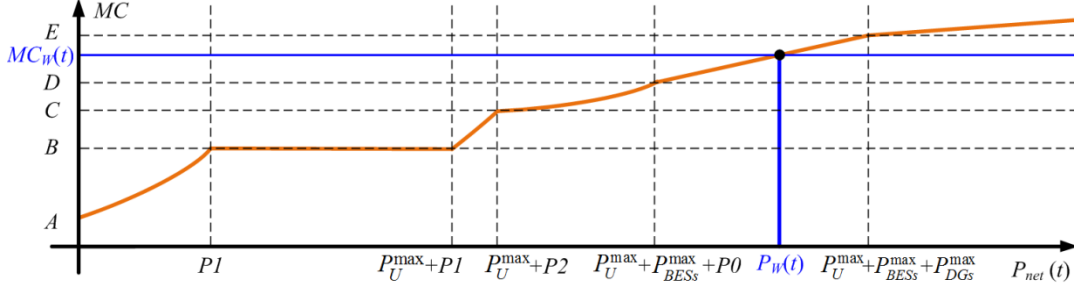
Fig. 6.2 System marginal cost for different system net power.

Fig. 6.1 can be elaborated to obtain the relationship between system marginal cost and system net power with the assistance of line l_s. The line l_s represents system marginal cost. The ordinate of the cross point between line l_s and system unit's marginal cost curve denotes the system marginal cost. When line l_s is shifted upward from the beginning and all cross points are traced, the relationship between system marginal cost and system net power for every points can be obtained. The system marginal cost for different system net power is shown in Fig. 6.2. When the system net power of $P_W(t)$ is resulted from the difference of RESs generation and loading profile, the correspondent system marginal cost is $MC_W(t)$. The power sharing among system units with marginal cost of $MC_W(t)$ can be shown intuitively in Fig. 6.1. The $MC_W(t)$ crossovers marginal cost curve of BESs, DGs and utility grid at point p, q and r, respectively. With P_{net} of $P_W(t)$, the BESs will dispatch power of $P_{Bs}(t)$, DGs will dispatch power of $P_{Gs}(t)$ and utility grid will dispatch power of $P_U(t)$.

Referring to Figs. 6.1 and 6.2, the power scheduling of BESs, utility grid, DGs and activation of load curtailment based on comparison of system units' marginal costs are:

• *BESs power dispatch*

Charging mode:

138

$$P_{Bs}(t) = \begin{cases} P_{net}(t) & (P_{Bs}^{min} < P_{net}(t) \le 0) \\ P_{Bs}^{min} & (P_{net}(t) \le P_{Bs}^{min}) \end{cases} \tag{6-14}$$

Discharging mode:

$$P_{Bs}(t) = \begin{cases} P_{net}(t) & (0 < P_{net}(t) \le P_1) \\ P_1 & (P_1 < P_{net}(t) \le P_U^{max} + P_1) \\ P_{net}(t) - P_U^{max} & (P_U^{max} + P_1 < P_{net}(t) \le P_U^{max} + P_2) \\ P_{net}(t) - P_U^{max} - P_{Gs} & (P_U^{max} + P_2 < P_{net}(t) \le P_U^{max} + P_{Bs}^{max} + P_0) \\ P_{Bs}^{max} & (P_U^{max} + P_{Bs}^{max} + P_0 < P_{net}(t)) \end{cases} \tag{6-15}$$

- *Utility grid power dispatch*

Power extracting mode:

$$P_U(t) = \begin{cases} 0 & (P_{net}(t) \le P_1) \\ P_{net} - P_1 & (P_1 < P_{net}(t) \le P_U^{max} + P_1) \\ P_U^{max} & (P_U^{max} + P_1 < P_{net}(t)) \end{cases} \tag{6-16}$$

Power injecting mode:

$$P_U(t) = \begin{cases} P_{net}(t) - P_{Bs}^{min} & (P_U^{min} + P_{Bs}^{min} < P_{net}(t) \le P_{Bs}^{min}) \\ P_U^{min} & (P_{net}(t) \le P_U^{min} + P_{Bs}^{min}) \end{cases} \tag{6-17}$$

- *DGs power dispatch*

$$P_{Gs}(t) = \begin{cases} 0 & (P_{net}(t) \le P_U^{max} + P_2) \\ P_{net}(t) - P_U^{max} - P_{Bs} & (P_U^{max} + P_2 < P_{net}(t) \le P_U^{max} + P_{Bs}^{max} + P_0) \\ P_{net}(t) - P_U^{max} - P_{Bs}^{max} & (P_U^{max} + P_{Bs}^{max} + P_0 < P_{net}(t) \le m) \\ P_{Gs}^{max} & (m < P_{net}(t)) \end{cases} \tag{6-18}$$

where $m = P_U^{max} + P_{Bs}^{max} + P_{Gs}^{max}$

- *Load curtailment activation*

In case the total generation is not sufficient to provide load consumption, load curtailment is activated.

$$P_{LCs}(t) = \begin{cases} 0 & (P_{net}(t) \le P_U^{max} + P_{Bs}^{max} + P_{Gs}^{max}) \\ P_{net}(t) - P_U^{max} + P_{Bs}^{max} + P_{Gs}^{max} & (P_U^{max} + P_{Bs}^{max} + P_{Gs}^{max} < P_{net}(t)) \end{cases} \tag{6-19}$$

139

With the generated power references as described in (6-14) – (6-19), microgrid power balance is ensured during the operation. Comparison of marginal cost is carried out in the power scheduling to determine the utilization priority of system units. Not only that the system power balance is ensured but minimum system operation cost is also achieved by implementing this method. The main advantage of the proposed economic dispatch by comparing the marginal costs of BESs, utility grid, DGs and interruptible loads is the simplicity which results in faster computation and higher time resolution for optimization. Therefore, it can be implemented in the real-time environment.

6.4 Experimental Verifications

A lab-scale DC microgrid is established as can be seen in Fig. 6.3 to verify the proposed economic dispatch based on marginal cost comparison. Eight circuit panels which can be connected to various energy sources, battery energy storages and loads are installed in loop configuration to establish a DC system bus. DC meters with data logging capability of bus voltage, power flow, *etc.* are mounted at each circuit panel outlet to monitor system operation statuses. The time-step of SCADA system is set to be 1 s.
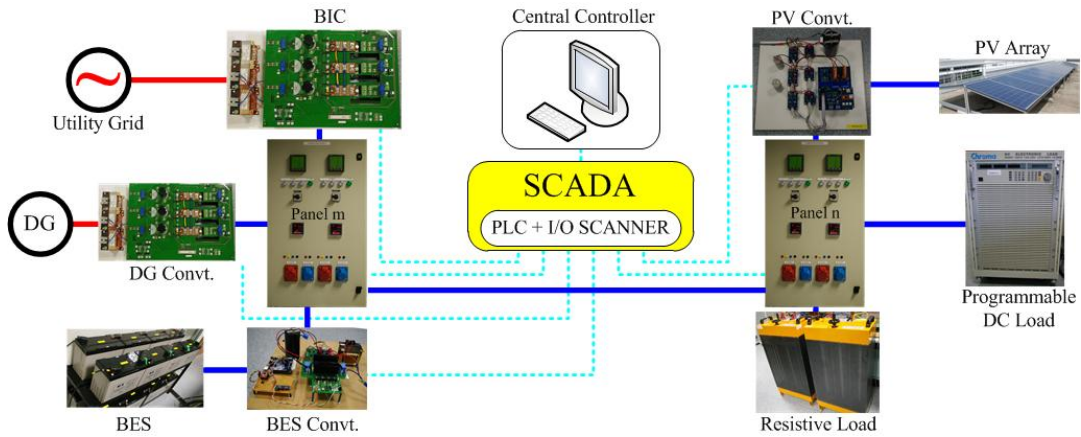
Fig. 6.3 Schematic diagram of a lab-scale DC microgrid.

The proposed method is implemented with multi-level EMS as described in Section 3.1. Three layers of control are configured in this multi-level EMS. Distributed EMS for system net power decomposition and components power

sharing is operated as the primary control. Utility grid, DG and BES operate in VRM with droop control. Bus voltage restoration is implemented in secondary control to eliminate the voltage deviation. Economic dispatch based on marginal costs comparison is employed in tertiary control to provide power reference economically to each component.

Solar PV arrays are integrated as the renewable energy sources. Programmable DC power supply is used to simulate the DG with AC/DC rectifier. Lead acid BES, DG and utility grid are integrated as energy buffer to compensate the imbalance power during DC microgrid operation. Both resistive load bank and Chroma programmable load are implemented to generate different loading profiles. The nominal DC bus voltage selection has followed the standard published by the REbus Alliance to be 380 V [7]. Specifications of experimental setups are presented in Table. 6.1. Three experiment cases have been conducted to verify the effectiveness the proposed method.

Table 6.1 Experimental setups.

Parameters	Unit	Settings
Nominal bus voltage	V	380
PV power capacity	kWp	2
BES power capacity	kW	1.5
DG power capacity	kW	2
Utility grid power capacity	kW	2
Utility tariff	$/kWh	0.118
RC	$	18,088.40
L_R	cycles	3000
D_R	-	0.8
C_R	Ah	137
D_A	-	0.5
a	$	2.594
b	$/kWh	0.271
c	$/kWh^2	0.0005
Resistive load	Ω	580
Δt	s	1

Case 1

Case 1 demonstrated DC microgrid operation based on conventional method in islanded mode. Experimental results, comprising PV generation, load consumption, DG power output, BES power output and system bus voltage, were as displayed in Fig. 6.4. Power dispatch in DC microgrid conventionally has been implemented

141

based on proportional power rating of components. The shared power was inversely proportional to the droop coefficient assigned. Islanded DC microgrid with integration of a PV, a BES, a DG and loads was established. PV was configured to operate in MPPT mode while BES and DG were operate in VRM with droop control. PV power output range of 0.81 - 1.24 kW was obtained as can be seen in Fig. 6.4. The average PV power output was 0.96 kW. The droop coefficients of BES and DG were obtained based on the voltage variation range and power capacities to be 6.67 and 5 V/kW, respectively. The resistive load consumed 240 W and the programmable load range was 0 - 3 kW.
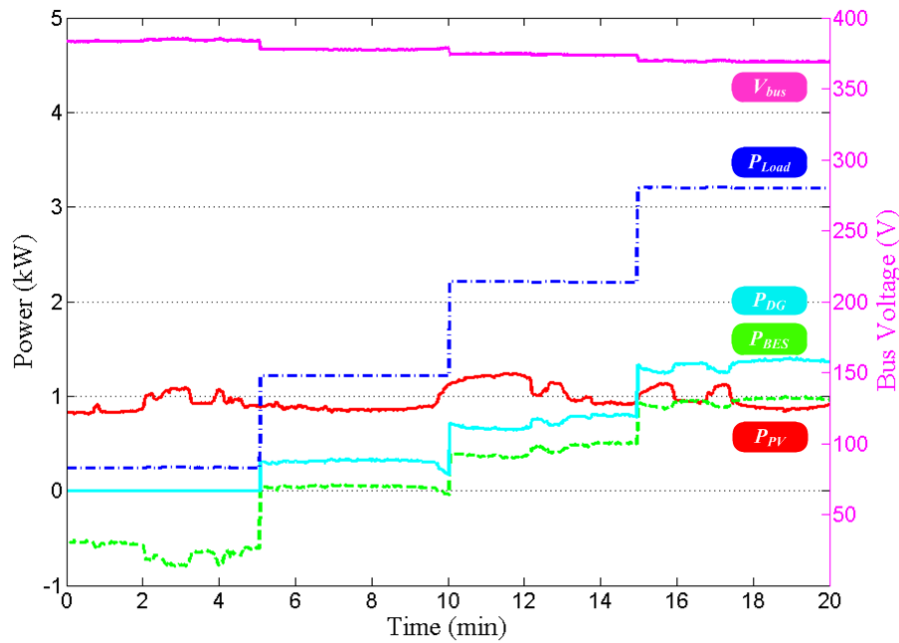
Fig. 6.4 Case 1 experimental results.

The islanded DC microgrid was operated for the duration of 20 minutes. Initially, only the resistive load was connected resulting in system net power P_{net} of -0.6 kW which meant that the generation was larger than load consumption. Thus, BES operated in charging stage to transfer all the excess power to charge BES while DG was not activated. When programmable load was increased to 1 kW at 5 min, Pnet increased to 0.35 kW. As a result, DG was activated and BES changed to discharging stage to maintain system power balance. Later on, the programmable load was increased again to 2 kW and 3 kW at 10 min and 15 min, respectively.

142

The DG and BES dispatch power proportionally based on their rated capacity i.e. 2 kW and 1.5 kW, respectively.

Bus voltage deviations can be observed since distributed control was implemented in this case study. Even though the marginal cost of DG is much higher than BES, in conventional method the power dispatch was performed proportionally based on power rating of its component which caused inefficiency in system operating cost. Marginal costs incurred with this method were $ 0.1093 and $ 0.0873 for DG and BES respectively. The total cost for this case study was $ 0.1966.

Case 2

Economic dispatch in DC microgrid based on marginal costs comparison was implemented in case 2. The proposed method was conducted in islanded DC microgrid with the same parameter and loading profiles as in case 1. Experiment results were displayed in Fig. 6.5.
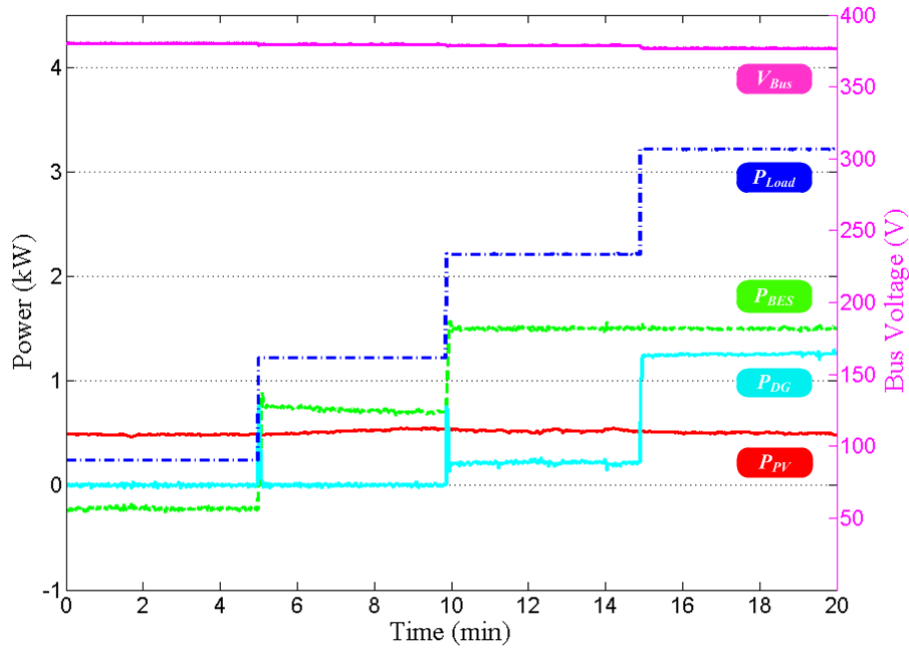
Fig. 6.5 Case 2 experimental results

Initially, negative P_{net} of -0.25 kW was resulted. Thus, same as in Case 1, BES operated in charging stage while DG was not activated. When programmable load was increased to 1 kW at 5 min P_{net} also increased to 0.7 kW. Since the marginal

cost of DG is higher than BES, DG was still not activated while BES changed to discharging stage to maintain system power balance. The programmable load was then increased again to 2 kW at 10 min and P_{net} increased to 1.7 kW. This configuration caused the activation of DG since BES has reached the maximum power rating of 1.5 kW. Thus, the difference between P_{net} and BES discharging power of 0.2 kW was supplied by DG. At 15 min, the programmable load was further increased to 3 kW and Pnet of 2.72 kW was resulted. Power dispatch of BES was still remained the same as the previous i.e. 1.5 kW and the difference between Pnet and BES discharging power of 1.22 kW was all covered by DG. The voltage variations can be reduced significantly since the multi-level EMS based control was implemented. During load transition at 5 min and 10 min, inrush power can be observed. These events happened because of the response delay of second and tertiary control in multi-level EMS.

Marginal costs incurred in this case were $ 0.1091 and $ 0.0885 for DG and BES, respectively. The total cost for this case study was $ 0.1976. PV power output should also be considered to compare the results between Case 1 and Case 2. The average PV power output for Case 2 was 0.506 kW which is lower by 0.454 kW than of case 1 which is 0.96 kW. However, the total cost of Case 2 will be much lower than those of Case 1 if the same PV power output applies. System operating cost can be reduced with the implementation of the proposed economic dispatch.

Case 3:

Economic dispatch based on marginal costs comparison was implemented in grid-tied DC microgrid for Case 3. The programmable load range was 1 - 4 kW. Experiment results are shown in Fig. 6.6.

At the start, resistive load and 1 kW programmable load were activated. Average PV power output was 0.615 kW. In this configuration the P_{net} of 0.64 kW was compensated by BES since BES has the lowest marginal cost. When the programmable load was increased to 2 kW at 10 min, P_{net} increased to 1.6 kW. Since the cross-point between marginal cost of BES and utility grid, referred to Fig.

2, was at 1.2 kW. BES supplied the P_{net} of 1.2 kW while the rest P_{net} of 0.4 kW was supplied by utility grid. At 15 min the programmable load was further increased to 3 kW resulted in P_{net} of 2.6 kW. The power sharing between BES and utility grid was still the same as the previous loading profile. Load power of 1.2 kW was supplied by BES while the rest of 1.4 kW was supplied by utility grid. Later on, programmable load was increased to 4 kW resulted in P_{net} of 3.6 kW. BES and utility grid reached the maximum power rating which was 1.5 kW and 2 kW, respectively, hence DG was activated to compensate the remaining P_{net} of 0.1 kW. DG was activated the last because of its marginal cost which was the highest compared to BES and utility grid.
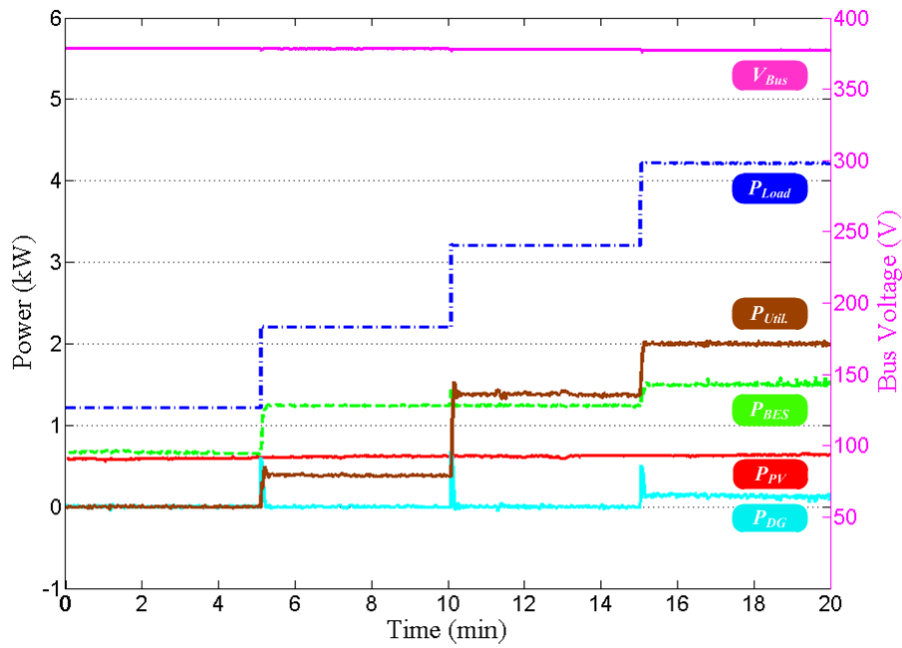
Fig. 6.6 Case 3 experimental results.

The experimental results of Case 3 have successfully demonstrated that the proposed method in DC microgrid operation can also be implemented in grid-tied mode and the result was as effective as it was in islanded mode. The prioritization of components utilization has been made based on the marginal cost. Component with the lowest marginal cost was activated first while component with higher marginal cost is activated later.

6.5   Conclusion

This chapter extends the work of what has been done in Section 3.1.2. More detail formulations on the marginal costs of system units have been realized. System units prioritization based on marginal cost for real-time power dispatch in microgrids has been proposed and implemented for DC microgrid operation. Marginal costs for BES, utility grid, DG and interruptible load have been derived.

Real-time economic dispatch based on marginal cost comparison has been proposed. The proposed method is able to do power scheduling prioritization intuitively based on marginal cost. The direct comparison of components' marginal cost simplifies the economic dispatch, thus it is suitable for real-time implementation. The effectiveness of the proposed method has been verified with a lab-scale multi-level EMS based DC microgrid with time resolution of 1 second.

Chapter VII

Conclusion and Future Works

7.1 Conclusion

Along with the increasing penetration of RESs, energy storages and DC-inherent loads in today's power systems, DC microgrids are gaining popularity because of the advantages to cope with the power conversion ineffectiveness and to reduce the carbon emission to the environment.

System stability of DC microgrids which is affected by system power balance and bus voltage is a key component that determines the quality of DC microgrid operation. Moreover, to deploy a cost-effective DC microgrid, parameters like system operation cost, battery lifetime, load management, *etc*. should also be considered. Therefore, to integrate all system units such that DC microgrid operation can be optimized, EMS strategy is implemented. Several EMS strategies for DC microgrids have been proposed, elaborated and implemented in this report.

Distributed EMS depends on local bus voltage as global indicator of system power balance hence it does not require communication links. Two types of distributed EMS strategies for DC microgrids have been proposed including multiple modes distributed EMS and advanced multiple-slack-terminal distributed EMS. In multiple modes distributed EMS, system bus voltage is partitioned into several regions and system units are prioritized based on their marginal utilization costs. The comparison of the local bus voltage with the threshold voltages determines the scheduling of system units' operating modes. In advanced multiple-slack-terminal distributed EMS, droop control is implemented to ensure seamless system bus voltage variation during the transitions of bus voltage regions. Besides, active power sharing among the multiple slack terminals can be realized effectively. Although distributed EMS is able to retain the system power balance effectively and autonomously, there are main drawbacks that are impossible to be eliminated

by distributed EMS *i.e*. steady state bus voltage deviations, power sharing error and inability in solving systematic optimization.

Therefore, multi-level based EMS with multiple slack terminals has been proposed to mitigate the main drawbacks of distributed EMS. It consists of primary control, secondary and tertiary control. Distributed EMS is applied in primary control. Bus voltage restoration is implemented in secondary control to bus voltage deviations so that system power quality can be enhanced. In tertiary control, power sharing compensation is applied to eliminate the error in power tracking. In case of communication failure, system operation can still be retained with primary control to ensure system reliability. Multi-level EMS also has been applied for the transition operation of DC microgrid between islanded and grid-tied mode. Another application of multi-level EMS is on hybrid AC/DC microgrid. Applying multi-level EMS in hybrid AC/DC microgrid ensures system power balance while enhancing the reliability.

Utilization of hybrid energy storages is turned out to be an effective and economic solution by applying the most of different ESs characteristics. EMS strategies for HESS coordination have been proposed in this report. Two types of strategy have been described including distributed and multi-level EMS of HESS. Distributed EMS realizes system net power decomposition and ESs power dispatch autonomously and effectively. However, distributed EMS has the main drawbacks such as degraded power quality and control accuracy. Therefore, multi-level EMS of HESS consisted of primary, secondary and tertiary controls, is proposed to improve system control accuracy and reliability. In primary control, multiple-slack-terminal distributed EMS of HESS, in which all ESs operate in VRM, is implemented. In secondary control, bus voltage restoration and power sharing compensation are implemented to eliminate the voltage deviation and power sharing errors, respectively. Moreover, in tertiary control, autonomous SoC recovery is used to limit the SoC variation of the ESs with high ramp rate. In case of communication failure, system operation can still be retained with primary control.

148

Battery energy storages play an important role in mitigating system power imbalance in DC microgrids due to RESs intermittency and sudden load change. However, the price of BES is of high cost, selection of BES capacity should thus be optimized to reduce system cost. A method has been proposed in this report to select depth of discharge range and capacity under the minimum system operation cost. The system operation cost including BES lifetime degradation cost and cost of energy not supplied were taken into consideration. The DoD range and BES capacity are selected under the minimum system operation cost.

More detail formulations on the marginal costs of system units have been realized. Real-time economic dispatch based on marginal cost comparison has been proposed and implemented for DC microgrid operation. The proposed method is able to do power scheduling prioritization intuitively based on marginal cost. The direct comparison of components' marginal cost simplifies the economic dispatch, thus it is suitable for real-time implementation.

The proposed methods have been verified in a lab-scale DC microgrid with integration of rooftop solar PV panels, various energy storages, loads and energy sources which is installed in Water and Energy Research Laboratory, Nanyang Technological University, Singapore. Supervisory control and data acquisition (SCADA) system has been embedded in the central controller for centralized coordination. Distributed EMS, multi-level EMS, islanding and reconnection procedures for system transitions between islanded and grid-tied modes, multi-level EMS of HESS have been tested with the lab-scale DC microgrid in different loading profiles.

7.2   Future Works

The main focus of this report is EMS strategy of DC microgrid with the integration on RESs and ESs. However, some related research topics should be further investigated to complete and enhance the implementation of the EMS strategy such as:

- Reliability of DC microgrids

In actual implementation, the quantitative reliability analysis of DC microgrid system is necessary to improve the performance of DC microgrids. Reliability analysis of DC microgrids can start from the small components like capacitors, power switches, sensors, *etc*. to the larger component like power electronic converters and ends with the reliability analysis in system level.

- Protection of DC microgrids

Protection of DC microgrids is very important to ensure the safety not only for the system but also for the end-user. Since the mechanisms of DC and AC protections are different and the standard of DC microgrid is still lacking, more research on this topic should be taken into consideration.

- EMS of hybrid AC/DC microgrids

EMS of hybrid AC/DC microgrids has been proposed and simulated in this report. However, the experimental verifications have to be conducted in real situations. With experimental verifications, some physical problems that are not shown in simulation, can be observed.

- EMS of multiple microgrids

EMS of multiple microgrids should be investigated since in the future more and more DC microgrids will be established. So, EMS of multiple microgrids will be required to manage the power flow among DC microgrids.

List of Publications

Journal Papers:

1. Setyawan, L.; Wang, P.; Xiao, J., "Marginal Cost Based System Units Prioritization for Real-time Power Dispatch in Microgrids", in *Smart Grid, IEEE Transactions on*, **submitted**.

2. Setyawan, L.; Wang, P.; Xiao, J., "Optimal Depth-of-Discharge Range and Capacity Settings for Battery Energy Storage in Microgrid Operation", in *Energy Conversion, IEEE Transactions on*, **submitted**.

3. Xiao, J.; Wang, P.; Setyawan, L.; Xu, Q., "Multi-Level Energy Management System for Real-Time Scheduling of DC Microgrids with Multiple Slack Terminals," in *Energy Conversion, IEEE Transactions on*, vol.PP, no.99, pp.1-9, 2015.

4. Xiao, J.; Setyawan, L.; Wang, P.; Jin, C., "Power-Capacity-Based Bus-Voltage Region Partition and Online Droop Coefficient Tuning for Real-Time Operation of DC Microgrids," in *Energy Conversion, IEEE Transactions on*, vol.PP, no.99, pp.1-10, 2015.

5. Xiao, J.; Wang, P.; Setyawan, L., "Implementation of Multiple-Slack-Terminal DC Microgrids for Smooth Transitions between Grid-tied and Islanded States," in *Smart Grid, IEEE Transactions on*, vol.PP, no.99, pp.1-1, 2015.

6. Xiao, J.; Wang, P.; Setyawan, L., "Multilevel Energy Management System for Hybridization of Energy Storages in DC Microgrids," in *Smart Grid, IEEE Transactions on*, vol.PP, no.99, pp.1-1, 2015.

7. Xiao, J.; Wang, P.; Setyawan, L., "Hierarchical Control of Hybrid Energy Storage System in DC Microgrids," in *Industrial Electronics, IEEE Transactions on*, vol.62, no.8, pp.4915-4924, Aug. 2015.

Conference Papers:

1. Xu, Q.; Hu, X.; Wang, P.; Xiao, J.; Setyawan, L., "Design and Stability Analysis for an Autonomous DC Microgrid with Constant Power Load," in *Annual IEEE Applied Power Electronics Conference and Exposition (APEC)*, 2016, **accepted**.

2. Xiao, J.; Wang, P.; Setyawan, L.; Jin, C.; Choo, F. H., "Energy management system for control of hybrid AC/DC microgrids," in *Industrial Electronics and Applications (ICIEA), 2015 IEEE 10th Conference on*, vol., no., pp.778-783, 15-17 June 2015.

3. Setyawan, L.; Xiao, J.; Wang, P.; Choo, F. H., "Hybridization of energy storages with different ramp rates in DC microgrids," in *Industrial Technology (ICIT), 2015 IEEE International Conference on*, vol., no., pp.1317-1322, 17-19 March 2015.

4. Wang, P.; Xiao, J.; Setyawan, L.; Choo, F. H., "Energy management system (EMS) for real-time operation of DC microgrids with multiple slack terminals," in *Innovative Smart Grid Technologies Conference Europe (ISGT-Europe), 2014 IEEE PES*, vol., no., pp.1-6, 12-15 Oct. 2014.

5. Setyawan, L.; Wang, P.; Xiao, J., "Implementation of sliding mode control in DC microgrids," in *Industrial Electronics and Applications (ICIEA), 2014 IEEE 9th Conference on*, vol., no., pp.578-583, 9-11 June 2014.

6. Wang, P.; Xiao, J.; Setyawan, L.; Jin, C.; Choo, F. H., "Hierarchical control of active hybrid energy storage system (HESS) in DC microgrids," in *Industrial Electronics and Applications (ICIEA), 2014 IEEE 9th Conference on*, vol., no., pp.569-574, 9-11 June 2014.

References

[1]   C. L. Sulzberger, "Triumph of AC - from Pearl Street to Niagara," *Power and Energy Magazine, IEEE,* vol. 99, pp. 64-67, 2003.

[2]   C. L. Sulzberger, "Triumph of AC. 2. The battle of the currents," *Power and Energy Magazine, IEEE,* vol. 1, pp. 70-73, 2003.

[3]   M. R. Hossain, A. M. T. Oo, and A. B. M. S. Ali, "Evolution of smart grid and some pertinent issues," in *Universities Power Engineering Conference (AUPEC), 2010 20th Australasian*, 2010, pp. 1-6.

[4]   P. Asmus, "Why Microgrids Are Moving into the Mainstream: Improving the efficiency of the larger power grid," *Electrification Magazine, IEEE,* vol. 2, pp. 12-19, 2014.

[5]   K. Ravindra, B. Kannan, and N. Ramappa, "Microgrids: A Value-Based Paradigm: The need for the redefinition of microgrids," *Electrification Magazine, IEEE,* vol. 2, pp. 20-29, 2014.

[6]   R. H. Lasseter, "MicroGrids," in *Power Engineering Society Winter Meeting, 2002. IEEE*, 2002, pp. 305-308 vol.1.

[7]   G. AlLee and W. Tschudi, "Edison Redux: 380 Vdc Brings Reliability and Efficiency to Sustainable Data Centers," *Power and Energy Magazine, IEEE,* vol. 10, pp. 50-59, 2012.

[8]   P. Savage;, R. R. Nordhaus;, and S. P.Jamieson, "DC Microgrids: Benefits and Barriers," Yale University2010.

[9]   M. A. Tavakkoli, A. Radan, and H. Hassibi, "Simulation and Analysis of a Compact Electronic Infrastructure for DC Micro-Grid: Necessity and Challenges," *Smart Grid and Renewable Energy,* vol. 3, pp. 73-82, 2012.

[10]   M. Kumar, S. N. Singh, and S. C. Srivastava, "Design and control of smart DC microgrid for integration of renewable energy sources," in *Power and Energy Society General Meeting, 2012 IEEE*, 2012, pp. 1-7.

[11]   B. M. Grainger, G. F. Reed, A. R. Sparacino, and P. T. Lewis, "Power Electronics for Grid-Scale Energy Storage," *Proceedings of the IEEE,* vol. 102, pp. 1000-1013, 2014.

[12]   G. F. Reed, "DC Technologies: Solutions to Electric Power System Advancements [Guest Editorial]," *Power and Energy Magazine, IEEE,* vol. 10, pp. 10-17, 2012.

[13]   M. Huber, A. Trippe, P. Kuhn, and T. Hamacher, "Effects of large scale EV and PV integration on power supply systems in the context of Singapore," in *Innovative Smart Grid Technologies (ISGT Europe), 2012 3rd IEEE PES International Conference and Exhibition on*, 2012, pp. 1-8.

[14]   B. T. Patterson, "DC, Come Home: DC Microgrids and the Birth of the "Enernet"," *Power and Energy Magazine, IEEE,* vol. 10, pp. 60-69, 2012.

[15]   J. V. Appen, M. Braun, T. Stetz, K. Diwold, and D. Geibel, "Time in the Sun: The Challenge of High PV Penetration in the German Electric Grid," *Power and Energy Magazine, IEEE,* vol. 11, pp. 55-64, 2013.

[16]   C. A. Hill, M. C. Such, D. Chen, J. Gonzalez, and W. M. Grady, "Battery Energy Storage for Enabling Integration of Distributed Solar Power Generation," *Smart Grid, IEEE Transactions on,* vol. 3, pp. 850-857, 2012.

[17] A. Etxeberria, I. Vechiu, S. Baudoin, H. Camblong, and J. Vinassa, "Control of a hybrid Energy Storage System using a three level neutral point clamped converter," in *IECON 2012 - 38th Annual Conference on IEEE Industrial Electronics Society*, 2012, pp. 3400-3405.

[18] H. Qian, J. Zhang, J.-S. Lai, and W. Yu, "A High-Efficiency Grid-Tie Battery Energy Storage System," *Power Electronics, IEEE Transactions on,* vol. 26, pp. 886-896, 2011.

[19] H. Zhou, T. Bhattacharya, T. Duong, T. S. T. Siew, and A. M. Khambadkone, "Composite Energy Storage System Involving Battery and Ultracapacitor With Dynamic Energy Management in Microgrid Applications," *Power Electronics, IEEE Transactions on,* vol. 26, pp. 923-930, 2011.

[20] N. Eghtedarpour and E. Farjah, "Distributed charge/discharge control of energy storages in a renewable-energy-based DC micro-grid," *Renewable Power Generation, IET,* vol. 8, pp. 45-57, 2014.

[21] R. Majumder, C. Bartzsch, P. Kohnstam, E. Fullerton, A. Finn, and W. Galli, "Magic Bus: High-Voltage DC on the New Power Transmission Highway," *Power and Energy Magazine, IEEE,* vol. 10, pp. 39-49, 2012.

[22] N. Hatziargyriou, "The Microgrids Concept," in *Microgrids:Architectures and Control*, ed: Wiley-IEEE Press, 2014, pp. 1-344.

[23] F. Katiraei, R. Iravani, N. Hatziargyriou, and A. Dimeas, "Microgrids management," *Power and Energy Magazine, IEEE,* vol. 6, pp. 54-65, 2008.

[24] D. Chen and L. Xu, "Autonomous DC Voltage Control of a DC Microgrid With Multiple Slack Terminals," *Power Systems, IEEE Transactions on,* vol. 27, pp. 1897-1905, 2012.

[25] D. Salomonsson, L. Soder, and A. Sannino, "An Adaptive Control System for a Dc Microgrid for Data Centers," in *Industry Applications Conference, 2007. 42nd IAS Annual Meeting. Conference Record of the 2007 IEEE*, 2007, pp. 2414-2421.

[26] M. Sechilariu, B. Wang, and F. Locment, "Building Integrated Photovoltaic System With Energy Storage and Smart Grid Communication," *Industrial Electronics, IEEE Transactions on,* vol. 60, pp. 1607-1618, 2013.

[27] H. Kakigano, Y. Miura, and T. Ise, "Low-Voltage Bipolar-Type DC Microgrid for Super High Quality Distribution," *Power Electronics, IEEE Transactions on,* vol. 25, pp. 3066-3075, 2010.

[28] H. Kakigano, Y. Miura, and T. Ise, "Distribution Voltage Control for DC Microgrids Using Fuzzy Control and Gain-Scheduling Technique," *Power Electronics, IEEE Transactions on,* vol. 28, pp. 2246-2258, 2013.

[29] W. Lu and B. T. Ooi, "Optimal Acquisition and Aggregation of Offshore Wind Power by Multiterminal Voltage-Source HVdc," *Power Engineering Review, IEEE,* vol. 22, pp. 71-72, 2002.

[30] E. Prieto-Araujo, F. D. Bianchi, A. Junyent-Ferre, and O. Gomis-Bellmunt, "Methodology for Droop Control Dynamic Analysis of Multiterminal VSC-HVDC Grids for Offshore Wind Farms," *Power Delivery, IEEE Transactions on,* vol. 26, pp. 2476-2485, 2011.

[31]   W. Lu and B.-T. Ooi, "Premium quality power park based on multi-terminal HVDC," *Power Delivery, IEEE Transactions on,* vol. 20, pp. 978-983, 2005.

[32]   G. O. Kalcon, G. P. Adam, O. Anaya-Lara, S. Lo, and K. Uhlen, "Small-Signal Stability Analysis of Multi-Terminal VSC-Based DC Transmission Systems," *Power Systems, IEEE Transactions on,* vol. 27, pp. 1818-1830, 2012.

[33]   Z. Amjadi and S. S. Williamson, "A Novel Control Technique for a Switched-Capacitor-Converter-Based Hybrid Electric Vehicle Energy Storage System," *Industrial Electronics, IEEE Transactions on,* vol. 57, pp. 926-934, 2010.

[34]   P. Garcia, L. M. Fernandez, C. A. Garcia, and F. Jurado, "Energy Management System of Fuel-Cell-Battery Hybrid Tramway," *Industrial Electronics, IEEE Transactions on,* vol. 57, pp. 4013-4023, 2010.

[35]   H. Yoo, S.-K. Sul, Y. Park, and J. Jeong, "System Integration and Power-Flow Management for a Series Hybrid Electric Vehicle Using Supercapacitors and Batteries," *Industry Applications, IEEE Transactions on,* vol. 44, pp. 108-114, 2008.

[36]   M. M. Amin and O. A. Mohammed, "Design and implementation of dc-bus system module for parallel integrated sustainable energy conversion systems," in *Power and Energy Society General Meeting, 2011 IEEE*, 2011, pp. 1-8.

[37]   R. Alliance, "REbus Microgrid Specification Draft V.0.14," ed, 2011.

[38]   M. E. Ropp and S. Gonzalez, "Development of a MATLAB/Simulink Model of a Single-Phase Grid-Connected Photovoltaic System," *Energy Conversion, IEEE Transactions on,* vol. 24, pp. 195-202, 2009.

[39]   C. Kuei-Hsiang, L. Ching-Ju, and H. Sheng-Han, "Modeling and fault simulation of photovoltaic generation systems using circuit-based model," in *Sustainable Energy Technologies, 2008. ICSET 2008. IEEE International Conference on*, 2008, pp. 290-294.

[40]   P. R. Ortego, S. Bermejo, and L. M. Castaner, "Multichip module photovoltaic miniarrays," *Advanced Packaging, IEEE Transactions on,* vol. 24, pp. 169-174, 2001.

[41]   K. Sun, L. Zhang, Y. Xing, and J. M. Guerrero, "A Distributed Control Strategy Based on DC Bus Signaling for Modular Photovoltaic Generation Systems With Battery Energy Storage," *Power Electronics, IEEE Transactions on,* vol. 26, pp. 3032-3045, 2011.

[42]   T. Esram and P. L. Chapman, "Comparison of Photovoltaic Array Maximum Power Point Tracking Techniques," *Energy Conversion, IEEE Transactions on,* vol. 22, pp. 439-449, 2007.

[43]   S.-J. Kang, J.-S. Ko, J.-S. Choi, M.-G. Jang, J.-H. Mun, J.-G. Lee*, et al.*, "A Novel MPPT Control of photovoltaic system using FLC algorithm," in *Control, Automation and Systems (ICCAS), 2011 11th International Conference on*, 2011, pp. 434-439.

[44]   M. N. Ambia, A. Al-Durra, and S. M. Muyeen, "Centralized power control strategy for AC-DC hybrid micro-grid system using multi-converter

scheme," in *IECON 2011 - 37th Annual Conference on IEEE Industrial Electronics Society*, 2011, pp. 843-848.

[45] B. Wang, M. Sechilariu, and F. Locment, "Intelligent DC Microgrid With Smart Grid Communications: Control Strategy Consideration and Design," *Smart Grid, IEEE Transactions on,* vol. 3, pp. 2148-2156, 2012.

[46] J. M. Guerrero, P. C. Loh, T.-L. Lee, and M. Chandorkar, "Advanced Control Architectures for Intelligent Microgrids-Part II: Power Quality, Energy Storage, and AC/DC Microgrids," *Industrial Electronics, IEEE Transactions on,* vol. 60, pp. 1263-1270, 2013.

[47] Y. K. Chen, Y. C. Wu, C. C. Song, and Y. S. Chen, "Design and Implementation of Energy Management System With Fuzzy Control for DC Microgrid Systems," *Power Electronics, IEEE Transactions on,* vol. 28, pp. 1563-1570, 2013.

[48] V. Salehi, A. Mohamed, and O. A. Mohammed, "Implementation of real-time optimal power flow management system on hybrid AC/DC smart microgrid," in *Industry Applications Society Annual Meeting (IAS), 2012 IEEE*, 2012, pp. 1-8.

[49] H. S. V. S. Kumar Nunna and S. Doolla, "Multiagent-Based Distributed-Energy-Resource Management for Intelligent Microgrids," *Industrial Electronics, IEEE Transactions on,* vol. 60, pp. 1678-1687, 2013.

[50] S. Anand, B. G. Fernandes, and M. Guerrero, "Distributed Control to Ensure Proportional Load Sharing and Improve Voltage Regulation in Low-Voltage DC Microgrids," *Power Electronics, IEEE Transactions on,* vol. 28, pp. 1900-1913, 2013.

[51] J. Schonberger, R. Duke, and S. D. Round, "DC-Bus Signaling: A Distributed Control Strategy for a Hybrid Renewable Nanogrid," *Industrial Electronics, IEEE Transactions on,* vol. 53, pp. 1453-1460, 2006.

[52] J. Schonberger, S. Round, and R. Duke, "Autonomous Load Shedding in a Nanogrid using DC Bus Signalling," in *IEEE Industrial Electronics, IECON 2006 - 32nd Annual Conference on*, 2006, pp. 5155-5160.

[53] D. Chen, L. Xu, and L. Yao, "DC Voltage Variation Based Autonomous Control of DC Microgrids," *Power Delivery, IEEE Transactions on,* vol. 28, pp. 637-648, 2013.

[54] N. D. a. R. Commission, "DL/T 5044-2004 Technical Code for Designing DC System of Power Projects," ed, 2004.

[55] J. Xiao and P. Wang, "Multiple modes control of household DC microgrid with integration of various renewable energy sources," in *Industrial Electronics Society, IECON 2013 - 39th Annual Conference of the IEEE*, 2013, pp. 1773-1778.

[56] L. Zhang, Y. Wang, H. Li, and P. Sun, "Hierarchical coordinated control of DC microgrid with wind turbines," in *IECON 2012 - 38th Annual Conference on IEEE Industrial Electronics Society*, 2012, pp. 3547-3552.

[57] I. Nutkani, L. Chiang, P. Wang, and F. Blaabjerg, "Autonomous Droop Scheme with Reduced Generation Cost," *Industrial Electronics, IEEE Transactions on,* vol. PP, pp. 1-1, 2014.

[58]   L. Setyawan, P. Wang, and J. Xiao, "Implementation of sliding mode control in DC microgrids," in *Industrial Electronics and Applications (ICIEA), 2014 IEEE 9th Conference on*, 2014, pp. 578-583.

[59]   J. D. Dogger, B. Roossien, and F. D. J. Nieuwenhout, "Characterization of Li-Ion Batteries for Intelligent Management of Distributed Grid-Connected Storage," *Energy Conversion, IEEE Transactions on,* vol. 26, pp. 256-263, 2011.

[60]   T. Dragicevic, J. M. Guerrero, J. C. Vasquez, and D. Skrlec, "Supervisory Control of an Adaptive-Droop Regulated DC Microgrid With Battery Management Capability," *Power Electronics, IEEE Transactions on,* vol. 29, pp. 695-706, 2014.

[61]   J. M. Guerrero, J. C. Vasquez, J. Matas, L. G. de Vicuña, and M. Castilla, "Hierarchical Control of Droop-Controlled AC and DC Microgrids: A General Approach Toward Standardization," *Industrial Electronics, IEEE Transactions on,* vol. 58, pp. 158-172, 2011.

[62]   X. Lu, K. Sun, J. M. Guerrero, J. C. Vasquez, and L. Huang, "State-of-Charge Balance Using Adaptive Droop Control for Distributed Energy Storage Systems in DC Microgrid Applications," *Industrial Electronics, IEEE Transactions on,* vol. 61, pp. 2804-2815, 2014.

[63]   X. Lu, K. Sun, J. M. Guerrero, J. C. Vasquez, L. Huang, and R. Teodorescu, "SoC-based droop method for distributed energy storage in DC microgrid applications," in *Industrial Electronics (ISIE), 2012 IEEE International Symposium on*, 2012, pp. 1640-1645.

[64]   Y. Gu, X. Xiang, W. Li, and X. He, "Mode-Adaptive Decentralized Control for Renewable DC Microgrid With Enhanced Reliability and Flexibility," *Power Electronics, IEEE Transactions on,* vol. 29, pp. 5072-5080, 2014.

[65]   X. Lu, J. M. Guerrero, K. Sun, and J. C. Vasquez, "An Improved Droop Control Method for DC Microgrids Based on Low Bandwidth Communication With DC Bus Voltage Restoration and Enhanced Current Sharing Accuracy," *Power Electronics, IEEE Transactions on,* vol. 29, pp. 1800-1812, 2014.

[66]   S. Anand and B. G. Fernandes, "Reduced-Order Model and Stability Analysis of Low-Voltage DC Microgrid," *Industrial Electronics, IEEE Transactions on,* vol. 60, pp. 5040-5049, 2013.

[67]   M. M. A. Abdelaziz, H. E. Farag, and E. F. El-Saadany, "Optimum Droop Parameter Settings of Islanded Microgrids With Renewable Energy Resources," *Sustainable Energy, IEEE Transactions on,* vol. 5, pp. 434-445, 2014.

[68]   D. Bo, Y. Li, and Z. Zheng, "Energy management of hybrid DC and AC bus linked microgrid," in *Power Electronics for Distributed Generation Systems (PEDG), 2010 2nd IEEE International Symposium on*, 2010, pp. 713-716.

[69]   C. Jin, P. C. Loh, P. Wang, Y. Mi, and F. Blaabjerg, "Autonomous operation of hybrid AC-DC microgrids," in *Sustainable Energy Technologies (ICSET), 2010 IEEE International Conference on*, 2010, pp. 1-7.

[70]   P. C. Loh and F. Blaabjerg, "Autonomous control of distributed storages in microgrids," in *Power Electronics and ECCE Asia (ICPE & ECCE), 2011 IEEE 8th International Conference on*, 2011, pp. 536-542.

[71]   S. Kai, Z. Li, X. Yan, and J. M. Guerrero, "A Distributed Control Strategy Based on DC Bus Signaling for Modular Photovoltaic Generation Systems With Battery Energy Storage," *Power Electronics, IEEE Transactions on,* vol. 26, pp. 3032-3045, 2011.

[72]   A. Khorsandi, M. Ashourloo, and H. Mokhtari, "A Decentralized Control Method for a Low-Voltage DC Microgrid," *Energy Conversion, IEEE Transactions on,* vol. 29, pp. 793-801, 2014.

[73]   Y.-E. Wu, C.-L. Shen, and C.-Y. Liu, "Implementation of solar illumination system with three-stage charging and dimming control function," in *Electric Information and Control Engineering (ICEICE), 2011 International Conference on*, 2011, pp. 2260-2263.

[74]   K. W. E. Cheng, B. P. Divakar, H. Wu, D. Kai, and H. F. Ho, "Battery-Management System (BMS) and SOC Development for Electrical Vehicles," *Vehicular Technology, IEEE Transactions on,* vol. 60, pp. 76-88, 2011.

[75]   C. Jin, P. Wang, J. Xiao, Y. Tang, and F. H. Choo, "Implementation of Hierarchical Control in DC Microgrids," *Industrial Electronics, IEEE Transactions on,* vol. 61, pp. 4032-4042, 2014.

[76]   S. Armstrong, M. E. Glavin, and W. G. Hurley, "Comparison of battery charging algorithms for stand alone photovoltaic systems," in *Power Electronics Specialists Conference, 2008. PESC 2008. IEEE*, 2008, pp. 1469-1475.

[77]   J.-S. Moon, J.-H. Lee, I.-Y. Ha, T.-K. Lee, and C.-Y. Won, "An efficient battery charging algorithm based on state-of-charge estimation for electric vehicle," in *Electrical Machines and Systems (ICEMS), 2011 International Conference on*, 2011, pp. 1-6.

[78]   T. Logenthiran, D. Srinivasan, A. M. Khambadkone, and H. N. Aung, "Multiagent System for Real-Time Operation of a Microgrid in Real-Time Digital Simulator," *Smart Grid, IEEE Transactions on,* vol. 3, pp. 925-933, 2012.

[79]   M.-E. Choi, S.-W. Kim, and S.-W. Seo, "Energy Management Optimization in a Battery/Supercapacitor Hybrid Energy Storage System," *Smart Grid, IEEE Transactions on,* vol. 3, pp. 463-472, 2012.

[80]   M. Zandi, A. Payman, J. P. Martin, S. Pierfederici, B. Davat, and F. Meibody-Tabar, "Energy Management of a Fuel Cell/Supercapacitor/Battery Power Source for Electric Vehicular Applications," *Vehicular Technology, IEEE Transactions on,* vol. 60, pp. 433-443, 2011.

[81]   N. Mendis, K. M. Muttaqi, and S. Perera, "Management of Battery-Supercapacitor Hybrid Energy Storage and Synchronous Condenser for Isolated Operation of PMSG Based Variable-Speed Wind Turbine Generating Systems," *Smart Grid, IEEE Transactions on,* vol. 5, pp. 944-953, 2014.

158

[82] L. Maharjan, S. Inoue, H. Akagi, and J. Asakura, "State-of-Charge (SOC)-Balancing Control of a Battery Energy Storage System Based on a Cascade PWM Converter," *Power Electronics, IEEE Transactions on,* vol. 24, pp. 1628-1636, 2009.

[83] J. Xiao, P. Wang, C. Jin, and F. H. Choo, "Multi-level control of grid-tied DC microgrids," in *Power and Energy Engineering Conference (APPEEC), 2013 IEEE PES Asia-Pacific*, 2013, pp. 1-6.

[84] A. Ghazanfari, M. Hamzeh, H. Mokhtari, and H. Karimi, "Active Power Management of Multihybrid Fuel Cell/Supercapacitor Power Conversion System in a Medium Voltage Microgrid," *Smart Grid, IEEE Transactions on,* vol. 3, pp. 1903-1910, 2012.

[85] L. Xu and D. Chen, "Control and Operation of a DC Microgrid With Variable Generation and Energy Storage," *Power Delivery, IEEE Transactions on,* vol. 26, pp. 2513-2522, 2011.

[86] X. Yu, X. She, X. Zhou, and A. Q. Huang, "Power Management for DC Microgrid Enabled by Solid-State Transformer," *Smart Grid, IEEE Transactions on,* vol. 5, pp. 954-965, 2014.

[87] M. Savaghebi, A. Jalilian, J. C. Vasquez, and J. M. Guerrero, "Secondary Control for Voltage Quality Enhancement in Microgrids," *Smart Grid, IEEE Transactions on,* vol. 3, pp. 1893-1902, 2012.

[88] X. Lu, J. M. Guerrero, K. Sun, J. C. Vasquez, R. Teodorescu, and L. Huang, "Hierarchical Control of Parallel AC-DC Converter Interfaces for Hybrid Microgrids," *Smart Grid, IEEE Transactions on,* vol. 5, pp. 683-692, 2014.

[89] R. S. Balog, W. W. Weaver, and P. T. Krein, "The Load as an Energy Asset in a Distributed DC SmartGrid Architecture," *Smart Grid, IEEE Transactions on,* vol. 3, pp. 253-260, 2012.

[90] F. Shariatzadeh, C. B. Vellaithurai, S. S. Biswas, R. Zamora, and A. K. Srivastava, "Real-Time Implementation of Intelligent Reconfiguration Algorithm for Microgrid," *Sustainable Energy, IEEE Transactions on,* vol. 5, pp. 598-607, 2014.

[91] P. Poonpun and W. T. Jewell, "Analysis of the Cost per Kilowatt Hour to Store Electricity," *Energy Conversion, IEEE Transactions on,* vol. 23, pp. 529-534, 2008.

[92] S. A. Pourmousavi, R. K. Sharma, and B. Asghari, "A framework for real-time power management of a grid-tied microgrid to extend battery lifetime and reduce cost of energy," in *Innovative Smart Grid Technologies (ISGT), 2012 IEEE PES*, 2012, pp. 1-8.

[93] S. Drouilhet and B. L. Johnson, "A Battery Life Prediction Method for Hybrid Power Applications," presented at the AIAA Aerospace Sciences Meeting and Exhibit, 1997.

[94] D. P. Jenkins, J. Fletcher, and D. Kane, "Lifetime prediction and sizing of lead-acid batteries for microgeneration storage applications," *Renewable Power Generation, IET,* vol. 2, pp. 191-200, 2008.

[95] J. F. Manwell, J. G. Mcgowan, U. Abdulwahid, and K. Wu, "Improvements to the Hybrid2 Battery Model," presented at the American Wind Energy Association Windpower 2005 Conference, 2005.

[96]   C. Wang, X. Li, L. Guo, and Y. W. Li, "A Nonlinear-Disturbance-Observer-Based DC-Bus Voltage Control for a Hybrid AC/DC Microgrid," *Power Electronics, IEEE Transactions on,* vol. 29, pp. 6162-6177, 2014.

[97]   P. C. Loh, D. Li, Y. K. Chai, and F. Blaabjerg, "Autonomous Operation of Hybrid Microgrid With AC and DC Subgrids," *Power Electronics, IEEE Transactions on,* vol. 28, pp. 2214-2223, 2013.

[98]   K. Kurohane, T. Senjyu, A. Yona, N. Urasaki, T. Goya, and T. Funabashi, "A Hybrid Smart AC/DC Power System," *Smart Grid, IEEE Transactions on,* vol. 1, pp. 199-204, 2010.

[99]   X. Liu, P. C. Loh, P. Wang, and F. Blaabjerg, "A Direct Power Conversion Topology for Grid Integration of Hybrid AC/DC Energy Resources," *Industrial Electronics, IEEE Transactions on,* vol. 60, pp. 5696-5707, 2013.

[100]   P. Wang, L. Goel, X. Liu, and F. H. Choo, "Harmonizing AC and DC: A Hybrid AC/DC Future Grid Solution," *Power and Energy Magazine, IEEE,* vol. 11, pp. 76-83, 2013.

[101]   C. Hou and Y. Huang, "Diode Rectifier with Auxiliary Converter for Hybrid AC/DC Microgrids," *Emerging and Selected Topics in Power Electronics, IEEE Journal of,* vol. PP, pp. 1-1, 2014.

[102]   J. Rocabert, A. Luna, F. Blaabjerg, and P. Rodriguez, "Control of Power Converters in AC Microgrids," *Power Electronics, IEEE Transactions on,* vol. 27, pp. 4734-4749, 2012.

[103]   D. Shi, Y. Luo, and R. K. Sharma, "Active synchronization control for microgrid reconnection after islanding," in *Innovative Smart Grid Technologies Conference Europe (ISGT-Europe), 2014 IEEE PES*, 2014, pp. 1-6.

[104]   C. Cho, J.-H. Jeon, J.-Y. Kim, S. Kwon, K. Park, and S. Kim, "Active Synchronizing Control of a Microgrid," *Power Electronics, IEEE Transactions on,* vol. 26, pp. 3707-3719, 2011.

[105]   N. Eghtedarpour and E. Farjah, "Power Control and Management in a Hybrid AC/DC Microgrid," *Smart Grid, IEEE Transactions on,* vol. 5, pp. 1494-1505, 2014.

[106]   W. Issa, M. Abusara, and S. Sharkh, "Control of Transient Power during Unintentional Islanding of Microgrids," *Power Electronics, IEEE Transactions on,* vol. PP, pp. 1-1, 2014.

[107]   A. Bidram and A. Davoudi, "Hierarchical Structure of Microgrids Control System," *Smart Grid, IEEE Transactions on,* vol. 3, pp. 1963-1976, 2012.

[108]   Y. Gu, W. Li, and X. He, "Frequency-Coordinating Virtual Impedance for Autonomous Power Management of DC Microgrid," *Power Electronics, IEEE Transactions on,* vol. 30, pp. 2328-2337, 2015.

[109]   X. Liu, P. Wang, and P. C. Loh, "A Hybrid AC/DC Microgrid and Its Coordination Control," *Smart Grid, IEEE Transactions on,* vol. 2, pp. 278-286, 2011.

[110]   P. Wang, C. Jin, D. Zhu, Y. Tang, P. C. Loh, and F. H. Choo, "Distributed Control for Autonomous Operation of a Three-Port AC/DC/DS Hybrid Microgrid," *Industrial Electronics, IEEE Transactions on,* vol. PP, pp. 1-1, 2014.

[111] C. Jin, P. Wang, J. Xiao, Y. Tang, and Choo, "Implementation of Hierarchical Control in DC Microgrids," *Industrial Electronics, IEEE Transactions on,* vol. PP, pp. 1-1, 2013.

[112] Q. Li, S. S. Choi, Y. Yuan, and D. L. Yao, "On the Determination of Battery Energy Storage Capacity and Short-Term Power Dispatch of a Wind Farm," *Sustainable Energy, IEEE Transactions on,* vol. 2, pp. 148-158, 2011.

[113] T. Nguyen, M. Crow, and A. Elmore, "Optimal Sizing of a Vanadium Redox Battery System for Microgrid Systems," *Sustainable Energy, IEEE Transactions on,* vol. PP, pp. 1-9, 2015.

[114] A. Aichhorn, M. Greenleaf, H. Li, and J. Zheng, "A cost effective battery sizing strategy based on a detailed battery lifetime model and an economic energy management strategy," in *Power and Energy Society General Meeting, 2012 IEEE*, 2012, pp. 1-8.

[115] R. Yu, J. Kleissl, and S. Martinez, "Storage Size Determination for Grid-Connected Photovoltaic Systems," *Sustainable Energy, IEEE Transactions on,* vol. 4, pp. 68-81, 2013.

[116] S. X. Chen, H. B. Gooi, and M. Q. Wang, "Sizing of Energy Storage for Microgrids," *Smart Grid, IEEE Transactions on,* vol. 3, pp. 142-151, 2012.

[117] S. Bahramirad, W. Reder, and A. Khodaei, "Reliability-Constrained Optimal Sizing of Energy Storage System in a Microgrid," *Smart Grid, IEEE Transactions on,* vol. 3, pp. 2056-2062, 2012.

[118] Z. Y. Gao, P. Wang, L. Bertling, and J. H. Wang, "Sizing of energy storage for power systems with wind farms based on reliability cost and wroth analysis," in *Power and Energy Society General Meeting, 2011 IEEE*, 2011, pp. 1-7.

[119] A. Chaouachi, R. M. Kamel, R. Andoulsi, and K. Nagasaka, "Multiobjective Intelligent Energy Management for a Microgrid," *Industrial Electronics, IEEE Transactions on,* vol. 60, pp. 1688-1699, 2013.

[120] F. A. Mohamed and H. N. Koivo, "MicroGrid Online Management and Balancing Using Multiobjective Optimization," in *Power Tech, 2007 IEEE Lausanne*, 2007, pp. 639-644.

[121] M. Sechilariu, B. Wang, and F. Locment, "Power management and optimization for isolated DC microgrid," in *Power Electronics, Electrical Drives, Automation and Motion (SPEEDAM), 2014 International Symposium on*, 2014, pp. 1284-1289.

[122] G. Carpinelli, A. Bracale, and P. Caramia, "The GREAT project: Integer linear programming-based day-ahead optimal scheduling of a DC microgrid," in *Environment and Electrical Engineering (EEEIC), 2013 12th International Conference on*, 2013, pp. 573-578.

[123] I. Duggal and B. Venkatesh, "Short-Term Scheduling of Thermal Generators and Battery Storage With Depth of Discharge-Based Cost Model," *Power Systems, IEEE Transactions on,* vol. PP, pp. 1-9, 2014.

[124] V. Agarwal, K. Uthaichana, R. A. DeCarlo, and L. H. Tsoukalas, "Development and Validation of a Battery Model Useful for Discharging

161

and Charging Power Control and Lifetime Estimation," *Energy Conversion, IEEE Transactions on,* vol. 25, pp. 821-835, 2010.

[125] Z. Bo, Z. Xuesong, C. Jian, W. Caisheng, and G. Li, "Operation Optimization of Standalone Microgrids Considering Lifetime Characteristics of Battery Energy Storage System," *Sustainable Energy, IEEE Transactions on,* vol. 4, pp. 934-943, 2013.

[126] Q. Hao, Z. Jianhui, L. Jih-Sheng, and Y. Wensong, "A High-Efficiency Grid-Tie Battery Energy Storage System," *Power Electronics, IEEE Transactions on,* vol. 26, pp. 886-896, 2011.

[127] R. Billinton and W. Peng, "Distribution system reliability cost/worth analysis using analytical and sequential simulation techniques," *Power Systems, IEEE Transactions on,* vol. 13, pp. 1245-1250, 1998.

[128] I. Baklouti, Z. Driss, and M. S. Abid, "Estimation of solar radiation on horizontal and inclined surfaces in Sfax, TUNISIA," in *Renewable Energies and Vehicular Technology (REVET), 2012 First International Conference on*, 2012, pp. 131-140.

[129] M. Ding, L. Wang, and R. Bi, "An ANN-based Approach for Forecasting the Power Output of Photovoltaic System," *Procedia Environmental Sciences,* vol. 11, Part C, pp. 1308-1315, // 2011.

[130] H. Shyh-Jier and S. Kuang-Rong, "Short-term load forecasting via ARMA model identification including non-Gaussian process considerations," *Power Systems, IEEE Transactions on,* vol. 18, pp. 673-679, 2003.

[131] H. Rui, H. Tiana, R. Gadh, and L. Na, "Solar generation prediction using the ARMA model in a laboratory-level micro-grid," in *Smart Grid Communications (SmartGridComm), 2012 IEEE Third International Conference on*, 2012, pp. 528-533.

[132] M. Cococcioni, E. D'Andrea, and B. Lazzerini, "24-hour-ahead forecasting of energy production in solar PV systems," in *Intelligent Systems Design and Applications (ISDA), 2011 11th International Conference on*, 2011, pp. 1276-1281.

[133] J. H. Chow, F. F. Wu, and J. A. Momoh, *Applied Mathematics for Restructured Electric Power Systems: Optimization, Control, and Computational Intelligence*: Springer, 2006.

[134] S. Drouilhet and B. L. Johnson, "A battery life prediction method for hybrid power applications," 1997.

[135] D. M. Rastler and E. P. R. Institute, *Electricity Energy Storage Technology Options: A White Paper Primer on Applications, Costs and Benefits*: Electric Power Research Institute, 2010.

[136] J. W. Shim, Y. Cho, S.-J. Kim, S. W. Min, and K. Hur, "Synergistic Control of SMES and Battery Energy Storage for Enabling Dispatchability of Renewable Energy Sources," *Applied Superconductivity, IEEE Transactions on,* vol. 23, pp. 5701205-5701205, 2013.

[137] A. Khaligh and Z. Li, "Battery, Ultracapacitor, Fuel Cell, and Hybrid Energy Storage Systems for Electric, Hybrid Electric, Fuel Cell, and Plug-In Hybrid Electric Vehicles: State of the Art," *Vehicular Technology, IEEE Transactions on,* vol. 59, pp. 2806-2814, 2010.

[138] F. Liu, J. Liu, H. Zhang, D. Xue, H. S. Ul, and L. Zhou, "Stability issues of Z + Z type cascade system in Hybrid Energy Storage System (HESS)," in *Energy Conversion Congress and Exposition (ECCE), 2013 IEEE*, 2013, pp. 434-441.

[139] M. Romer, G. H. Miley, N. Luo, and R. J. Gimlin, "Ragone Plot Comparison of Radioisotope Cells and the Direct Sodium Borohydride/Hydrogen Peroxide Fuel Cell With Chemical Batteries," *Energy Conversion, IEEE Transactions on,* vol. 23, pp. 171-178, 2008.

[140] D. V. Ragone, "Review of Battery Systems for Electrically Powered Vehicles," 1968.

[141] Q. Xie, Y. Wang, Y. Kim, M. Pedram, and N. Chang, "Charge Allocation in Hybrid Electrical Energy Storage Systems," *Computer-Aided Design of Integrated Circuits and Systems, IEEE Transactions on,* vol. 32, pp. 1003-1016, 2013.

[142] A. Esmaili, B. Novakovic, A. Nasiri, and O. Abdel-Baqi, "A Hybrid System of Li-Ion Capacitors and Flow Battery for Dynamic Wind Energy Support," *Industry Applications, IEEE Transactions on,* vol. 49, pp. 1649-1657, 2013.

[143] S. Lemofouet and A. Rufer, "A Hybrid Energy Storage System Based on Compressed Air and Supercapacitors With Maximum Efficiency Point Tracking (MEPT)," *Industrial Electronics, IEEE Transactions on,* vol. 53, pp. 1105-1115, 2006.

[144] Y. Zhang, Z. Jiang, and X. Yu, "Control Strategies for Battery/Supercapacitor Hybrid Energy Storage Systems," in *Energy 2030 Conference, 2008. ENERGY 2008. IEEE*, 2008, pp. 1-6.

[145] L. P. Jarvis, T. B. Atwater, and P. J. Cygan, "Hybrid power sources for Land Warrior scenario," *Aerospace and Electronic Systems Magazine, IEEE,* vol. 15, pp. 37-41, 2000.

[146] Z. Amjadi and S. S. Williamson, "Modeling, Simulation, and Control of an Advanced Luo Converter for Plug-In Hybrid Electric Vehicle Energy-Storage System," *Vehicular Technology, IEEE Transactions on,* vol. 60, pp. 64-75, 2011.

[147] M. Farhadi and O. A. Mohammed, "Real-Time Operation and Harmonic Analysis of Isolated and Non-Isolated Hybrid DC Microgrid," *Industry Applications, IEEE Transactions on,* vol. 50, pp. 2900-2909, 2014.

[148] R. A. Dougal, S. Liu, and R. E. White, "Power and life extension of battery-ultracapacitor hybrids," *Components and Packaging Technologies, IEEE Transactions on,* vol. 25, pp. 120-131, 2002.

[149] C. Abbey, W. Li, and G. Joos, "An Online Control Algorithm for Application of a Hybrid ESS to a Wind-Diesel System," *Industrial Electronics, IEEE Transactions on,* vol. 57, pp. 3896-3904, 2010.

[150] H. Wen, W. Xiao, H. Li, and X. Wen, "Analysis and minimisation of DC bus surge voltage for electric vehicle applications," *Electrical Systems in Transportation, IET,* vol. 2, pp. 68-76, 2012.

[151] S. Lu, K. A. Corzine, and M. Ferdowsi, "A New Battery/Ultracapacitor Energy Storage System Design and Its Motor Drive Integration for Hybrid

Electric Vehicles," *Vehicular Technology, IEEE Transactions on,* vol. 56, pp. 1516-1523, 2007.

[152] Z. Amjadi and S. S. Williamson, "Prototype Design and Controller Implementation for a Battery-Ultracapacitor Hybrid Electric Vehicle Energy Storage System," *Smart Grid, IEEE Transactions on,* vol. 3, pp. 332-340, 2012.

[153] L. Gao, R. A. Dougal, and S. Liu, "Power enhancement of an actively controlled battery/ultracapacitor hybrid," *Power Electronics, IEEE Transactions on,* vol. 20, pp. 236-243, 2005.

[154] H. Yu, R. Lu, T. Wang, and C. Zhu, "Energetic Macroscopic Representation based modeling and control for battery/ultra-capacitor hybrid energy strorage system in HEV," in *Vehicle Power and Propulsion Conference, 2009. VPPC '09. IEEE*, 2009, pp. 1390-1394.

[155] W. Li, G. Joos, and J. Belanger, "Real-Time Simulation of a Wind Turbine Generator Coupled With a Battery Supercapacitor Energy Storage System," *Industrial Electronics, IEEE Transactions on,* vol. 57, pp. 1137-1145, 2010.

[156] S. M. Lukic, J. Cao, R. C. Bansal, F. Rodriguez, and A. Emadi, "Energy Storage Systems for Automotive Applications," *Industrial Electronics, IEEE Transactions on,* vol. 55, pp. 2258-2267, 2008.

[157] P. Wang, J. Xiao, L. Setyawan, C. Jin, and F. H. Choo, "Hierarchical control of active hybrid energy storage system (HESS) in DC microgrids," in *Industrial Electronics and Applications (ICIEA), 2014 IEEE 9th Conference on*, 2014, pp. 569-574.

[158] A. Kuperman and I. Aharon, "Battery–ultracapacitor hybrids for pulsed current loads: A review," *Renewable and Sustainable Energy Reviews,* vol. 15, pp. 981-992, 2011.

[159] J. Wei and B. Fahimi, "Active Current Sharing and Source Management in Fuel Cell-Battery Hybrid Power System," *Industrial Electronics, IEEE Transactions on,* vol. 57, pp. 752-761, 2010.

[160] N. Mendis, K. M. Muttaqi, and S. Perera, "Management of Low- and High-Frequency Power Components in Demand-Generation Fluctuations of a DFIG-Based Wind-Dominated RAPS System Using Hybrid Energy Storage," *Industry Applications, IEEE Transactions on,* vol. 50, pp. 2258-2268, 2014.

[161] A. Mohamed, V. Salehi, and O. Mohammed, "Real-Time Energy Management Algorithm for Mitigation of Pulse Loads in Hybrid Microgrids," *Smart Grid, IEEE Transactions on,* vol. 3, pp. 1911-1922, 2012.

[162] I. J. Cohen, J. P. Kelley, D. A. Wetz, and J. Heinzel, "Evaluation of a Hybrid Energy Storage Module for Pulsed Power Applications," *Plasma Science, IEEE Transactions on,* vol. PP, pp. 1-1, 2014.

[163] B. Shrestha, D. A. Wetz, and P. M. Novak, "Pulsed Elevated Rate Discharge of Electrochemical Energy Storage Devices," *Plasma Science, IEEE Transactions on,* vol. 40, pp. 2462-2469, 2012.

[164]   J. P. Zheng, T. R. Jow, and M. S. Ding, "Hybrid power sources for pulsed current applications," *Aerospace and Electronic Systems, IEEE Transactions on,* vol. 37, pp. 288-292, 2001.

[165]   S. Toshikazu, K. Takahiro, N. Yoshiyuki, K. Kazunori, and Y. Keiji, "Redox Flow Batteries for the Stable Supply of Renewable Energy," *SEI Technical Review,* vol. 76, p. 9, 2013.

[166]   M. Houwing, R. R. Negenborn, M. D. Ilić, and B. De Schutter, "Model predictive control of fuel cell micro cogeneration systems," in *Networking, Sensing and Control, 2009. ICNSC '09. International Conference on*, 2009, pp. 708-713.

[167]   S. Succar; and R. H. Williams, "Compressed Air Energy Storage: Theory, Resources, And Applications For Wind Power," Princeton Environmental Institute, Princeton University2008.

[168]   K. Jin, X. Ruan, M. Yang, and M. Xu, "A Hybrid Fuel Cell Power System," *Industrial Electronics, IEEE Transactions on,* vol. 56, pp. 1212-1222, 2009.

[169]   Q. Jiang and H. Hong, "Wavelet-Based Capacity Configuration and Coordinated Control of Hybrid Energy Storage System for Smoothing Out Wind Power Fluctuations," *Power Systems, IEEE Transactions on,* vol. 28, pp. 1363-1372, 2013.

[170]   S. K. Kollimalla, M. K. Mishra, and N. L. Narasamma, "Design and Analysis of Novel Control Strategy for Battery and Supercapacitor Storage System," *Sustainable Energy, IEEE Transactions on,* vol. 5, pp. 1137-1144, 2014.

[171]   C. Sen, Y. Usama, T. Carciumaru, X. Lu, and N. C. Kar, "Design of a Novel Wavelet Based Transient Detection Unit for In-Vehicle Fault Determination and Hybrid Energy Storage Utilization," *Smart Grid, IEEE Transactions on,* vol. 3, pp. 422-433, 2012.

[172]   G. Wang, M. Ciobotaru, and V. G. Agelidis, "Power Smoothing of Large Solar PV Plant Using Hybrid Energy Storage," *Sustainable Energy, IEEE Transactions on,* vol. 5, pp. 834-842, 2014.

[173]   X. Chen, J. Jin, Y. Xin, B. Shu, C. Tang, Y. Zhu*, et al.*, "Integrated SMES Technology for Modern Power System and Future Smart Grid," *Applied Superconductivity, IEEE Transactions on,* vol. PP, pp. 1-1, 2014.

[174]   J. Jia, G. Wang, Y. T. Cham, Y. Wang, and M. Han, "Electrical Characteristic Study of a Hybrid PEMFC and Ultracapacitor System," *Industrial Electronics, IEEE Transactions on,* vol. 57, pp. 1945-1953, 2010.

[175]   R. M. Kamel, A. Chaouachi, and K. Nagasaka, "Three Control Strategies to Improve the Microgrid Transient Dynamic Response During Isolated Mode: A Comparative Study," *Industrial Electronics, IEEE Transactions on,* vol. 60, pp. 1314-1322, 2013.

[176]   Z. Nie, X. Xiao, Q. Kang, R. Aggarwal, H. Zhang, and W. Yuan, "SMES-Battery Energy Storage System for Conditioning Outputs From Direct Drive Linear Wave Energy Converters," *Applied Superconductivity, IEEE Transactions on,* vol. 23, pp. 5000705-5000705, 2013.

[177] J. Xiao, P. Wang, and L. Setyawan, "Hierarchical Control of Hybrid Energy Storage System in DC Microgrids," *Industrial Electronics, IEEE Transactions on,* vol. PP, pp. 1-1, 2015.

[178] I. U. Nutkani, L. Poh Chiang, W. Peng, and F. Blaabjerg, "Cost-Prioritized Droop Schemes for Autonomous AC Microgrids," *Power Electronics, IEEE Transactions on,* vol. 30, pp. 1109-1119, 2015.

[179] A. Seon-Ju, N. Soon-Ryul, C. Joon-Ho, and M. Seung-Il, "Power Scheduling of Distributed Generators for Economic and Stable Operation of a Microgrid," *Smart Grid, IEEE Transactions on,* vol. 4, pp. 398-405, 2013.

[180] A. Parisio and L. Glielmo, "Multi-objective optimization for environmental/economic microgrid scheduling," in *Cyber Technology in Automation, Control, and Intelligent Systems (CYBER), 2012 IEEE International Conference on*, 2012, pp. 17-22.

[181] M. Ross, C. Abbey, F. Bouffard, and G. Joos, "Multiobjective Optimization Dispatch for Microgrids With a High Penetration of Renewable Generation," *Sustainable Energy, IEEE Transactions on,* vol. PP, pp. 1-9, 2015.

[182] M. Mahmoodi, P. Shamsi, and B. Fahimi, "Economic Dispatch of a Hybrid Microgrid With Distributed Energy Storage," *Smart Grid, IEEE Transactions on,* vol. PP, pp. 1-1, 2015.

[183] W. Shi, N. Li, C. C. Chu, and R. Gadh, "Real-Time Energy Management in Microgrids," *Smart Grid, IEEE Transactions on,* vol. PP, pp. 1-1, 2015.

[184] R. Turvey, *What are marginal costs and how to estimate them?* vol. 13: Ralph Turvey, 2000.

[185] I. U. Nutkani, P. Wang, L. Poh Chiang, and F. Blaabjerg, "Cost-based droop scheme for DC microgrid," in *Energy Conversion Congress and Exposition (ECCE), 2014 IEEE*, 2014, pp. 765-769.